Hyperpolarized Noble Gases as Biomarkers for Pulmonary Pathology

Clémentine Lesbats

Thesis submitted to the University of Nottingham
for the degree of Doctor of Philosophy

November 2016

ABSTRACT

Hyperpolarized noble gas MRI using ^{3}He and ^{129}Xe has allowed void space imaging of the lungs for several years. Hyperpolarized ^{83}Kr MRI has also been shown to provide an MRI contrast sensitive to the surface-to-volume ratio and chemistry of synthetic porous systems. *Ex vivo* animal models of pulmonary diseases and *in vitro* experiments were used in this thesis to examine three methodological advances allowing for the measurement of pulmonary physiological parameters using ^{129}Xe and ^{83}Kr.

The ^{83}Kr quadrupolar property was explored in a rat model of pulmonary surface-to-volume ratio degradation, i.e. emphysema. The surface quadrupolar relaxation (SQUARE) of the noble gas provided maps of the longitudinal relaxation in control and emphysematous rat lungs. The relaxation observations were regionally correlated to the histological measurements of the alveolar degradation.

The ^{129}Xe solubility in the lungs, blood, and more generally liquids, was the basis for the design of a new biosensor composed of a cryptophane cage tethered to a paramagnetic agent. The depolarization of the ^{129}Xe atoms encapsulated by the cryptophane, followed by chemical exchange with the surrounding medium was investigated *in vitro*. This model biosensor will lead to a future switchable biosensor that will be deactivated by the enzymatic cleavage of the encapsulating cage and the paramagnetic agent.

Finally, the ^{129}Xe solubility was further utilised to study the gas transfer through *ex vivo* rat lungs after blood replacement by a perfluorocarbon emulsion. The large chemical shift separating the ^{129}Xe peaks for the gas phase, the tissue and the perfluorocarbon emulsion, allowed for a selective excitation of each phase and the independent observation of their signal build-up after inhalation. This mechanism will be used as a biomarker for gas transfer impairment in animal models of pulmonary fibrosis.

ACKNOWLEDGEMENTS

I would like to acknowledge all of the people who have helped me during the course of the work contained in this thesis. Firstly, I would like to thank my supervisors Thomas Meersmann and Galina Pavlovskaya for their everyday guidance and numerous pieces of advice during the past three years and half.

I would like to acknowledge the team I have worked with, and particularly my two first laboratory colleagues Joseph Six and David Lilburn without whom I would not know how to hyperpolarize, how to dissect rat lungs, how to work in this laboratory and how to multitask. I doubt I will ever forget the long nights working with them in the laboratory. I also want to thank Nicola Rogers for the real support and inspiration she gave me from the time she joined the group in my second year, after both Joe and David had left. These three people deserve my gratitude for preparing me for my research projects and for their friendship. I also want to thank Fraser Hill-Casey for his friendly assistance in the laboratory every day of the week and Zahra Rahemtulla for making my life easier with an automated recompression unit. I would also like to thank Alan Dorkes who fixed all of my broken equipment, and improved all of the designs I brought him.

I am also very thankful to the valuable friends I have met at the MRI centre from the moment I arrived. A lot of support also came from the friends who didn't know anything about MRI, my first year hall friends, and my colleague tutors. All of these people opened my mind to new horizons and helped me through this unforgettable experience.

Finally, I would like to thank my family and friends who encouraged me from Bordeaux and Paris.

Merci infiniment !

TABLE OF CONTENTS

CHAPTER 1

INTRODUCTION

1.1. Motivation

The decrease of the number of infectious diseases and their virulence led to a shift of the worldwide main causes of death to chronic conditions such as pulmonary or heart diseases. Moreover, the environmental changes and the increase of tobacco exposure in the population induced a dramatic increase in chronic pulmonary diseases (COPD), which include number of non-reversible respiratory conditions (e.g. emphysema) with a slowly progressing decrease in lung function. The annual cost for taking care of the 3 million patients with COPD in the UK (although 2 million are undiagnosed) represents £36 million (1). According to the WHO, COPD is predicted to become the third leading cause of death in 2030 (2). Idiopathic pulmonary fibrosis is another respiratory disease related to tobacco smoking. This chronic and progressive interstitial disease occurs in 4200 new patients each year in England (3). Chronic pulmonary diseases show variable symptoms and are often not diagnosed in the early stage of the disease. They often require the collaboration of numerous medical specialists, and necessitate X-rays and spirometry tests.

Some early stage biomarkers would be beneficial for an earlier diagnosis of these pulmonary diseases and would allow for targeted treatments and a better management of the symptoms.

1.2. Imaging lung disease

The most commonly used clinical method to diagnose or longitudinally monitor lung disease is high-resolution computed tomography (HRCT). Even though this imaging technique provides excellent anatomical features, it also involves the use of ionising X-rays radiations. Lung function tests such as spirometry or plethysmography give a global evaluation of the lung volumes and the ability to exchange gas, without spatial resolution. But the anatomical and functional changes caused by pulmonary diseases are not homogeneous over the organ.

At the difference of CT, magnetic resonance imaging (MRI) is a non-invasive tool that can be used to investigate lung disease. However, the low proton density of the lung (4), and the short relaxation times caused by the air-tissue interface (5) are major drawbacks for the technique. Fast acquisitions have been developed to overcome the fast relaxation in the pulmonary tissue (6), but the low tissue density is the main feature of the organ that cannot be amended.

MRI has however the advantage to be able to image different nuclei such as the noble gases ^{3}He, ^{129}Xe or ^{83}Kr, enabling harmless imaging of the airspace after the inhalation of a noble gas. Recent developments in spin exchange optical pumping (SEOP) in the past three decades have allowed for a great increase of the hyperpolarized noble gas signal intensity, and therefore high-resolution ventilation imaging. Ventilation imaging gives a spatial resolution of the ventilation defects, whereas the spirometry test is only providing a global evaluation of the ventilation function.

Different methods using hyperpolarized noble gases have been giving functional parameters. For example, the inhaled gas being subject to a restricted diffusion in the alveoli, the ^{3}He apparent diffusion coefficient (ACD) can define the alveolar dimensions (7, 8). Changes in this diffusion can be used as a biomarker for the alveolar degradation caused by emphysema (8-10). Hyperpolarized ^{129}Xe ADC was also demonstrated to be able to distinguish emphysematous lung to healthy lung (11).

^{129}Xe also presents the unique property to dissolve in the lung tissue after inhalation. The large ^{129}Xe chemical shift when dissolved in the pulmonary tissue or the blood has been used as an advantage to study the lung gas exchange using MRI. ^{129}Xe gas exchange through the lung barrier is used as a biomarker for parenchymal thickening caused by pulmonary fibrosis (12).

Finally, hyperpolarized ^{83}Kr MRI has been demonstrated to be an alternative biomarker for the alveolar destruction. Its nuclear electric quadrupole moment is a probe for surfaces. Such interactions are detected by measuring the ^{83}Kr longitudinal relaxation (T_1) in the gas phase (13-15).

Hyperpolarized noble gas imaging is a method allowing longitudinal pharmacological studies without an over-exposition to ionising radiations and providing functional biomarkers that cannot be obtained using HRCT.

1.3. Small animal study of pulmonary pathology

Small animal models of human pulmonary diseases have been commonly used for both pharmacological development and imaging methodology development. Rodents are often used because of their fast breeding and their low cost. The use of small animals however requires the improvement of most techniques that were developed for humans. Various difficulties are encountered when using small animals for *in vivo* imaging experiments. Beyond the need of higher resolution, the main issue is the impossibility to make the animals breath-hold and stay still like a human subject would do. By a matter of fact, a ventilator and neuromuscular blocking agents are necessary to force the animal having a controlled behaviour similar to a human (16). Some other groups have developed free breathing hyperpolarized rodent lung imaging, involving increased motion artefact, the necessity for averaging and data post-processing (17).

Ex vivo lung experimentation was used to study the pulmonary physiology (18-20) but has also been utilised by our group as a tool for hyperpolarized lung imaging methodology development. *Ex vivo* lung imaging comports the advantage to avoid all of the *in vivo* numerous difficulties, whilst producing physiologically relevant measurements for new hyperpolarized noble gases imaging technique developments (15, 21, 22).

1.4. Thesis overview

Research outlined in this thesis has the objective to investigate potential pulmonary disease biomarkers using hyperpolarized gas NMR and MRI. The two noble gases ^{129}Xe and ^{83}Kr are hyperpolarized to probe *ex vivo* rat lungs, taking advantage of their unique characteristics to provide spatially resolved diseases biomarkers. These biomarkers provide information on the lung physiopathology such as the alveolar radius, the presence of an enzyme or a fibrotic thickening.

Chapter 2 presents an overview of the interdisciplinary background of this thesis, from the concepts of magnetic resonance and hyperpolarized noble gases technologies, to the *ex vivo* rat lung experimentation.

Chapter 3 demonstrates the promising hyperpolarized ^{83}Kr MRI as a novel biomarker for the alveolar microstructure. The surface sensitive ^{83}Kr relaxation

allows for the discrimination of diseased and healthy lungs in an *ex vivo* rat model of the COPD emphysema.

Chapter 4 presents the first results obtained with a newly designed biosensor able to host hyperpolarized ^{129}Xe in solution. The encapsulation of the ^{129}Xe into a cryptophane A cage tethered to a paramagnetic group induces its fast relaxation. The biosensor relaxivity on the hyperpolarized ^{129}Xe is investigated and an *in vivo* enzymatic biosensor is demonstrated.

Chapter 5 examines the use of synthetic blood as a potential source of ^{129}Xe MRI contrast for interstitial diseases. Two perfluorocarbon emulsions are used as a blood replacement in *ex vivo* rat lungs to evaluate the gas transfer through the lung parenchyma.

1.5. References

1. NICE clinical guideline: Chronic obstructive pulmonary disease: management of chronic obstructive pulmonary disease in adults in primary and secondary care (partial update). In: Excellence NIfHaC, editor. 2010.
2. World Health Statistics. Geneva, Switzerland: World Health Organization; 2011.
3. NICE clinical guideline: Idiopathic pulmonary fibrosis: the diagnosis and management of suspected idiopathic pulmonary fibrosis. In: Excellence NIfHaC, editor. 2013.
4. Hatabu H, Alsop DC, Listerud J, Bonnet M, Gefter WB. T2* and proton density measurement of normal human lung parenchyma using submillisecond echo time gradient echo magnetic resonance imaging. Eur J Radiol. 1999;29(3):245-52.
5. Bergin CJ, Pauly JM, Macovski a. Lung Parenchyma - Projection Reconstruction Mr-Imaging. Radiology. 1991;179(3):777-81.
6. Stock KW, Chen Q, Hatabu H, Edelman RR. Magnetic resonance T-2* measurements of the normal human lung in vivo with ultra-short echo times. Magnetic Resonance Imaging. 1999;17(7):997-1000.
7. Woods JC, Choong CK, Yablonskiy DA, Bentley J, Wong J, Pierce JA, et al. Hyperpolarized He-3 diffusion MRI and histology in pulmonary emphysema. Magn Reson Med. 2006;56(6):1293-300.

8. Chen XJ, Hedlund LW, Moller HE, Chawla MS, Maronpot RR, Johnson GA. Detection of emphysema in rat lungs by using magnetic resonance measurements of He-3 diffusion. Proceedings of the National Academy of Sciences of the United States of America. 2000;97(21):11478-81.
9. Saam BT, Yablonskiy DA, Kodibagkar VD, Leawoods JC, Gierada DS, Cooper JD, et al. MR imaging of diffusion of He-3 gas in healthy and diseased lungs. Magn Reson Med. 2000;44(2):174-9.
10. Swift AJ, Wild JM, Fichele S, Woodhouse N, Fleming S, Waterhouse J, et al. Emphysematous changes and normal variation in smokers and COPD patients using diffusion He-3 MRI. Eur J Radiol. 2005;54(3):352-8.
11. Chen XJ, Moller HE, Chawla MS, Cofer GP, Driehuys B, Hedlund LW, et al. Spatially resolved measurements of hyperpolarized gas properties in the lung in vivo. Part I: Diffusion coefficient. Magn Reson Med. 1999;42(4):721-8.
12. Driehuys B, Cofer GP, Pollaro J, Mackel JB, Hedlund LW, Johnson GA. Imaging alveolar-capillary gas transfer using hyperpolarized Xe-129 MRI. Proceedings of the National Academy of Sciences of the United States of America. 2006;103(48):18278-83.
13. Pavlovskaya GE, Cleveland ZI, Stupic KF, Meersmann T. Hyperpolarized Krypton-83 as a New Contrast Agent for Magnetic Resonance Imaging. Proceedings of the National Academy of Sciences of the United States of America. 2005;102:18275-9.
14. Stupic KF, Elkins ND, Pavlovskaya GE, Repine JE, Meersmann T. Effects of pulmonary inhalation on hyperpolarized krypton-83 magnetic resonance T-1 relaxation. Phys Med Biol. 2011;56(13):3731-48.
15. Six JS, Hughes-Riley T, Lilburn DML, Dorkes AC, Stupic KF, Shaw DE, et al. Pulmonary MRI contrast using Surface Quadrupolar Relaxation (SQUARE) of hyperpolarized Kr-83. Magnetic Resonance Imaging. 2014;32(1):48-53.
16. Fish R, Danneman PJ, Brown M, Karas A. Anesthesia and analgesia in laboratory animals: Academic Press; 2011.
17. Wakayama T, Kitamoto M, Ueyama T, Imai H, Narazaki M, Kimura A, et al. Hyperpolarized Xe-129 MRI of the mouse lung at a low xenon

concentration using a continuous flow-type hyperpolarizing system. Journal of Magnetic Resonance Imaging. 2008;27(4):777-84.

18. Frazer DG, Weber KC. Trapped air in ventilated excised rat lungs. J Appl Physiol. 1976;40(6):915-22.

19. Herget J, Chovanec M. Isolated perfused murine lung: A well characterized preparation for studying lung vascular function. Drug Discovery Today: Disease Models. 2010;7(3-4):131-5.

20. Uhlig S, Wollin L. An Improved Setup for the Isolated-Perfused Rat Lung. Journal of Pharmacological and Toxicological Methods. 1994;31(2):85-94.

21. Lilburn DM, Tatler AL, Six JS, Lesbats C, Habgood A, Porte J, et al. Investigating lung responses with functional hyperpolarized xenon-129 MRI in an ex vivo rat model of asthma. Magn Reson Med. 2015.

22. Lilburn DML, Hughes-Riley T, Six JS, Stupic KF, Shaw DE, Pavlovskaya GE, et al. Validating Excised Rodent Lungs for Functional Hyperpolarized Xenon-129 MRI. PLoS One. 2013;8(8).

CHAPTER 2

INTRODUCTION TO MAGNETIC NUCLEAR RESONANCE AND NOBLE GAS HYPERPOLARIZATION

2.1. Purpose of the chapter

This chapter aims to provide the reader with background knowledge in basic nuclear magnetic resonance techniques, and an introduction to noble gas hyperpolarization technique, used in all of the described research in this thesis.
Most of this chapter's material that is related to nuclear magnetism and resonance are taken and adapted from the textbooks published by A. Abragam (1), P. T. Callaghan (2), M. H. Levitt (3), and E. Mark Haacke (4). In addition to these four books, the theoretical parts associated to the hyperpolarization were supported by numerous relevant publications illustrating some applications using hyperpolarized noble gases for spectroscopy and imaging.
Some more specific background about pulmonary diseases and animal models will be given in the next chapters of this thesis.

2.2. Basics of Nuclear Magnetic Resonance (NMR)

Nuclear Magnetic Resonance (NMR) is a physical phenomenon widely used in research and medical imaging applications. The NMR spectroscopy and imaging techniques are both based on the fact that nuclei placed in a magnetic field will interact with radiofrequency radiation. This interaction will cause a coherent precession of the nuclear spins that, in turn, will induce an electric signal in a surrounding receiving coil.

2.2.1. Nuclear spin properties

NMR and MRI are techniques using the properties of the atomic nuclei. The nuclei are composed of protons and neutrons that will determine the nuclear spin I. The spin is an intrinsic property of all of the subelements of the nucleons, namely the quarks. The angular momenta of all the nuclear quarks are added up, defining the nuclear spin angular momentum m. The angular momentum is used to describe the direction of the spin polarization axis. Nuclei with an odd atomic number Z or an odd mass number will have an

integer of half integer nuclear spin value $I > 0$ and will be considered NMR active. The nuclei used in this work and their properties are listed in Table 2.1.

Isotope	*Spin*	*Natural abundance (%)*	*Gyromagnetic ratio* $\gamma/10^6$ *(rad.s^{-1}.T^{-1})*	*NMR frequency at 9.4 T (MHz)*
^{1}H	1/2	100.00	267.522	400.228
^{3}He	1/2	0.000137	-203.802	-304.899
^{19}F	1/2	100.00	251.815	376.729
^{83}Kr	9/2	11.58	-10.331	-15.456
^{129}Xe	1/2	26.44	-74.521	-111.488
^{131}Xe	3/2	21.18	22.091	33.049

Table 2.1 Nuclear isotopes used in this work and their properties. Table adapted from reference (5).

In the case of a single spin placed in a static magnetic field B_0, the total energy of the nuclear spin is defined by the Hamiltonian operator $\hat{H}_z$. The Hamiltonian contains the gyromagnetic ratio γ, the magnetic field B_0 and the nuclear spin operator $\hat{I}_z$ which eigenvalues are the magnetic quantum numbers m_z (Eq. 2.1 and 2.2).

$$\hat{H}_z = -\gamma\hbar B_0\hat{I}_z \qquad \text{Eq. 2.1}$$

$$\hat{H}_z = -\omega\hat{I}_z \qquad \text{Eq. 2.2}$$

where γ is the gyromagnetic ratio of the nucleus, and $\hbar = \frac{h}{2\pi}$ with h the Planck's constant.

The eigenvalues of the Hamiltonian describe the energy of a spin state. In the absence of a magnetic field, the different nuclear energy levels of the spin states are degenerate; they all have the same ground state energy. If a magnetic field B_0 is applied along the z-axis, an energy splitting is therefore observed, producing $2I + 1$ sublevels taking the values $m_z = I, I - 1, \ldots, -I$, this is called the Zeeman splitting. NMR is the detection of this nuclear Zeeman splitting sublevels. In the energy diagram on Figure 2.1, these states are

represented by horizontal lines. The energy levels E are directly calculated from the above Hamiltonian.

$$E = -\gamma \hbar B_0 m_z \qquad \text{Eq. 2.3}$$

Any nucleus with a spin $I = 0$, will not present any Zeeman splitting at all, making them NMR silent.

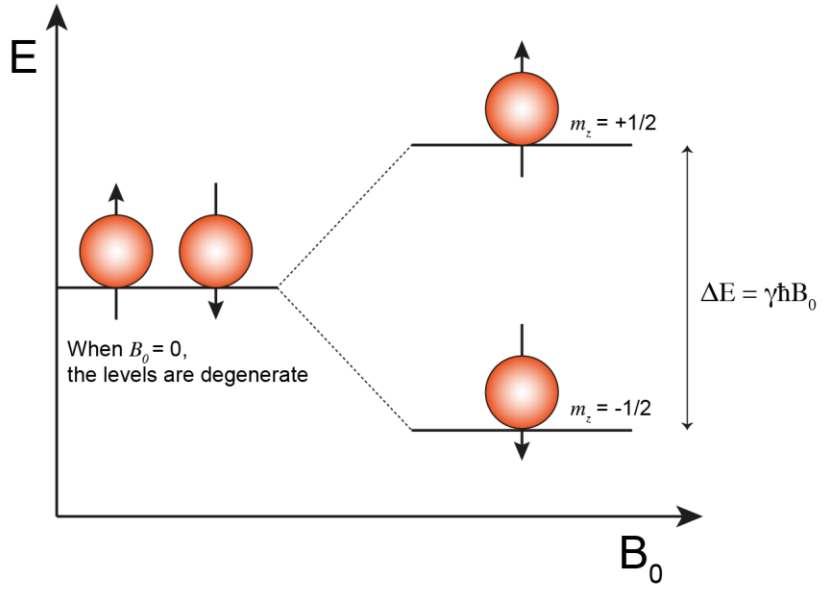

Figure 2.1 Energy level diagram for a population of two ^{129}Xe spins ($I = 1/2$). In the absence of an external magnetic field B_0, the energy levels are degenerate. The presence of an external magnetic field along the z-axis induces a Zeeman splitting of the different spin states.

Another intrinsic property of the nucleus is the magnetic moment μ caused by the nuclear magnetism. The magnetic moment μ and the nuclear spin angular momentum I are proportionally linked by a constant γ called the gyromagnetic ratio (Eq. 2.4). Magnetic moments can be described as vectors $\vec{\mu}$ defining the spin polarization. The magnetic moment takes the value:

$$\mu = \gamma . \hbar . I \qquad \text{Eq. 2.4}$$

where γ is the gyromagnetic ratio (see Table 2.1), $\hbar$ the Planck's constant divided by 2π and I the nuclear spin angular momentum.

In the absence of magnetic field, the vectors are randomly oriented, resulting in no net magnetization ($\sum \mu = 0$) (Figure 2.2.a). In the presence of a static magnetic field B_0, the magnetic moments will align with the direction of the

field, inducing an anisotropic spin polarization distribution ($\sum \mu > 0$) (Figure 2.2.b). This positive net magnetization at thermal equilibrium is called the macroscopic magnetization, $M_0 = \sum \mu$.

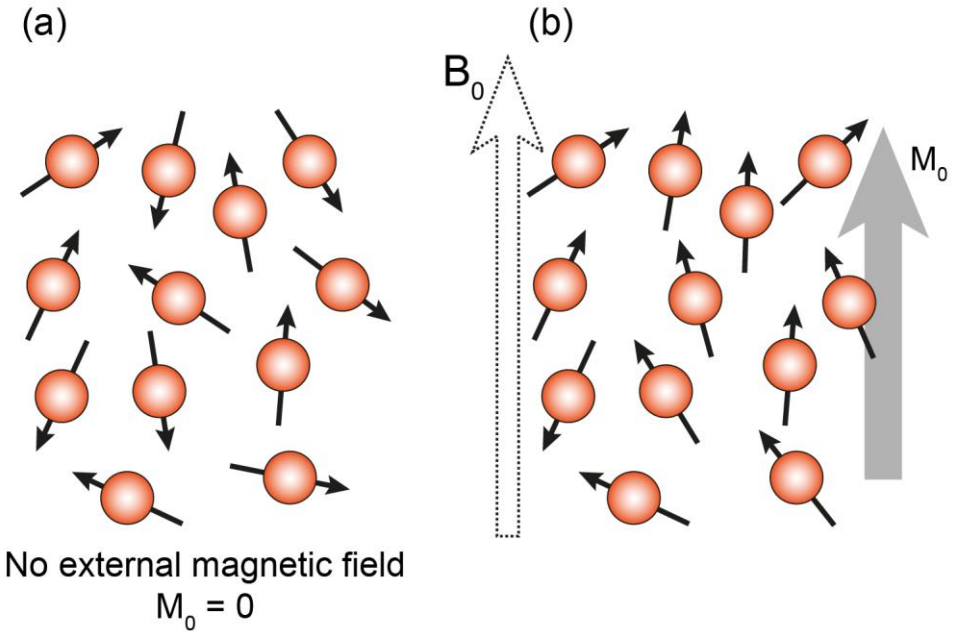

Figure 2.2 (a) Isotropic distribution of the magnetic moments in the absence of magnetic field. (b) Anisotropic distribution of the magnetic moments in the presence of a static magnetic field B_0 yielding a macroscopic magnetization $M_0 > 0$.

As discussed in the previous paragraph, the external magnetic field will orientate the spin polarization. The angular momenta will precess around the axis formed by the magnetic field B_0. The frequency of precession is called the Larmor frequency ω_0 (Eq. 2.5), and is directly proportional to the gyromagnetic ratio γ of the nucleus and the magnetic field B_0 applied to the nucleus:

$$\omega_0 = -\gamma . B_0 \qquad \text{Eq. 2.5}$$

The Larmor frequency can be positive or negative, depending on the sign of the gyromagnetic ratio (see Figure 2.3). That implies the angular momentum of different nuclei may precess in different directions around the magnetic field axis. For a positive gyromagnetic ratio, the Larmor frequency is negative, and the nucleus will precess clockwise around the field (when looking from the top of the field). For both noble gases nuclei ^{129}Xe and ^{83}Kr used in this thesis, the

gyromagnetic ratio is negative, implying an anticlockwise Larmor precession around B_0.

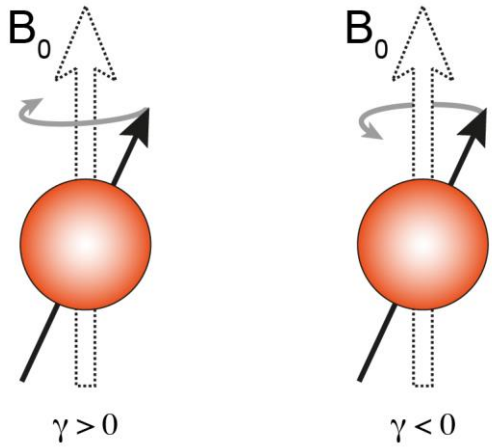

Figure 2.3 Precession of the nuclear spin magnetic moment around the external magnetic field axis for a spin with positive or negative gyromagnetic ratio. Figure adapted from (3).

2.2.2. Polarization at thermal equilibrium

The uneven spin population distribution in each Zeeman energy levels will induce a very small magnetization. This macroscopic magnetization M_0 is oriented parallel or anti parallel to the external magnetic field (Figure 2.2.b). It is called the longitudinal magnetization M_z. This magnetization will be directly dependent on the difference of population of the spin orientations.

At thermal equilibrium, given a temperature T, the spin population in each energy state follows the Boltzmann distribution. This means the spin density $\rho_{eq,i}$ at a spin state i will be equal to:

$$\rho_{eq,i} = \frac{N_i}{\sum_i N} = \frac{\exp\left({}^{-E_i}/_{k_B T}\right)}{\sum_{-I}^{I} \exp\left({}^{-E_i}/_{k_B T}\right)} \qquad \text{Eq. 2.6}$$

where $E_i = -\gamma \hbar B_0 m_i$ is the energy at the spin state i.

The polarization of a spin system is proportional to the longitudinal magnetization at thermal equilibrium. It corresponds to the ratio of the longitudinal magnetization over its maximum value. Therefore, for a spin $1/2$, e.g. ^{129}Xe, where $N\uparrow$ and $N\downarrow$ are the number of spins in each energy level, the polarization P is equal to:

$$P = \frac{N\uparrow - N\downarrow}{N\uparrow + N\downarrow} \quad \text{Eq. 2.7}$$

$$P = \frac{\exp\left(-\gamma\hbar B_0 / 2k_B T\right) - \exp\left(\gamma\hbar B_0 / 2k_B T\right)}{\exp\left(-\gamma\hbar B_0 / 2k_B T\right) + \exp\left(\gamma\hbar B_0 / 2k_B T\right)} \quad \text{Eq. 2.8}$$

The thermal energy is always much bigger than the energy between two Zeeman sublevels, therefore making the thermal equilibrium spin populations difference very small. Because the high temperature limit is met, i.e. $\frac{E_i}{k_B T} \ll 1$, the polarization equation for a spin $1/2$ can be simplified to:

$$P = \frac{|\gamma|\hbar B_0}{2k_B T} \quad \text{Eq. 2.9}$$

The polarization is directly dependent on the magnetic field B_0 but also, the gyromagnetic ratio γ. This is of particular importance when handling nuclei with low gyromagnetic ratio such as ^{83}Kr.

The longitudinal magnetization M_z, or thermal equilibrium polarization, corresponds to a very small population difference between the energy levels and is almost undetectable. It is defined by:

$$M_z = M_0 = \frac{N\gamma\hbar}{2} P = \frac{N\gamma^2\hbar^2 B_0}{4k_B T} \quad \text{Eq. 2.10}$$

We will see in the next section how the polarization induced by the magnetic field can be measured.

2.2.3. Excitation and detection of the NMR signal

This section describes how to excite the nuclear spin in the system and detect the signal from it. Some considerations for the construction of a custom-built ^{129}Xe coil for the *in vivo* preclinical MRI Bruker scanner, located in the psychology department of the University of Nottingham, are given in the Appendix 1.

The application of an oscillatory field in the radio frequency (RF) range, with a frequency ν equal to the Larmor frequency of the sample spins will induce a Zeeman energy level transition. The energy absorbed by the system to induce the energy levels transition is equal to the difference between $E_{-1/2}$ and $E_{1/2}$ (Eq. 2.11).

$$\Delta E = E_{-1/2} - E_{1/2} = \gamma \hbar B_0 = -\gamma \omega_0 \qquad \text{Eq. 2.11}$$

The RF pulse induces a phase coherence of the spins, generating a non-zero transverse magnetization M_{xy}, polarizing the bulk polarization off the z-axis (Figure 2.4). When the RF pulse is turned off, all of the spins will start precessing around the z-axis again, inducing the rotation of the transverse magnetization M_{xy} in the xy-plane at the Larmor frequency. The transverse magnetization M_{xy} will decay from M_0 to zero, while the longitudinal magnetization M_z will recover its equilibrium value M_0 over time. The precession of the bulk magnetization produces an oscillating electric current in the detection coil (usually the same as the excitation coil). The signal will decay because of dephasing described by the rate constant T_2^* (transverse relaxation) and the decaying signal detected by the coil is called the free induction decay (FID). Relaxation mechanisms related to hyperpolarized systems are explained further on this chapter.

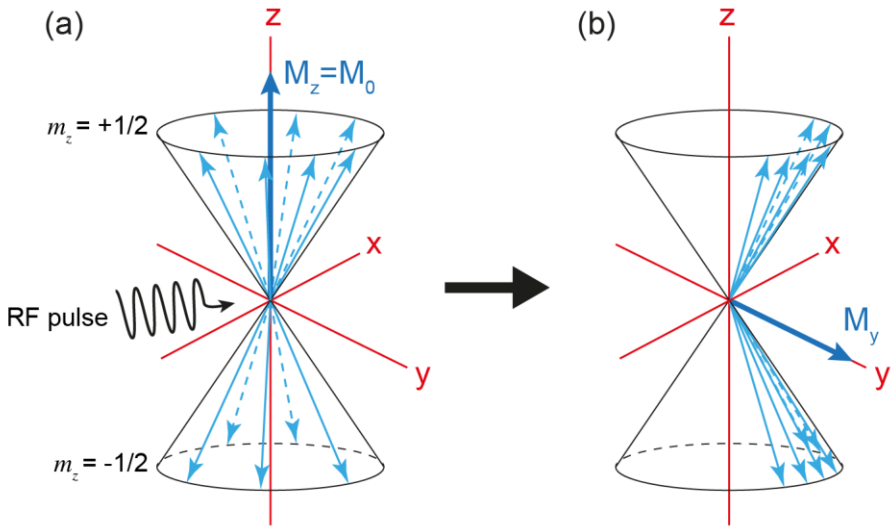

Figure 2.4 Excitation of a sample of spins $1/2$. (a) The Boltzmann distribution of the spins at thermal equilibrium produces a bulk magnetization along the z-axis (along B_0), the spins have random phases. (b) The application of a RF pulse induces the phase coherence of the spins, leading to a magnetization M_y in the transverse plane.

2.3. Hyperpolarization through spin exchange optical pumping (SEOP)

NMR and MRI of gas phase nuclei is challenging as compared to conventional MRI that images hydrogen atoms contained in the human tissue. This is due to the low density of a gas as compared to nuclei in the condensed state, and its associated low signal intensity. One way to increase the signal would be to increase the number of spins by increasing the gas pressure. Highly pressurised thermal samples are used to measure the thermal polarization of a gas sample; it is however not a practical option when used for pulmonary application for example.

Different strategies can be used to enhance the polarization. The polarization equation (Eq. 2.9) states that the polarization is dependent on the gyromagnetic ratio of the nucleus γ, the static magnetic field B_0 and the temperature T. By consequence, in identical conditions ^{129}Xe will provide a 7-fold stronger polarization than ^{83}Kr. However, an increase of the magnetic field often limits the working space in the magnet bore, and cooling down a sample can be impracticable when doing preclinical or clinical studies.

Hyperpolarization is a technique that creates a low spin temperature, enabling high polarization values at low pressure and ambient temperature. The work presented in this thesis utilises the spin exchange optical pumping (SEOP) hyperpolarization technique, which is the most commonly used method to hyperpolarize noble gases such as ^{3}He, ^{129}Xe and ^{83}Kr. Other existing techniques to hyperpolarize noble gases are being developed, for example metastability exchange optical pumping (MEOP) that has been efficiently used to hyperpolarize ^{3}He (6), dynamic nuclear polarization (DNP) has been applied to ^{129}Xe in its liquid phase, directly followed by its sublimation (7), and ^{129}Xe 'brute-force' hyperpolarization by placing the system at very low temperature of the mK range to hyperpolarize the spins, followed by a rapid heating of the system (8).

The primary aim of SEOP is to increase the sensitivity of the spectroscopy by increasing the longitudinal magnetization M_z to overcome the low signal as discussed above (Figure 2.5). The purpose of this method is to obtain highly non-equilibrium nuclear spin polarization.

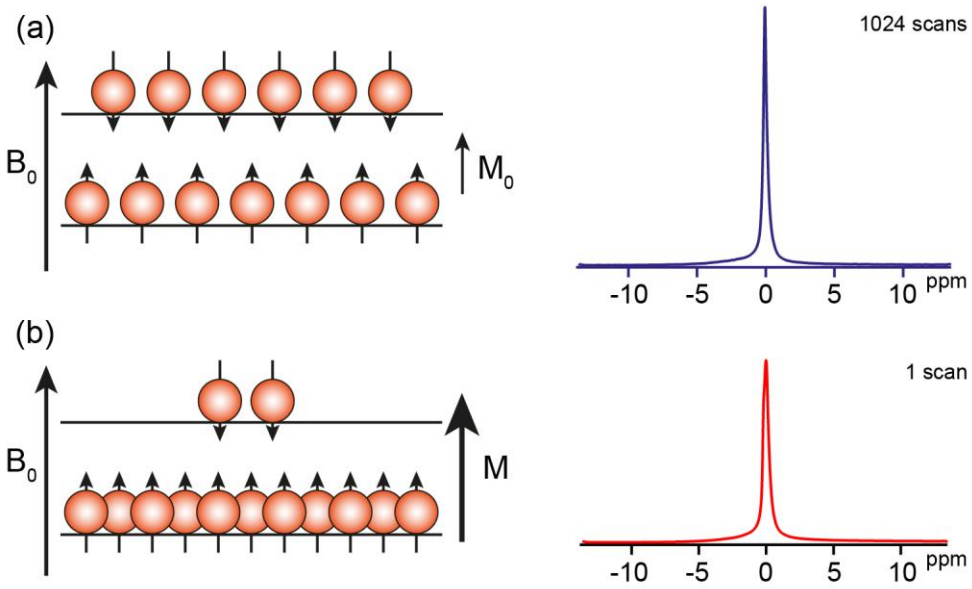

Figure 2.5 (a) Spin energy levels distribution and ^{129}Xe signal at thermal equilibrium and corresponding spectrum, acquired with 1024 averages (scan duration: 4h 40min) (b) Spin energy levels distribution and ^{129}Xe signal after enhancement by spin exchange optical pumping hyperpolarization and its corresponding spectrum, acquired in a single scan (scan duration: 6 s). At thermal equilibrium the spin population difference is very small, the signal has been averaged, producing a signal-to-noise ratio, $SNR = 3000$. After hyperpolarization, a single scan allows for a 5-fold SNR enhancement ($SNR = 14000$). Note that the thermal sample was containing 8 bar Xe – 1 bar O_2 (total pressure, 9 bar), and the hp gas mixture 25 % Xe – 75 % N_2 was hyperpolarized for 6 min at 316 K and 682 mbar, for a detection pressure of 0.42 bar after recompression. Representative spectra acquired for recompression unit tests (see Section 2.3.3.).

The studies in this thesis only employ the SEOP technique with the existing laboratory equipment, and without analysing nor improving the method, a brief description of spin exchange optical pumping hyperpolarization is given in this section to provide a general understanding to the reader. The SEOP hyperpolarization process can be divided into two steps, optical pumping of the alkali metal and spin exchange with the noble gas.

2.3.1. Optical pumping of the alkali metal

The SEOP cell containing the noble gas and the alkali metal rubidium is placed in a magnetic field produced by Helmholtz coils (15.54 mT) to induce the Zeeman splitting of rubidium (Rb). The SEOP cell is also heated with warm air to produce a rubidium vapour of appropriate density. Alkali metals such as rubidium or cesium are used because they have a single unpaired electron on their valence shell.

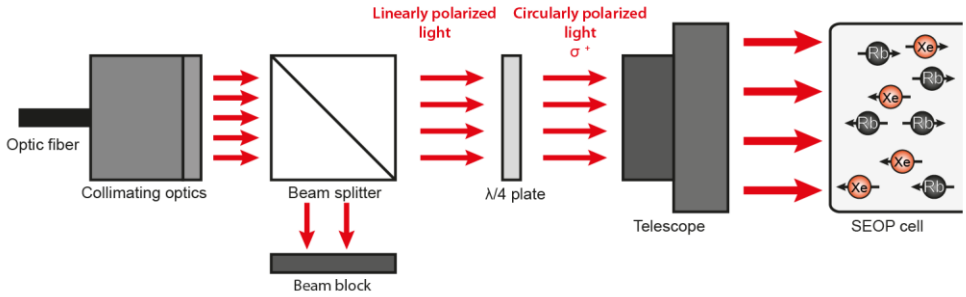

Figure 2.6 Schematics of the optics components of the polarizer. The laser light is transmitted to an optic fibre. A collimator focuses the light on a beam splitter, placed 25 mm away. The beam splitter linearly polarizes the light beam. The light then goes through a quarter-wave plate (λ/4 plate) that circularly polarizes the beam. Finally, the beam is expended with a telescope to create a parallel beam having a diameter of the size of the SEOP pumping cell holder front window.

The laser light is circularly polarized using a beam splitter and a quarter-wave plate as described in Figure 2.6. In general words, the circularly polarized laser is tuned to the D_1 transition of the valence electron of the Rb (794.7 nm), present in the vapour state in the SEOP pumping cell. It will induce the transition of the angular momentum from the light to the electron spin. Resulting to the selection rule, the angular momentum is preserved and excitation will only happen from the $m = -1/2$ sublevel of the $^2S_{1/2}$ state to $m = +1/2$ of the $^2P_{1/2}$ state (Figure 2.7). We say the electrons are in their excited state. Some collisions between Rb atoms will induce mixing of the excited states. The electrons will then decay back to their ground state. Due to ongoing laser pumping, the population of spins in the $m = -1/2$ sublevel of the $^2S_{1/2}$ state is continuously depleted by the circularly polarized light excitation, therefore increasing the population in the $m = +1/2$ sublevel.

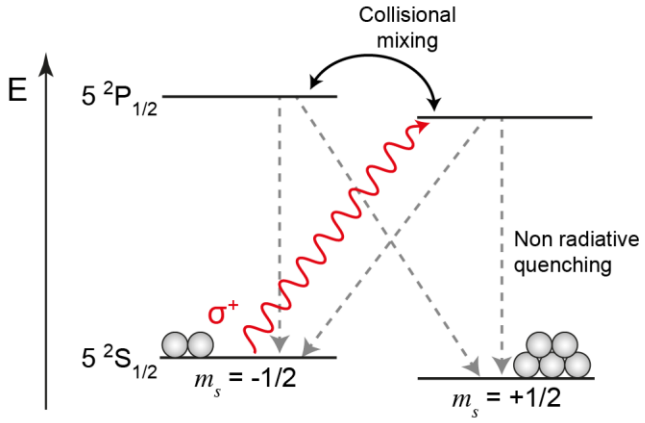

Figure 2.7 A left circularly polarized laser optically pumps the alkali metal electron. The sublevel $m_s = +1/2$ is populated through the continuous pumping of the $m_s = -1/2$ by the laser, tuned at its D_1 transition.

Nitrogen (N_2) is included to the gas mixture, alongside with the noble gas, in order to quench the radiation caused by the relaxation of the excited electrons to their ground states. Instead of releasing the energy by emitting a photon that would be deleterious for the polarization build-up of the Rb, the energy is converted into the N_2 vibrational mode.

2.3.2. Spin exchange to the noble gas

The transfer of polarization is done by spin exchange that will transfer the angular momentum from the alkali metal electron spin to the noble gas nuclear spin. As illustrated in Figure 2.8, it can be accomplished by two processes: binary collisions or van der Waals complexes formation. Binary collision is the main spin exchange mechanism for ^{83}Kr, whereas ^{129}Xe will also undergo spin exchange through van der Waals complexes. In both cases, the energy transfer happening during the contact between the alkali electron spin and the noble gas nuclear spin induces a flip flop of the Rb electron spin and the noble gas nuclear spin, increasing the populations of noble gas atoms with the same nuclear spin orientation.

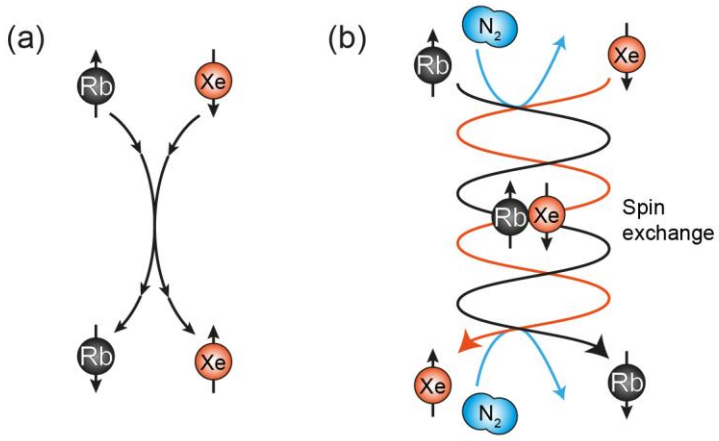

Figure 2.8 Alkali metal spin exchange between a rubidium electron spin and a ^{129}Xe nuclear spin by (a) collision and (b) van der Waals interaction (three-body collisions).

2.3.3. Parameters involved in the polarization efficiency

The use of very diluted noble gases mixtures requires cryogenic separation after SEOP hyperpolarization. However, this cryogenic concentration is not a feasible process in the case of ^{83}Kr, due to its fast quadrupolar relaxation in the condensed phase that would lead to almost complete depolarization (9). An alternative to this is to hyperpolarize a higher concentration of noble gas, but at lower pressure. The polarization equipment in our laboratory has been adapted to such applications. Most parameters involved in the polarization level have been studied by Six et al. and published in the online journal PloS One in 2012 (9).

The polarization level of any nucleus placed in a magnetic field is defined by Eq. 2.9. The polarization of a known sample (see Figure 2.5(a) for example) at thermal equilibrium is calculated before each hyperpolarized gas experiment. This measurement will be used to define the polarization of the hyperpolarized gas after SEOP. The signal intensity recorded during shuttle delivery hyperpolarized gas experiments also requires taking into account the N_2 buffer gas. It is easy to understand that the actual noble gas polarization has to be scaled to the dilution of the noble gas in the gas mixture. The apparent polarization P_{app} takes into account this dilution factor:

$$P_{app} = P \cdot \frac{P_{NG}}{P_{tot}} \qquad \text{Eq. 2.12}$$

where P_{NG} is the polarization in the pure noble gas, and P_{tot} the SEOP pressure, including the buffer gas. The highest polarization levels were

obtained using 40-50 % xenon and 25 % krypton gas mixtures, with $P_{app}^{max} = 15.5\%$ and $P_{app}^{max} = 4.4\%$ respectively.

The polarization is shown to increase as the total SEOP cell pressure was decreased from 3.5 bar to a maximum polarization reached at around 0.2 – 0.3 bar for ^{129}Xe and 0.35 – 0.5 bar for ^{83}Kr. When the pressure decreased from the optimum pressure, the polarization is rapidly decreasing to zero.

The temperature is another important parameter involved in the formation of a high-density rubidium vapour. A higher SEOP hyperpolarization temperature has been shown to be beneficial to ^{83}Kr, counteracting the lower Rb-^{83}Kr exchange rate, but also reducing the quadrupolar relaxation on the SEOP cell surface. The highest polarizations have been reached with 373 K for ^{129}Xe and 433 K for ^{83}Kr.

To summarize, our laboratory settings allow the steady state spin polarization to be reached after 6 min of hyperpolarization at 373 K for ^{129}Xe and 8 min at 433 K for ^{83}Kr.

The drawback of using the highest polarization pressure conditions is that it cannot be delivered without recompression to ambient pressure. The idea of recompression of the gas was already used for metastability-exchange optical pumping applications (10). Similarly, for all imaging experiments in this work, a piston has been used to recompress the gas to ambient pressure before being delivered to excised lungs. This method consists in delivering the gas directly from the SEOP cell to a pre-vacuumed recompression chamber by gas expansion, and to subsequently recompress it by pushing a piston in the back of the chamber with pressurized nitrogen gas (11). Recompressed hyperpolarized gas was shown to not significantly alter the polarization of the noble gas. Up to 100 % and 75 % of the spin polarization was maintained for ^{129}Xe and ^{83}Kr respectively.

2.4. Relaxation mechanisms

Instead of directly measuring the longitudinal magnetization, NMR will measure the magnetization that is perpendicular to the magnetic field B_0, called the transverse magnetization M_{xy}. At thermal equilibrium in a large magnetic field, this transverse magnetization is null.

2.4.1. Transverse relaxation

After the application of a 90 ° RF pulse, the spins will be in phase coherence, forming a transverse magnetization as seen in Figure 2.4. From the time the RF pulse is off, the spins start losing their synchrony due to the presence of slightly difference local magnetic fields from the influence of neighbouring spins. Their phase will start cancel each other out over time; this loss of phase coherence will therefore induce an irreversible transverse magnetization relaxation, also called the spin – spin relaxation, or T_2 relaxation. The relaxation behaviour of M_{xy} can be describe by an exponential decay as follow:

$$M_{xy}(t) = M_0 e^{-t/T_2} \qquad \text{Eq. 2.13}$$

where t is the time after tipping the magnetization in the xy-plane and M_0 is the initial transverse magnetization.

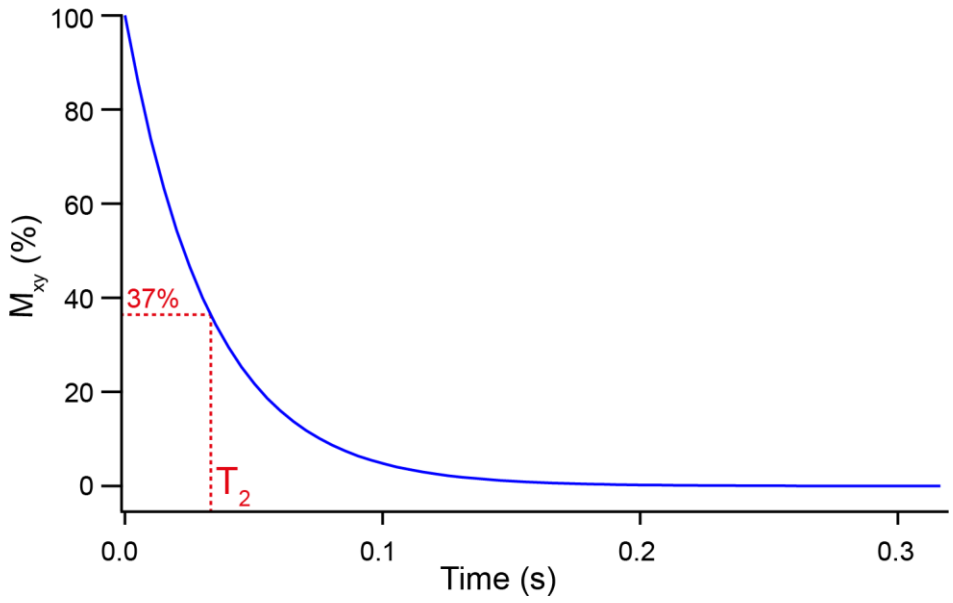

Figure 2.9 Transverse magnetization (M_{xy}) relaxation of ^{129}Xe after full excitation with a 90 ° RF pulse. The transverse relaxation constant T_2 corresponds to the time passed where M_{xy} = 37 %.

On the envelope of the FID, the transverse decay that is actually observed is the T_2^* relaxation decay that also takes into account B_0 field inhomogeneities. T_2^* is directly measured from the envelope of the FID and is linked to T_2 and $T_{2,inhomo}$ by the relation in Eq. 2.14.

$$\frac{1}{T_2^*} = \frac{1}{T_2} + \frac{1}{T_{2,inhomo}} \qquad \text{Eq. 2.14}$$

	T_2 *(ms)*	T_2^* *(ms)*
^{129}Xe	32.9 ± 0.5	1.77 ± 0.37
^{83}Kr	166 ± 11	13.1 ± 0.8

Table 2.2 Transverse relaxation constants of the two nuclei of interest ^{129}Xe and ^{83}Kr, in the gas phase in the absence of oxygen, in *ex vivo* rat lungs, recorded at 9.4 T in the laboratory Bruker spectrometer. Data taken from J.S. Six PhD thesis (12).

Experimental T_2 and T_2^* were measured in *ex vivo* lungs and displayed in Table 2.2. The transverse relaxation is of particular importance in imaging sequences such as the gradient-echo sequence, where the signal is recorded a long time after the RF excitation pulse, making it more complicated for systems with short T_2.

2.4.2. Longitudinal relaxation

First let's consider a thermal system, e.g. an ensemble of ^{1}H. After a RF excitation pulse, as the transverse magnetization M_{xy} decreases, the longitudinal magnetization M_z grows back to its initial thermal value M_0. The M_{xy} regrowth process is called the longitudinal relaxation, or spin – lattice relaxation and is defined by Eq. 2.15.

$$M_z(t) = M_0(1 - 2e^{-t/T_1}) \qquad \text{Eq. 2.15}$$

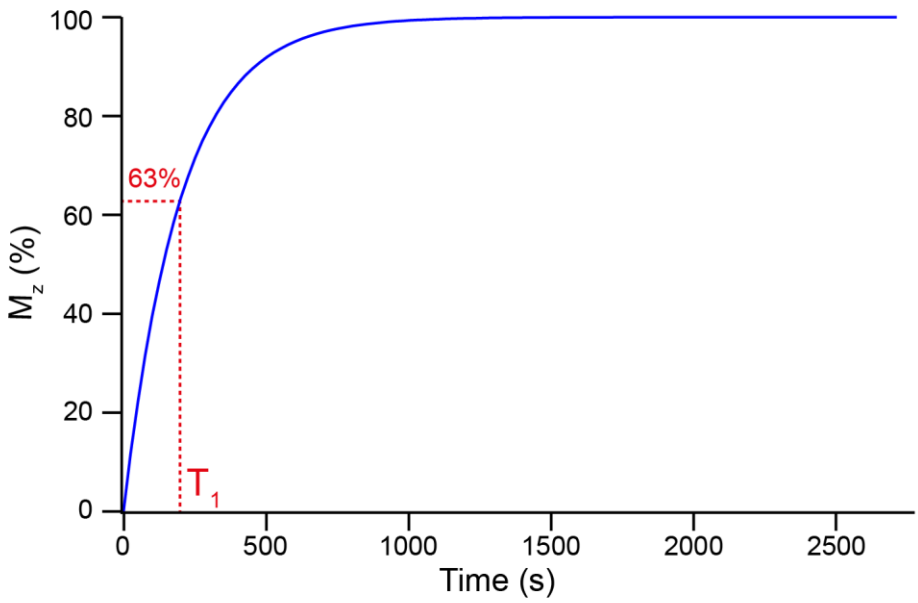

Figure 2.10 Longitudinal magnetization (M_z) evolution as a function of time after a full 90 ° excitation pulse. Magnetization recovery resulting to $M_z = 63$ % occurs when the time passed equals the longitudinal relaxation constant T_1

This phenomenon is caused by interactions of the nuclear spins with the surrounding nuclear spins magnetic fields (the lattice). The spins will return to their lower energy state with time.

In the case of hyperpolarized noble gases, the system has been hyperpolarized such that the initial longitudinal magnetization before RF excitation is much greater than the thermal equilibrium polarization. The T_1 relaxation is the mechanism by which the spins will return to their thermal equilibrium, inducing the decay of the longitudinal magnetization to thermal equilibrium magnetization.

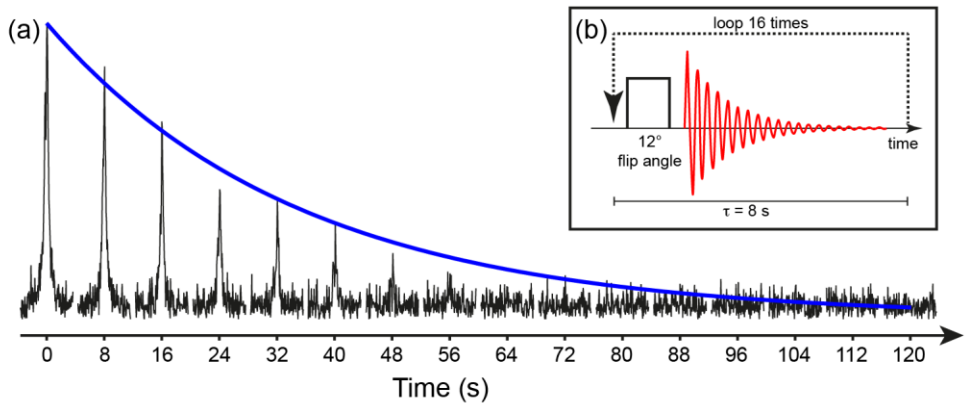

Figure 2.11 (a) Small flip angle train of spectra. A fit of the Eq. 2.16 is displayed in blue, illustrating the longitudinal relaxation mechanism. (b) Schematics of the small flip angle pulse sequence. Example taken from Chapter 4.

T_1 is obtained by using a small flip angle train of excitation pulses (Figure 2.11.b). The longitudinal magnetization after the n-th pulse will be dependent on the T_1 relaxation (s), but also on the flip angle θ (rad) as described in Eq. 2.16 (13).

$$M_z(n) = M_z(0) \times cos^n(\theta) \times e^{-n \times \tau / T_1} \qquad \text{Eq. 2.16}$$

where τ (s) is the repetition time between two pulses.

The flip angle was set to 6 to 24 °, depending on the signal intensity of the hp gas in the medium. A weak signal such as dissolved ^{129}Xe signal will require a high flip angle, whereas a strong gas phase signal will allow the use of a very low flip angle. Flip angles and delays were calibrated before each experiment, and are specified in each experimental chapter's methodological part.

Experimental T_1 values for hyperpolarized ^{129}Xe and ^{83}Kr recorded in *ex vivo* lungs are displayed in Table 2.3. The longitudinal relaxation of ^{129}Xe is drastically shortened to ~20 s by the presence of 21 % oxygen in the case of *in vivo* experiments.

	T_1 (s)
^{129}Xe	200 ± 20
^{83}Kr	1.25 ± 0.07

Table 2.3 Longitudinal relaxation constants of the two nuclei of interest ^{129}Xe and ^{83}Kr, in the gas phase in the absence of oxygen, in *ex vivo* rat lungs, recorded at 9.4 T. ^{129}Xe and ^{83}Kr data are taken from reference (11), and (14) respectively.

2.6. Magnetic Resonance Imaging (MRI) methods using hyperpolarized systems

When NMR defines the sample at the atomic and molecular levels, it however does not give any spatial information inside the RF coil. MRI allows the spatial resolution of quantitative NMR data. More precisely, a spatial dependency of the frequency and the phase properties of the nuclear spin is created by varying the magnetic field across the sample. Multi-dimensional data sets are acquired in the form of a spatial frequency image called k-space. The k-space is the Fourier transform of the image. The image is reconstructed by calculating the inverse Fourier transform of its corresponding k-space.

An overview of the mechanisms involved in the k-space discrete sampling is given in this section, adapted to the construction of a typical image oriented the zy-plane of the MRI scanner, with a slice oriented along the x-axis, which was the most used geometry in this thesis.

2.6.1. Spatial encoding using magnetic field gradients

The spatial encoding of the NMR signal is realised by applying magnetic field gradients to the sample in addition to the static magnetic field B_0. The magnetic field gradients are linear along the x-, y- and z- axes, and will produce a very unique local magnetic field aligned with B_0 at every point of the sample. The spins will experience different local magnetic field corresponding to a combination of the static magnetic field and the linear field gradient, $B_0 + xG$, where G is a given gradient in x, y or z (Figure 2.12).

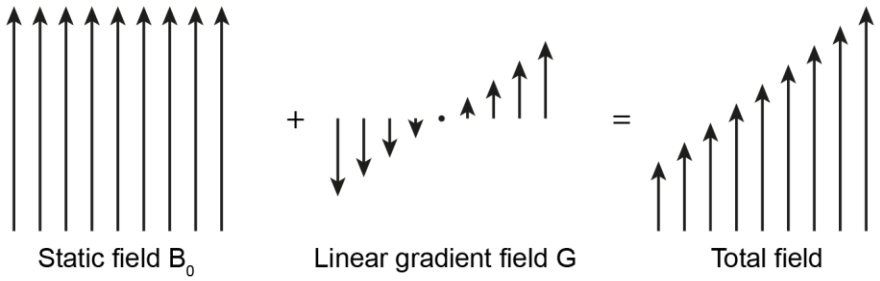

Figure 2.12 Magnetic field representation along the x-, y- or z-axis. The linear gradient field is added to the static field from the superconducting magnet, generating a very unique total magnetic field, dependent on the spatial location along the gradient axis.

Frequency-encoding gradient In the presence of a magnetic field gradient along the z-axis, the spins experience different local magnetic fields, and therefore resonate at slightly different Larmor frequencies when located at different coordinate along the z-axis. Eq. 2.17 describes how a spin located at the coordinate z will precess under a total magnetic field composed of the static magnetic field B_0 and a gradient field G_z.

$$\omega_0 = \gamma(B_0 + xG_z) \qquad \text{Eq. 2.17}$$

The local spatial distribution of the spins across the sample at a given location can be directly determined from the frequency content of the MR signal. This frequency-encoding gradient is used to define the direct direction of the k-space (Figure 2.13.A). The inverse Fourier transform of the signal made of spatial frequencies will be directly proportional to the spin density at a location x, giving a spin density profile. The field-of-view (FOV) in the frequency-encoding gradient direction is defined by:

$$FOV_z = \frac{1}{\upsilon \times G_z \times DW} \qquad \text{Eq. 2.18}$$

where ν is the gyromagnetic ratio of the nucleus in Hz/T, G_x is the strength of the frequency-encoding gradient in T/m and DW is the dwell time (sampling interval) in s.

Phase-encoding gradient After a flip angle in applied, identical spins in an identical environment will spin at the same Larmor frequency. This can be altered by a gradient applied along the y-axis. The spins will now experience different local magnetic fields, and will be precessing at different frequencies. The gradient causing this dephasing is called the phase-encoding gradient. The number of phase-encoding gradient increments and the phase-encoding gradient strength will define the resolution in the second direction of the image Figure 2.13.A). The FOV in the phase-encoding gradient direction is defined by:

$$FOV_y = \frac{1}{\upsilon \times \Delta G_y \times \delta} \qquad \text{Eq. 2.19}$$

where ν is the gyromagnetic ratio of the nucleus in Hz/T, ΔG_y and δ are the strength of the phase-encoding gradient step in T/m and the duration of the phase-encoding gradient in s respectively.

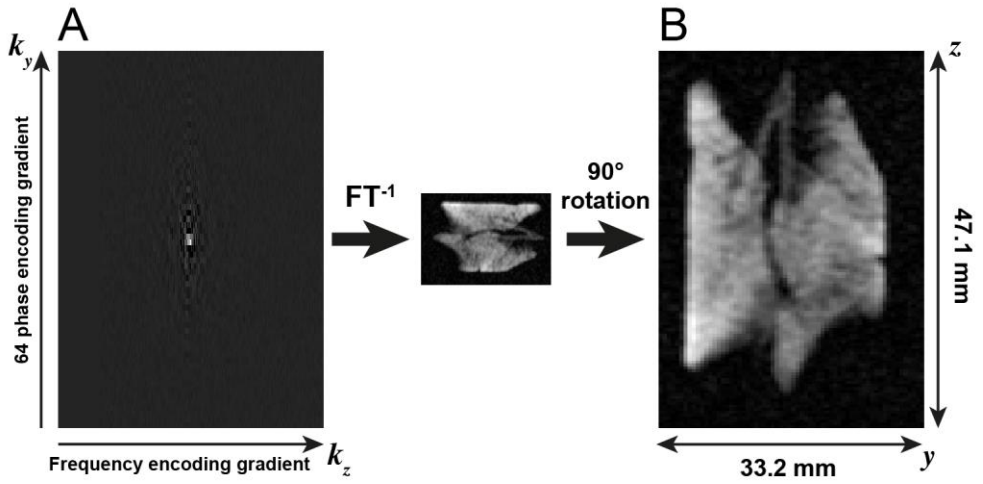

Figure 2.13 (A) Example of k-space sampled using a gradient-echo pulse sequence with 256 complex points echo acquisition and 64 phase-encoding steps. The frequency-encoding gradient was set along the z-axis, and the phase-encoding gradient along the y-axis. (B) Corresponding 128 x 64 image after inverse Fourier transform and rotation of the matrix.

Slice selection The selective excitation of a slice is realised thanks to the use of a gradient in the third direction, combined to the application of a spatially selective RF pulse. The best slice profile is reached using a sinc RF pulse that will give, after inverse Fourier transform a frequency distribution with rectangular profile, or bandwidth. A linear gradient is applied in the z-direction orthogonal to the x-axis of the slice, so that only a slice will be excited by the RF pulse. The frequency of the RF pulse will define the position of the slice and its spin density profile. The slice thickness is defined by the RF pulse bandwidth BW in Hz and the gradient strength G_z in T/m:

$$Slice\ thickness_z = \frac{BW}{\upsilon \times G_z} \qquad \text{Eq. 2.20}$$

where ν is the gyromagnetic ratio of the nucleus in Hz/T.

The slice-encoding gradient is followed by a rephasing lobe (Figure 2.14.A) to compensate the dephasing of the slice spins during the slice-selective gradient.

In this work, all imaging experiments have been conducted using gradient-echo imaging with a linear sampling of the k-space, from negative to positive phase-encoding gradient. The next sections outline the gradient-echo imaging method, and the rapid acquisition technique gradient-echo technique fast low angle shot (FLASH). Finally, the variable flip angle (VFA) adaptation of the FLASH sequence for hyperpolarized systems is described.

2.6.2. Gradient-echo imaging

Imaging sequences consists in building a k-space by putting together the frequency encoding, the phase encoding, and the slice selection if necessary. In order to fill the k-space with negative and positive frequency values, an echo is formed by the use of gradients. The echo was first introduced in spin-echo sequences in 1950 by Erwin Hahn (15), constituted of two RF pulse, a 90 ° pulse followed by a second pulse (ideally a 180 ° pulse), also called refocusing pulse. The spins will begin to dephase just after the 90 ° pulse. The 180 ° pulse will induce the tipping of the spins in the xy-plane, inversing their phase. All the spins will return to the zero-phase point at the same time equal to two times the interpulse delay, called the echo time.

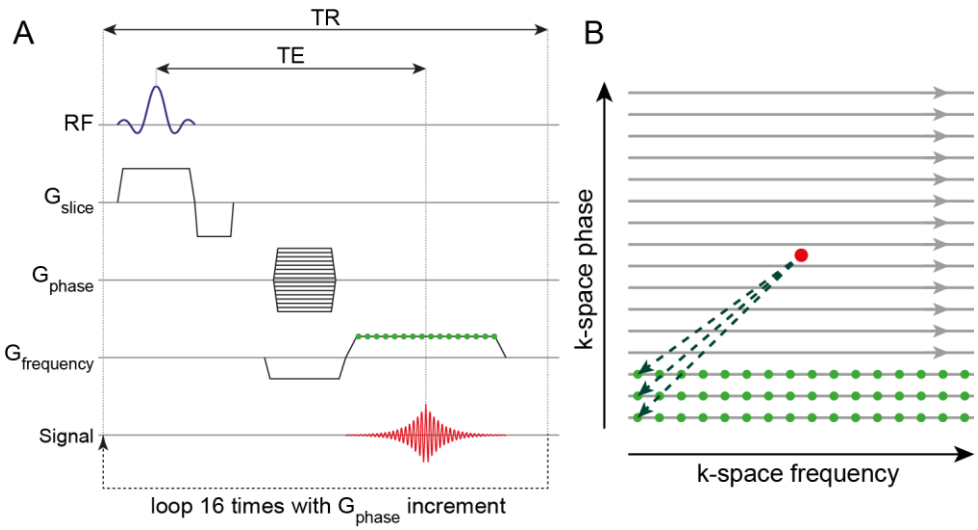

Figure 2.14 (A) Gradient-echo sequence diagram for the coverage of a 16 x 16 k-space matrix with 16 RF excitations. A sinc RF pulse is applied in concomitance with the slice-selection gradient. The echo is induced by a set of two lobes of frequency-encoding gradients of opposite polarity. The k-space is covered using a step increment of the strength of the phase-encoding gradient. The echo time TE is the time between the centre of the RF pulse and the centre of the echo. The repetition time TR is the time for each phase-encoded loop. (B) k-space diagram of the coverage by linear sampling of a 16 x 16 matrix, starting from the most negative phase-encoding gradient value. The red dot represents the (0,0) point where the phase and the frequency are null. The dashed arrows represent the trajectory in the k-space when the phase-encoding and frequency-encoding gradients are applied simultaneously. The discrete sampling of the 16 data points is illustrated by the green dots.

In the gradient-echo imaging sequence, the same idea of refocusing the spins is used. The spins are dephased by a first gradient, and will be rephased using a gradient of opposite sign. The echo will be created by a frequency-encoding gradient composed of two lobes of opposite sign. The gradient-echo sequence is illustrated in Figure 2.14. The slice-selection gradient is applied with the RF pulse, and followed by a rephasing gradient, so that the spins in the slice are in phase. The first frequency-gradient lobe is negative and dephases the spin. A phase-encoding gradient is applied simultaneously with the dephasing frequency-encoding gradient, to encode the second direction of the k-space. The second frequency-gradient positive lobe is of the same amplitude as the defocusing frequency-encoding gradient, but twice as long and of positive sign. The change of sign of the gradient induces a rephasing of the spins and creates an echo similar to the spin-echo, in the middle of the positive rephasing gradient. The frequency-gradient lobe producing the echo is also called the read-gradient as the data are discretely sampled during the echo time.

The phase-gradient encoding strength is incremented N times from $-G_{max}$ to $+G_{max}$ to cover the k-space. The maximum signal intensity is reached when the phase-gradient strength is set to zero.

2.6.3. Variable flip angle (VFA) fast low angle shot (FLASH) imaging sequence

The gradient-echo sequence presented in the previous section implies the transverse magnetization has completely depleted before the next incremental loop is started. This way, we get a steady-state magnetization for each k-space line. The introduction of low flip angle gradient-echo sequence has significantly fastened image acquisition of thermal systems, such as ^{1}H, by reducing the TR to values lower than T_2 (16). This fast low angle shot (FLASH) sequence is commonly used for hyperpolarized noble gas imaging, allowing the utilization of only a small part of the initial non-renewable longitudinal magnetization for each RF excitation pulse. The remaining longitudinal polarization after n RF excitation pulses is proportional to $(cos\theta)^n$, where θ is the flip angle, leading to a signal decrease during the course of the k-space acquisition. Zhao et al. developed the variable flip angle FLASH pulse sequence (VFA FLASH) (17). This imaging method adapted

from the FLASH sequence maximises the amount of polarization that is used during the image acquisition by increasing the flip angle during the course of the image acquisition, up to 90 °, compensating for the polarization loss created by the preceding pulse (i.e. for the preceding phase-increment). In the case a total acquisition much shorter than T_1, the n-th excitation pulse will produce a flip angle θ_n defined by the relation in Eq. 2.21.

$$\theta_n = tan^{-1}\left(\frac{1}{\sqrt{N-n}}\right) \qquad \text{Eq. 2.21}$$

2.7. Hyperpolarized noble gases MRI of rodents' lungs

To date the most widespread atom used for hyperpolarized gases MRI is ^{3}He. The larger ^{3}He gyromagnetic ratio leads to a higher NMR and MRI signal intensity that led to a boost in the human hyperpolarized ^{3}He imaging research in the past two decades (18-20). The main source of ^{3}He comes from the nuclear weapons program (i.e. from tritium decay). The demand of ^{3}He supply exceeding the available quantities, the world is facing a drastic shortage and a price inflation (21). The non-sustainable production of ^{3}He pushed the researchers to extend their effort to hyperpolarized ^{129}Xe pulmonary MRI. Xenon is a naturally occurring element and represents 0.05 ppm of air, and can be extracted by fractional distillation of liquefied air. The ^{129}Xe isotope of interest for MRI represents 26.4 % of xenon gas. The first noble gas imaging actually was the image of a mouse lung preparation using hyperpolarized ^{129}Xe (22). Because ^{129}Xe has a 2.7 times smaller gyromagnetic ratio than ^{3}He (Table 2.1), ^{129}Xe MRI was initially a much difficult task. Recent improvements in the hyperpolarization techniques compensated for the inherent lower signal and allowed ^{129}Xe imaging to reach SNR values comparable to ^{3}He MRI (23-25).

The purpose of this thesis is to demonstrate some new sensor application in *ex vivo* rat lungs and in solution. An overview of the progress in hyperpolarized ^{129}Xe and ^{83}Kr research in rodent pulmonary imaging research related to this work is presented in this section. A description of the *ex vivo* imaging protocol is given at the end of this chapter.

2.7.1. Hyperpolarized ^{129}Xe MRI

2.7.1.1. Ventilation imaging

As discussed in the first part of this chapter, the NMR signal intensity is defined by the energy difference between the spins orientations, and is therefore directly proportional to the gyromagnetic ratio and the field strength. Therefore, identical conditions will lead to smaller ^{129}Xe signal intensity than ^{3}He. The increasing interest in ^{129}Xe spin exchange optical pumping in the last decade led to a significant progress in noble gas SEOP polarizers (23-27).

Static ventilation imaging, usually realized using a FLASH (Flash Low Angle SHot) pulse sequence, allows imaging of the gas distribution within the lungs. An abnormal gas distribution may be the indication of one or more ventilation defects. Quantitative explorations of chronic obstructive pulmonary disease (COPD) and asthma in human have shown correlation between effective ventilation and gold standard clinical spirometry and plethysmography (28).

The variable flip angle (VFA) FLASH sequence has been implemented to reduce the exponential signal decay due to a train of constant flip angles (17). Sequence imaging using VFA FLASH has been shown to create excitation field inhomogeneity artefacts when using human-size excitation coils (29), requiring field correction. This technique is however ideal for rodent lung imaging FOV of a few cm, using small probes (30, 31).

2.7.1.2. Diffusion imaging

The change of location of the gas atoms during the signal acquisition due to diffusion is often a problem causing imaging artefacts. It can however be used as a tool to evaluate the gas diffusion in restricted environment. During a breath hold, the gas is restricted by the pulmonary anatomy. As a consequence, the dimensions of the alveolar microstructure will directly affect the apparent diffusion coefficient (ADC) mapping. The diffusion in lungs has recently been defined as anisotropic, even in the more distal parts as mostly following cylindrical structures (32). The gas diffusion changes caused by destructive diseases such as emphysema seem to induce more variations in the transverse direction, perpendicular to the main diffusion axis (33).

Because of its high signal intensity, and almost insolubility in tissue, most ADC studies were realised using ^{3}He. Free ^{3}He diffusion coefficient in air is

equal to $D_{He} = 0.86cm^2/s$ (34). This value is significantly decreased when restricted by boundaries such as the alveolar walls ($ADC = 0.14 \pm 0.02cm^2/s$ in healthy rat lungs alveolar space, measured at the end of expiration). An increased ^{3}He ADC was observed in emphysematous rats ($ADC = 0.17 \pm 0.02cm^2/s$) (34).

Although the ^{3}He is the gas of choice for ADC MRI investigation, the progress in the ^{129}Xe hyperpolarization overcoming the weaker signal, and the inflation of the ^{3}He price induced a shift of the research effort to ^{129}Xe ADC MRI. ^{129}Xe self-diffusion in air is slower than for ^{3}He, with $D_{Xe} = 0.14cm^2/s$, allowing for some smaller scale diffusion measurements. Boudreau et al. measured a significant increase of the transverse component of the anisotropic gas diffusion from $D_T = 0.0021 \pm 0.0005cm^2/s$ in a control rat to $D_T = 0.005 \pm 0.001cm^2/s$ in the emphysematous rat lungs (35).

^{3}He ADC and ^{129}Xe ADC have been correlated in control and emphysematous rabbits, providing equal results in quantifying the microstructure impairment (36). Finally, the longer diffusion times when using ^{129}Xe would involve lower gradients strengths, which would be easier to implement on clinical MRI scanners.

Note that the ^{83}Kr hyperpolarized technique described further in this section can also be used to evaluate the alveolar microstructure. The work presented in chapter 3 correlates the hyperpolarized ^{83}Kr relaxation behaviour to the alveolar geometry changes caused by emphysema in rat lungs.

2.7.1.3. Dissolved phase imaging

Since its discovery at the end of the 19th century, ^{129}Xe has been a rich topic for the scientific community. ^{129}Xe's solubility has been of particular interest from the late 1940's, when the first anaesthetic effect was observed in mice (37). The solubility of the noble gas has been further studied in aqueous media and in the different compartments of the body.

Noble gas	*Ostwald solubility coefficient*				
	Water (mL/mL)	Plasma (mL/mL)	RBC (mL/mL)	Adipocytes (mL/g)	Human lung homogenate (mL/g)
^{3}He	0.0094 [(a)]	-	-	-	0.01325 [(b)]
^{129}Xe	0.1217 [(a)]	0.1277 [(a)]	0.4312 [(a)]	2.0184 [(a)]	-
^{83}Kr	0.0672 [(a)]	0.059 [(b)]	0.107 [(b)]	0.4622 [(b)]	-

Table 2.4 Ostwald solubility coefficient in water and biological compartments of interest. ^{3}He, ^{129}Xe and ^{83}Kr data were taken from references (38), (39, 40) and (40, 41) respectively. Note that measurements were taken at [(a)] at 20 °C and [(b)] 37 °C.

Table 2.4 reports literature measurements of the Ostwald solubility coefficient for ^{3}He, ^{129}Xe and ^{83}Kr in water and tissues. The Ostwald solubility coefficient is defined by the ratio of the volume of gas absorbed by the volume of the absorbing liquid at a given temperature. ^{129}Xe presents a solubility 13 times larger than ^{3}He, and 2 times larger than ^{83}Kr. In addition, ^{129}Xe's solubility is enhanced by a factor 16 in fat tissue, with an Ostwald coefficient of 2 mL/g (39). The ^{129}Xe higher solubility has been used to explore and image the hyperpolarized ^{129}Xe transfer from the airspace to the bloodstream, whereas ^{3}He remains confined in the alveoli, used as a morphological marker in ventilation and diffusion imaging.

Dissolved phase imaging is possible thanks to the relatively long T_1 of ^{129}Xe with 200 s in the alveolar gas phase in absence of oxygen (11), 15 s in presence of 20 % of oxygen (42), 12 s in the lung parenchyma (43), and 4.0 – 6.4 s in the blood (44), allowing for the transfer of hyperpolarized gas before the signal decay occurs.

^{129}Xe exhibits different chemical shifts when experiencing different chemical environments due to its large electron cloud making it precess at slightly different rates. Furthermore, there are significant differences in the resonance frequency when ^{129}Xe is bound to a variety of molecules, including hemoglobin (45, 46). The different ^{129}Xe chemical shifts observed in rodents and humans spread over 200 ppm, and allow us to differentiate the different compartments, from the gas phase, through the parenchyma, to the bloodstream. Rodents and human static and dynamic studies have shown four

peaks arising from the ^{129}Xe in the lungs. The gas phase peak is used as a 0 ppm reference, and three peaks appear at 191, 199 and 213 ppm, representing ^{129}Xe dissolved in plasma, lung parenchyma and red blood cells respectively (47).

This large chemical shift between the ^{129}Xe present in the alveoli and dissolved in the lung tissue allowed for chemical shift selective imaging of the dissolved phase, thus giving a spatially resolved information of the gas transfer over time (48). The dissolved ^{129}Xe unfortunately represents less than 1-2 % of the total ^{129}Xe present in the lungs after inhalation. This low proportion makes chemical shift imaging of the dissolved phase more complicated, but can be accomplished through signal averaging, selective RF excitation, and radial acquisition (49, 50).

This property has been used to show gas transfer impairment in rodents and human. For example, gas transfer is reduced in interstitial diseases such as idiopathic pulmonary fibrosis (51, 52). Dynamic spectroscopy showed a delayed and decreased ^{129}Xe signal arising from the lungs' vascular system (47). The first exploration in rodents showed a decreased signal in the blood compartment was observed due to a fibrotic thickening of the alveolar membrane (48).

An imaging techniques has been derived from the fact that the signal intensity arising from the dissolved ^{129}Xe is a lot smaller than that of the gas phase. This imaging technique called xenon transfer contrast (XTC), inspired from CEST, compensates the low dissolved ^{129}Xe signal by detecting it indirectly through the gas phase after saturation of the dissolved phase and subsequent gas exchange (53, 54). Two gas phase images have to be acquired, the first one following a saturation of a region without ^{129}Xe signal (-200 ppm), and the second one following the saturation of the dissolved ^{129}Xe (200 ppm). A decrease of signal intensity in the gas phase would indicate a gas transfer from the lung parenchyma to the alveolar space (55, 56).

2.7.1.3. Gas carriers for dissolved ^{129}Xe signal enhancement and contrast

Because the hyperpolarized ^{129}Xe signal arising from the lungs tissue is a factor of 100 times smaller than the gas phase signal after inhalation of the gas, methods to increase the concentration of ^{129}Xe in the bloodstream have been investigated using various biocompatible carrier agents and membrane technologies (50, 57, 58).

In vivo imaging however is still limited by the poor solubility of ^{129}Xe in the blood requiring continuous perfusion of hp ^{129}Xe directly into the bloodstream via a gas exchange module (Membrana MicroModule®, Charlotte, North Carolina, USA). These hollow-fiber membranes used in blood oxygenators have been employed to increase the concentration of dissolved ^{129}Xe both in blood and in solutions (50, 57-60). Membranes have been used as they greatly reduce the degree of foaming that occurs when the relatively insoluble gas is delivered to solution as only small bubbles diffuse across. This method is suitable for *in vivo* animal experimentation but is unlikely to find widespread clinical acceptance due to issues with invasiveness and coagulation within the gas exchange device itself. This extracorporeal circulation composed of a gas exchange module has been used in rats to observe the hp ^{129}Xe transferring back from the bloodstream to the alveoli, by imaging the gas phase (50).

It has been shown to be less technically demanding and less invasive to prepare hp ^{129}Xe into a solution and then infuse the prepared solution into the animal itself (61, 62). Biologically "inert" substances that produce little coagulation can avoid the need for delivery through extracorporeal circulation of blood. Carrier agents with high solubility have been investigated, as it is known that ^{129}Xe has a much higher solubility in lipid and perfluorocarbon based compounds (Ostwald coefficient > 1) (63). Hyperpolarized ^{129}Xe imaging and spectroscopy using gas carrier have been used to investigate the dissolved ^{129}Xe signal by angiography (64), in the brain (65, 66), heart and kidneys (67), but also the gas exchange in the lungs (68).

Table 2.5 lists the particle size, ^{129}Xe solubility and T_1 in gas carrier agents. Perfluorocarbon emulsions (PFCE) have been developed from the late 1980's as blood substitutes taking advantage of their faster exchange with oxygen than

hemoglobin. 1st and 2nd generation PFCE blood substitutes, and perflurooctyl-bromide (PFOB) have been investigated as hp ^{129}Xe carrier agents (57, 63, 69).

	Diameter (μm)	*Ostwald solubility*	T_1 *(s)*	*Chemical shift (ppm)*
Plasma	-	0.13	47.2 ± 5.1	194
RBC	7.0	0.43	2.2 – 7.8 ¶	213
PFCE 1st generation Fluosol	0.20	N/A	N/A	~110
PFCE 2st generation Oxygent	0.16 – 0.19	N/A	N/A	~110
PFOB	0.4 – 5.0 §	1.2	83.4 ± 3.3	106
Liposomes	8	N/A	116.2 ± 6.2	0.6
Intralipid suspension 20 %	N/A	0.62	40.0 ± 3.0	197

Table 2.5 Ostwald solubility and ^{129}Xe T_1 longitudinal relaxation times in different carriers from references (39, 57, 62, 64, 69). ¶ in deoxygenated and oxygenated blood respectively. § eggyold concentration dependent.

When introduced to the PFCE such as Fluosol (Green Cross, Osaka, Japan) or Oxygent (Alliance Pharmaceutical Corp., Wiltshire, UK), hyperpolarized ^{129}Xe displays a broad peak with a chemical shift relative to the gas phase at 110 ppm as compared to the RBC peak at 216 ppm (57).

PFOB emulsions show a narrower peak centered at 106 ppm. The linewidth with PFOB is emulsion-dependent, with larger droplets producing the least exchange and a narrower peak (62). The best peak resolution was obtained with droplets bigger than 5 μm, but such particle size has been associated with various side effects such as thrombocytopenia in some patients after synthetic blood transfusion (70).

Liposomes-filled ^{129}Xe provides a narrow peak located at 0.6 ppm, that could be used as a ^{129}Xe sensor *in vivo*, providing the organ of interest is not in the proximity of the lungs where the ^{129}Xe gas phase signal would overlap with the liposome signal (69).

Although better ^{129}Xe spectral results (narrower dissolved phase peak) are expected with PFOB or liposome agents, most interest should be given to the less harmful gas carriers, such as PFCE with diameter under 0.2 μm.

The peaks associated with the ^{129}Xe in the tissue and in the blood are adjacent, at 191 ppm and 213 ppm in the rodent 198 and 218 ppm in human, and can be difficult to differentiate. The introduction of a carrier agent injected in the rat's

lung pulmonary bloodstream has been explored in Chapter 5, taking advantage of the different chemical shift of ^{129}Xe dissolved in two different perfluorocarbon emulsions (PFCE).

2.7.1.3. ^{129}Xe biosensors

^{129}Xe's solubility and wide chemical shift have also been used for molecular sensing. Some encapsulating molecules have been synthetized to host the ^{129}Xe in the dissolved phase. Spence et al. designed the first ^{129}Xe biosensor in 2001 (71), composed of a cryptophane A tethered to a ligand able to target a protein. The ^{129}Xe dissolved in the solvent will be encapsulated in the cryptophane cage. The signal from the encapsulated ^{129}Xe in a free biosensor appears at 70 ppm, whereas the binding of the ligand to its target induces a chemical shift to 72.5 ppm. Cryptophane E was also used as a ^{129}Xe host for molecular biosensing, with a chemical shift close to 40 ppm (72). More *in vitro* essays have used human proteins targets (73), but the chemical shift created by the molecular biding was always below 7.5 ppm, leading to overlapping ^{129}Xe NMR peaks. Although this ^{129}Xe NMR is feasible *in vitro*, using high resolution NMR probes, *in vivo* detection of such small chemical shift change remains highly difficult. Taratula et al. thought of increasing the local concentration of encapsulated ^{129}Xe by using dendrimers able to congregate several cryptophanes without tethering them (74).

HyperCEST technique based on the XTC was developed (75). This NMR and MRI technique uses the detection of the dissolved phase (medium signal at 193 ppm) after the saturation of the encapsulated ^{129}Xe at 65 ppm or control at -65 ppm. This technique inspired from CEST was also used by Garcia et al (76) to improve the sensitivity of the very low encapsulated signal.

Finally, Klippel et al. used a combination of two ^{129}Xe hosts, cryptophane A (60 ppm) and perfluoroctyl bromide (PFOB, 120 ppm) (77). Two cell cultures were labelled with one of each allowing a selective CEST saturation of each cell population.

Chapter 4 uses an encapsulating cryptophane A, tethered to a paramagnetic gadolinium-DOTA (GdDOTA) group. The transient vicinity of the ^{129}Xe and the GdDOTA induces its fast depolarisation. The relaxivity of the biosensor has been evaluated.

2.7.2. Hyperpolarized ^{83}Kr MRI

Nuclei with nuclear spin $I = 1/2$ have a completely spherical electric charge distribution; the nuclear electric energy will be entirely independent of the orientation of the spin in space, and of its electrical environment. On the other hand, nuclei with nuclear spin $I > 1/2$ such as ^{131}Xe ($I = 3/2$) or ^{83}Kr ($I = 9/2$) have a non-spherical electric charge distribution, called quadrupolar electric charge distribution. The electric quadrupole moment of the nucleus interacts with the electric field gradient (EFG) generated by external distortions of the electronic cloud. This electric quadrupolar interaction in typically an intramolecular process caused by chemical bonding, except for noble gas isotopes that are inherently monoatomic. Figure 2.15 illustrates how adsorption or collision cause a deformation of the electronic cloud, inducing the formation of an Electric Field Gradient (EFG) that will interact will the nuclear quadrupolar moment. The resulting fast quadrupolar driven relaxation will depolarize the ^{83}Kr nuclear spin.

Figure 2.15 ^{83}Kr collisions and surface adsorption causing quadrupolar relaxation.

The ^{83}Kr quadrupolar relaxation was shown to provide a T_1 contrast dependent on the surface-to-volume ratio in the porous medium, but also on the surface hydration.

Porous media made of glass beads have been used to demonstrate the quadrupolar relaxation. A high surface-to-volume ratio increases the

probability of adsorption or collisions of the ^{83}Kr atoms with the surface. Shorter T_1 were observed with high surface-to-volume ratio media (78). Furthermore, hydrophobic surfaces cause shorter T_1 than hydrophilic surfaces due to stronger interaction with the surface during the adsorption (78, 79).

The surface quadrupolar relaxation (SQUARE) previously described in synthetic porous media was also validated in *ex vivo* rat lungs. Excised healthy rat lungs were used as a biological model for porous media with an increasing surface-to-volume ratio from trachea to alveoli.

Stupic et al. used non-localized T_1 spectroscopy with different inhalation schemes to demonstrate the relaxation behaviours in the different lung compartments (14). The inhalation of smaller volumes of hyperpolarized ^{83}Kr followed by thermal gas allows to specifically localize the signal without spatially resolve the spectroscopy (Figure 2.16.a). ^{83}Kr is shown to relax faster in the distal parts of the pulmonary system (Figure 2.16.b).

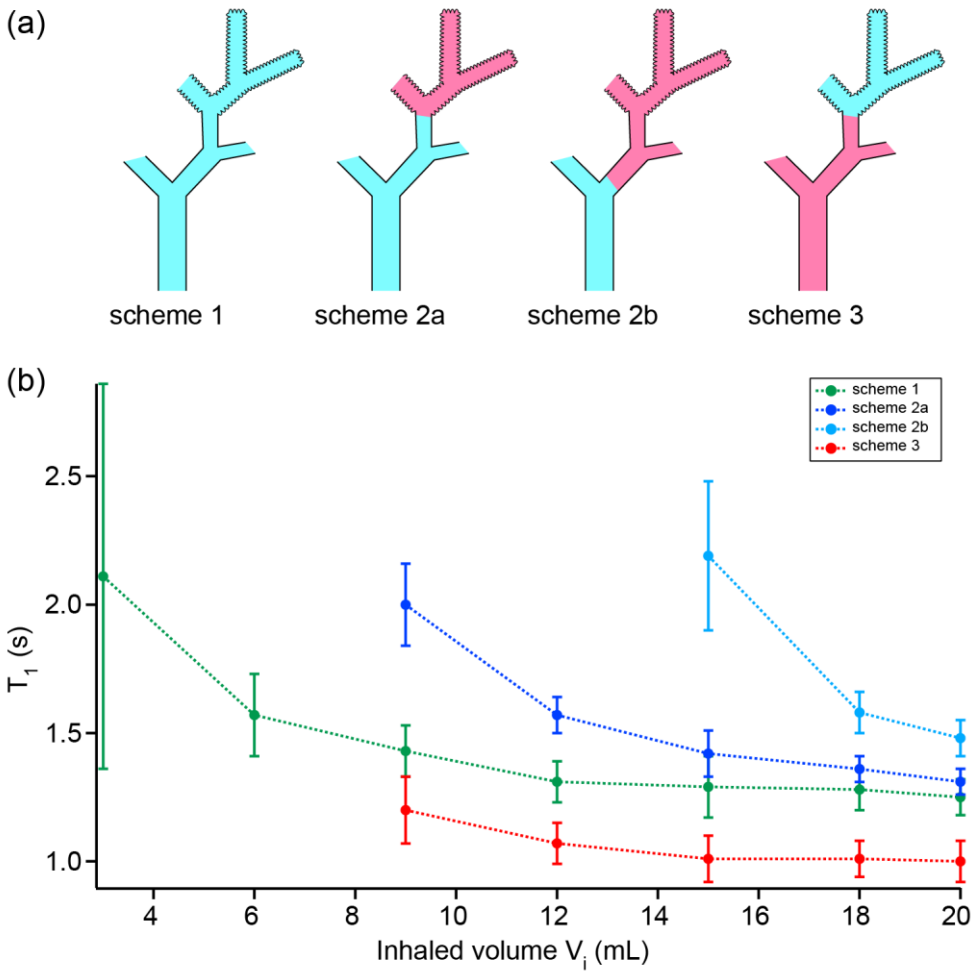

Figure 2.16 (a) Gas distribution for four inhalation schemes in *ex vivo* rat lungs using hyperpolarized ^{83}Kr in blue and thermal gas in pink. Scheme 1: only hp ^{83}Kr inhaled. Scheme 2a: 6 mL of thermal gas followed by hp ^{83}Kr to the total volume. Scheme 2b: 12 mL of thermal gas followed by hp ^{83}Kr to the total volume. Scheme 3: 6 mL of hp ^{83}Kr followed by thermal gas to the total volume. (b) Longitudinal relaxation for the different inhalation schemes and total volumes. Composite figure adapted from reference (14).

These results have been further demonstrated using hp ^{83}Kr MRI. Six et al. acquired an image of the excised lung at different delay post-inhalation (80). Figure 2.17 A to E shows the hyperpolarized ^{83}Kr gas distribution in the lungs at 0.0, 0.5, 1.0 and 1.5 s after inhalation. The signal decay is already visible by simple observation of the ^{83}Kr ventilation images, with brighter airways after long pre-imaging delays. The incremented delay post-inhalation is necessary for the calculation of the spatially resolved ^{83}Kr longitudinal relaxation in the lungs (Figure 2.17 E). A faster T_1 decay is observed in the distal alveolar areas (iv) (0.9±0.1 s) as compared to the trachea (i) (5.3±1.9 s) where the surface-to-volume ratio is small.

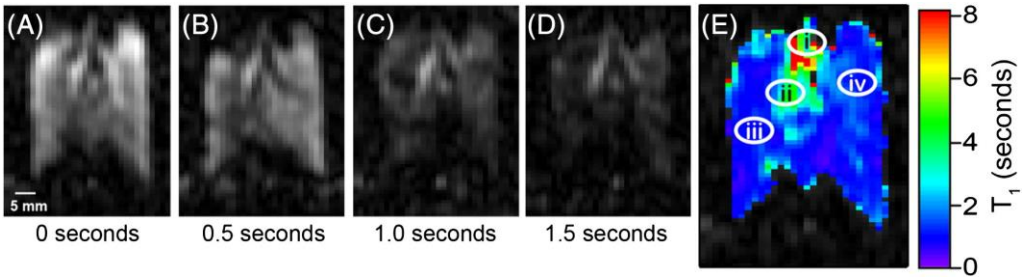

Figure 2.17 SQUARE contrast demonstrated in *ex vivo* Sprague-Dawley rat lungs. (A-D) show the signal decay within the lungs when acquiring ^{83}Kr MRI images after increasing pre-scan delays. (E) Regional T_1 value calculated from the signal decay in (A-D). Figure taken from reference (80).

This ^{83}Kr surface-to-volume ratio sensor has been spatially resolved in healthy rat lungs. This property has been used in an animal model of emphysema, characterized by a destruction of the alveolar structure. The close relationship between T_1 relaxation and surface-to-volume changes caused by emphysema is discussed in Chapter 3.

2.8. *Ex vivo* rat lung protocol

When hyperpolarized noble gases imaging has already been performed *in vivo* in small rodents such as mice, rats or guinea pigs, it is however an undeniable

very complex task. Advances have been made on ventilators allowing the delivery of the hyperpolarized gas to the animal while keeping the animal anaesthetised, but also on fast imaging sequences.

High temporal and spatial resolution for hyperpolarized ^{129}Xe 2D and 3D MRI have been reached by using radial acquisition that allowed a faster sampling of the k-space over the course of several inhalations (81, 82). Cartersian k-spaces are reconstructed by Fourier transform whereas radially collected k-spaces require projection reconstruction techniques. The variable flip angle concept has also been implemented to radial acquisition protocols in order to compensate for the flip-angle-induced hyperpolarization loss (83). Different flip angles have also allowed for selective enhanced resolution in the airways or the peripheral area (82). Acquisition time has also been reduced by using sparse sampling of the k-space (84).

Small animal ventilators have been customised for hyperpolarized gas MRI purpose. They are built from non-magnetic components in order to preserve the gas hyperpolarization. They are usually able to deliver either the normally oxygenated gas mixed with anaesthetic gas, or the hyperpolarized gas mixture in a well-controlled manner (85, 86). Small tubing and valves have to be used to limit the dead space (87). Moreover, small rodents inhale only small volume of gas under 2 mL, and at a rate of 80-160 breaths per minute, requiring a tidal volume delivery high precision and high temporal precision for the MRI acquisition triggering. Whilst most hyperpolarized noble gases compatible ventilators are performing positive pressure forced inhalation (85, 86, 88, 89), another approach has been used to achieve *in vivo* ^{129}Xe gas phase and dissolved phase in mice under passive spontaneous breathing and using low noble gas concentration mixture (90, 91). This technique has the advantage to be less invasive as to not require treating the animal with neuromuscular blocking drug nor excessively deep anaesthesia to control the breathing rate. Indeed, damages have been observed in mice after prolonged mechanical ventilation (92).

Ex vivo lungs experiments have been shown to be technically less demanding and allow for MRI protocols development and study animal models of pulmonary diseases such as asthmatic bronchoconstriction (80, 93, 94). They do not require maintaining the animal under constant anaesthesia nor complex

intubation. The inhaled volume is reproducible over the course of the experiment, and breath holds can be maintained for extended durations. Some more extreme conditions can be applied to the lungs such as the complete absence of oxygen, prolonging the hyperpolarized signal in the lungs. Finally, the *ex vivo* lungs hyperpolarized noble gases MRI reduces the regulatory requirements for animal care and handling. In fact, it allows for the experiments to be realised in buildings that are not compliant to small animal research, and also reduces the approvals needed for the project to be realised in term of animal suffering regulation. A description of the lung excision surgery as used in Chapters 3 and 5 is given in the following section.

The rat was euthanized using an overdose of pentobarbital sodium 200 mg/mL (Euthatal, Merial Animal Health Ltd, Harlow, UK). The permanent cessation of the circulation was checked before pursuing the dissection. From this point, the dissection has to be proceeded as quickly as possible in order to prevent blood clotting in the pulmonary circulation. An incision is done along the mid-ventral line; the aorta is severed under the diaphragm in order to quickly drain the blood out of the heart and pulmonary system. A catheter is positioned in the isolated trachea and clamped after pushing 4 mL of air though it, in order to inflate the lungs to a minimal volume to avoid collapsing of the airways. A catheter is placed in the caudal vena cava and the lungs are perfused with 20 – 30 mL heparin/saline 100 IU/mL to flush the remaining blood from the heart and the lungs. A midline thoracotomy gives access to the pulmonary and cardiac area. The thymus is removed, and the anterior vena cava is ligated. For the purpose of Chapter 5 only, synthetic blood is administrated to the lungs through the caudal vena cava. The lungs are finally loosened from the neck and thorax. A cannula is tied off in the trachea, and the lungs are tested several times for leaks. The lungs are suspended in a ventilation chamber whose dimensions fit the MRI detection coil.

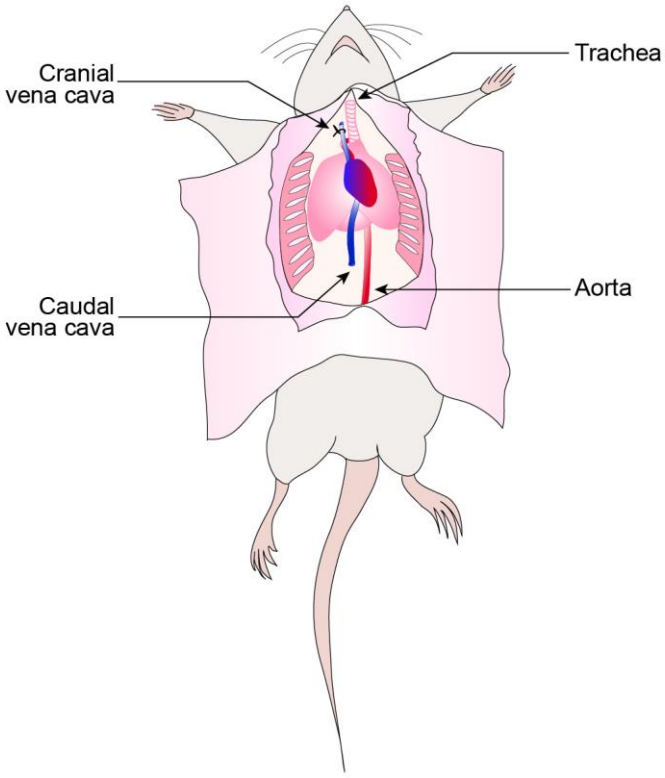

Figure 2.18 Schematics of the principal surgery key locations during the lung extraction for hyperpolarized noble gases MRI. The aorta is first severed, and will serve as blood way-out. The pulmonary circulation is flushed with Heparin/saline through a catheter in the caudal vena cava. The cranial vena cava is sutured to orientate the injected Heparin/saline and synthetic blood directly through the pulmonary circulation. The trachea is catheterised and clamped *in situ* during the surgery.

The ventilation chamber is connected to a ventilation syringe (Figure 2.19.a) placed in the coil within the spectrometer. The hp gas delivery composed of the hyperpolarizer and the recompression unit is attached to the bottom of the ventilation chamber, at the entrance of the trachea. The hp gas is shuttled to the recompression unit, which will deliver the gas at ambient pressure to the lungs. Passive inhalation is realised by pulling the ventilation syringe to the wanted volume (Figure 2.19.b). This will create a negative pressure in the back of the lung, mimicking the action of the diaphragm. This way, the excised lung will passively inhale the recompressed hp gas.

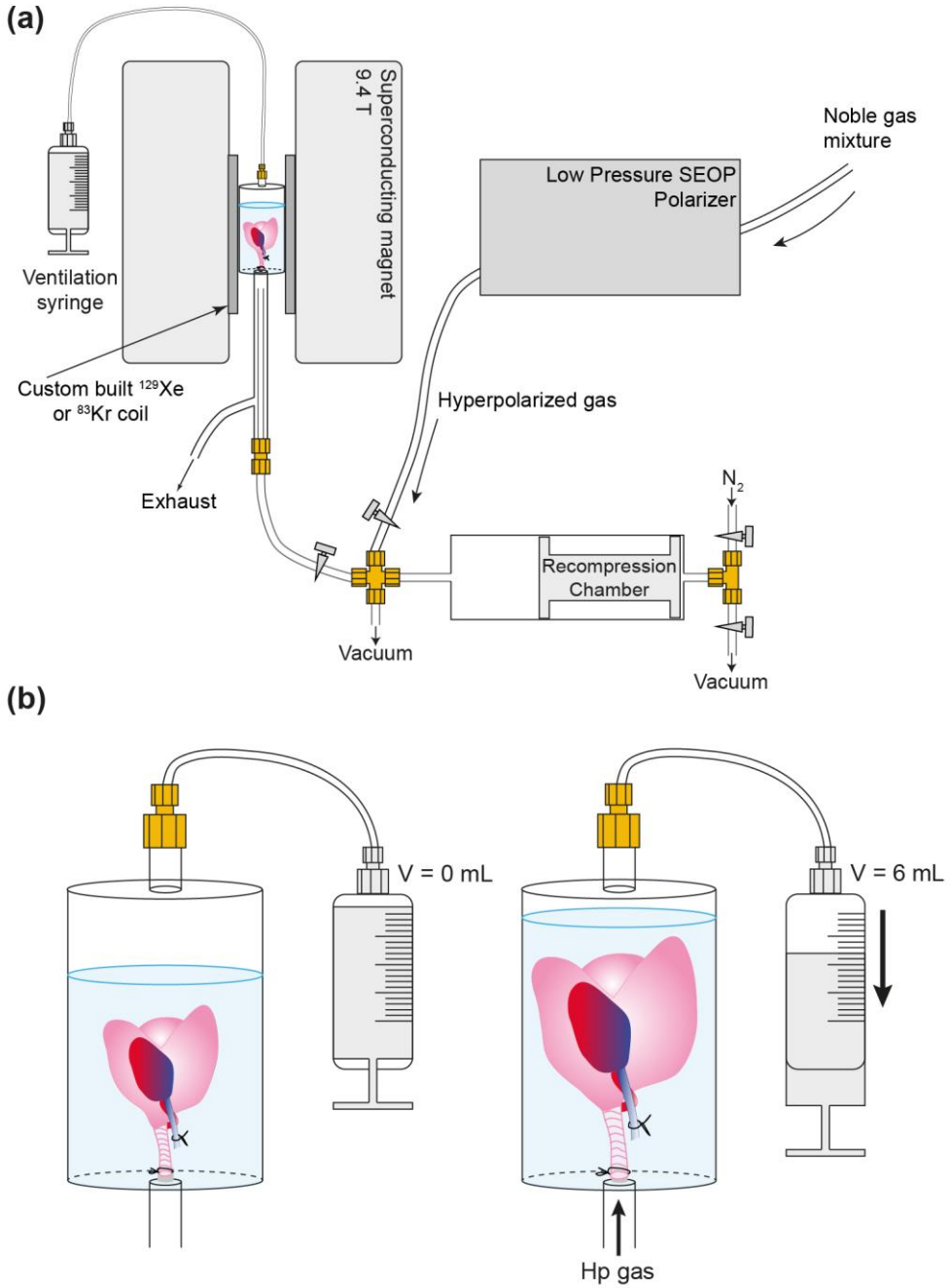

Figure 2.19 Overview of an *ex vivo* lung MRI experiment apparatus. (a) Simplified laboratory setup for an *ex vivo* rat lung experiment. The ^{129}Xe or ^{83}Kr is hyperpolarized at low pressure (< 1 bar) in a custom built polarizer, and delivered to a recompression unit. The recompressed gas will be delivered to a transmission line located at the opening of trachea. (b) *Ex vivo* lungs passive inhalation using a ventilation syringe.

2.7. References

1. Abragam A. The Principles of Nuclear Magnetism. Oxford, UK: Oxford University Press; 1961.
2. Callaghan PT. Principles of Nuclear Magnetic Resonance Microscopy. New York: Oxford University press; 1991.
3. Levitt MH. Spin Dynamics: Basics of Nuclear Magnetic Resonance. West Sussex, UK: John Wiley & Sons, LTD; 2001.
4. Haacke EM, Brown RW, Thompson MR, Venkatesan R. Magnetic Resonance Imaging: Physical Principles and Sequence Design: Wiley; 1999.
5. Harris RK, Becker ED, De Menezes SMC, Goodfellow R, Granger P. NMR nomenclature. Nuclear spin properties and conventions for chemical shifts - (IUPAC recommendations 2001). Pure and Applied Chemistry. 2001;73(11):1795-818.
6. Batz M, Nacher PJ, Tastevin G. Fundamentals of metastability exchange optical pumping in helium. Journal of Physics: Conference Series. 2011;294(1):012002.
7. Comment A, Jannin S, Hyacinthe JN, Mieville P, Sarkar R, Ahuja P, et al. Hyperpolarizing Gases via Dynamic Nuclear Polarization and Sublimation. Physical Review Letters. 2010;105(1):018104.
8. Krjukov EV, O'Neill JD, Owers-Bradley JR. Brute force polarization of Xe-129. Journal of Low Temperature Physics. 2005;140(5-6):397-408.
9. Six JS, Hughes-Riley T, Stupic KF, Pavlovskaya GE, Meersmann T. Pathway to cryogen free production of hyperpolarized krypton-83 and xenon-129. Plos One (in press). 2012.
10. Gentile TR, Jones GL, Thompson AK, Rizi RR, Roberts DA, Dimitrov IE, et al. Demonstration of a compact compressor for application of metastability-exchange optical pumping of He-3 to human lung imaging. Magn Reson Med. 2000;43(2):290-4.
11. Hughes-Riley T, Six JS, Lilburn DML, Stupic KF, Dorkes AC, Shaw DE, et al. Cryogenics free production of hyperpolarized 129Xe and 83Kr for biomedical MRI applications. J Magn Reson. 2013;237:23-33.
12. Six JS. New MRI contrast agents through spin exchange optical pumping of noble gases with a nuclear electric quadrupole moment: University of Nottingham; 2014.

13. Gao JH, Lemen L, Xiong JH, Patyal B, Fox PT. Magnetization and diffusion effects in NMR imaging of hyperpolarized substances. Magn Reson Med. 1997;37(1):153-8.
14. Stupic KF, Elkins ND, Pavlovskaya GE, Repine JE, Meersmann T. Effects of pulmonary inhalation on hyperpolarized krypton-83 magnetic resonance T-1 relaxation. Phys Med Biol. 2011;56(13):3731-48.
15. Hahn EL. Spin echoes. Phys Rev. 1950;80(4):580-94.
16. Haase A, Frahm J, Matthaei D, Hanicke W, Merboldt KD. FLASH imaging. Rapid NMR imaging using low flip-angle pulses. Journal of Magnetic Resonance (1969). 1986;67(2):258-66.
17. Zhao L, Mulkern R, Tseng CH, Williamson D, Patz S, Kraft R, et al. Gradient-echo imaging considerations for hyperpolarized Xe-129 MR. Journal of Magnetic Resonance Series B. 1996;113(2):179-83.
18. van Beek EJR, Wild JM, Kauczor HU, Schreiber W, Mugler JP, de Lange EE. Functional MRI of the lung using hyperpolarized 3-helium gas. Journal of Magnetic Resonance Imaging. 2004;20(4):540-54.
19. Mayo JR, Hayden ME. Hyperpolarized Helium 3 Diffusion Imaging of the Lung1. Radiology. 2002;222(1):8-11.
20. Mugler Iii JP, Wang C, Miller GW, Cates Jr GD, Mata JF, Brookeman JR, et al. Helium-3 Diffusion MR Imaging of the Human Lung Over Multiple Time Scales. Acad Radiol. 2008;15(6):693-701.
21. Shea DA, Morgan D. The Helium-3 Shortage: Supply, Demand, and Options for Congress. Congressional Research Service; 7-5700; R41419; wwwcrsgov 2010.
22. Albert MS, Cates GD, Driehuys B, Happer W, Saam B, Springer CS, et al. Biological Magnetic-Resonance-Imaging Using Laser Polarized Xe-129. Nature. 1994;370(6486):199-201.
23. Driehuys B, Cates GD, Miron E, Sauer K, Walter DK, Happer W. High-volume production of laser-polarized Xe-129. Applied Physics Letters. 1996;69(12):1668-70.
24. Hersman FW, Ruset IC, Ketel S, Muradian I, Covrig SD, Distelbrink J, et al. Large production system for hyperpolarized Xe-129 for human lung imaging studies. Acad Radiol. 2008;15(6):683-92.

25. Nikolaou P, Coffey AM, Walkup LL, Gust BM, Whiting N, Newton H, et al. Near-unity nuclear polarization with an open-source 129Xe hyperpolarizer for NMR and MRI. Proceedings of the National Academy of Sciences. 2013;110(35):14150-5.

26. Zook AL, Adhyaru BB, Bowers CR. High capacity production of > 65% spin polarized xenon-129 for NMR spectroscopy and imaging. J Magn Reson. 2002;159(2):175-82.

27. Driehuys B, Pollaro J, Cofer GP. In vivo MRI using real-time production of hyperpolarized Xe-129. Magn Reson Med. 2008;60(1):14-20.

28. Kirby M, Svenningsen S, Owrangi A, Wheatley A, Farag A, Ouriadov AV, et al. Hyperpolarized 3He and 129Xe MR Imaging in Healthy Volunteers and Patients with Chronic Obstructive Pulmonary Disease. Radiology. 2012.

29. Deppe MH, Teh K, Parra-Robles J, Lee KJ, Wild JM. Slice profile effects in 2D slice-selective MRI of hyperpolarized nuclei. J Magn Reson. 2010;202(2):180-9.

30. Santyr GE, Lam WW, Parra-Robles JM, Taves TM, Ouriadov AV. Hyperpolarized noble gas magnetic resonance imaging of the animal lung: Approaches and applications. Journal of Applied Physics. 2009;105(10).

31. Santyr GE, Lam WW, Ouriadov A. Rapid and efficient mapping of regional ventilation in the rat lung using hyperpolarized 3He with Flip angle variation for offset of RF and relaxation (FAVOR). Magn Reson Med. 2008;59(6):1304-10.

32. Fichele S, Paley MNJ, Woodhouse N, Griffiths PD, van Beek EJR, Wild JM. Finite-difference simulations of He-3 diffusion in 3D alveolar ducts: Comparison with the "cylinder model". Magn Reson Med. 2004;52(4):917-20.

33. Xu X, Boudreau M, Ouriadov A, Santyr GE. Mapping of 3He apparent diffusion coefficient anisotropy at sub-millisecond diffusion times in an elastase-instilled rat model of emphysema. Magn Reson Med. 2012;67(4):1146-53.

34. Chen XJ, Hedlund LW, Moller HE, Chawla MS, Maronpot RR, Johnson GA. Detection of emphysema in rat lungs by using magnetic resonance measurements of He-3 diffusion. Proceedings of the National Academy of Sciences of the United States of America. 2000;97(21):11478-81.

35. Boudreau M, Xu X, Santyr GE. Measurement of 129Xe gas apparent diffusion coefficient anisotropy in an elastase-instilled rat model of emphysema. Magn Reson Med. 2013;69(1):211-20.
36. Mata JF, Altes TA, Cai J, Ruppert K, Mitzner W, Hagspiel KD, et al. Evaluation of emphysema severity and progression in a rabbit model: comparison of hyperpolarized He-3 and Xe-129 diffusion MRI with lung morphometry. J Appl Physiol. 2007;102(3):1273-80.
37. Lawrence J, Loomis W, Tobias C, Turpin F. Preliminary observations on the narcotic effect of xenon with a review of values for solubilities of gases in water and oils. The Journal of physiology. 1946;105(3):197.
38. Hiza M. Solubility data series, volume 1: Helium and neon—gas solubilities: H. Lawrence Clever (ed.), Pergamon Press, 1979, xxi+ 393 pages, $100.00, ISBN 0-08-022351-6. Elsevier; 1980.
39. Chen RYZ, Fan FC, Kim S, Jan KM, Usami S, Chien S. Tissue-Blood partition-coefficient for Xenon - Temperature and hematocrit dependence. J Appl Physiol. 1980;49(2):178-83.
40. Clever H. Solubility data series, volume 2: Krypton, Xenon and Radon-gas solubilities. International Union of Pure and Applied Chemistry. Pergamon Press, Oxford/UK (ua); 1979.
41. Strang R. Measurement of Ostwald solubility coefficient of Krypton in blood and ocular tissue. Phys Med Biol. 1975;20(6):1025-8.
42. Jameson CJ, Jameson AK, Hwang JK. Nuclear-Spin Relaxation by Intermolecular Magnetic Dipole Coupling in the Gas-Phase - Xe-129 in Oxygen. Journal of Chemical Physics. 1988;89(7):4074-81.
43. Martin CC, Williams RF, Gao JH, Nickerson LDH, Xiong JH, Fox PT. The pharmacokinetics of hyperpolarized xenon: Implications for cerebral MRI. JMRI-J Magn Reson Imaging. 1997;7(5):848-54.
44. Wolber J, Cherubini A, Dzik-Jurasz ASK, Leach MO, Bifone A. Spin-lattice relaxation of laser-polarized xenon in human blood. Proceedings of the National Academy of Sciences of the United States of America. 1999;96(7):3664-9.
45. Albert MS, Schepkin VD, Budinger TF. Measurement of Xe-129 T1 in Blood to Explore the Feasibility of Hyperpolarized Xe-129 Mri. Journal of Computer Assisted Tomography. 1995;19(6):975-8.

46. Ratcliffe CI. Xenon NMR. Annual Reports on NMR Spectroscopy. 1998;36:123-221.

47. Sakai K, Bilek AM, Oteiza E, Walsworth RL, Balamore D, Jolesz FA, et al. Temporal dynamics of hyperpolarized Xe-129 resonances in living rats. Journal of Magnetic Resonance Series B. 1996;111(3):300-4.

48. Driehuys B, Cofer GP, Pollaro J, Mackel JB, Hedlund LW, Johnson GA. Imaging alveolar-capillary gas transfer using hyperpolarized Xe-129 MRI. Proceedings of the National Academy of Sciences of the United States of America. 2006;103(48):18278-83.

49. Kaushik SS, Freeman MS, Cleveland ZI, Davies J, Stiles J, Virgincar RS, et al. Probing the regional distribution of pulmonary gas exchange through single-breath gas- and dissolved-phase Xe-129 MR imaging. J Appl Physiol. 2013;115(6):850-60.

50. Cleveland ZI, Moller HE, Hedlund LW, Nouls JC, Freeman MS, Qi Y, et al. In Vivo MR Imaging of Pulmonary Perfusion and Gas Exchange in Rats via Continuous Extracorporeal Infusion of Hyperpolarized Xe-129. PLoS One. 2012;7(2).

51. Agusti AGN, Roca J, Gea J, Wagner PD, Xaubet A, Rodriguezroisin R. Mechanisms of gas-exchange impairment in idiopathic pulmonary fibrosis. Am Rev Respir Dis. 1991;143(2):219-25.

52. Egger C, Cannet C, Gerard C, Jarman E, Jarai G, Feige A, et al. Administration of Bleomycin via the Oropharyngeal Aspiration Route Leads to Sustained Lung Fibrosis in Mice and Rats as Quantified by UTE-MRI and Histology. PLoS One. 2013;8(5):13.

53. Ruppert K, Brookeman JR, Hagspiel KD, Mugler JP. Probing lung physiology with xenon polarization transfer contrast (XTC). Magn Reson Med. 2000;44(3):349-57.

54. Ruppert K, Mata JF, Wang HTJ, Tobias WA, Cates GD, Brookeman JR, et al. XTC MRI: Sensitivity improvement through parameter optimization. Magn Reson Med. 2007;57(6):1099-109.

55. Patz S, Muradian I, Hrovat MI, Ruset IC, Topulos G, Covrig SD, et al. Human pulmonary imaging and spectroscopy with hyperpolarized Xe-129 at 0.2T. Acad Radiol. 2008;15(6):713-27.

56. Dregely I, Mugler JP, Ruset IC, Altes TA, Mata JF, Miller GW, et al. Hyperpolarized Xenon-129 Gas-Exchange Imaging of Lung Microstructure: First Case Studies in Subjects With Obstructive Lung Disease. Journal of Magnetic Resonance Imaging. 2011;33(5):1052-62.

57. Bifone A, Song YQ, Seydoux R, Taylor RE, Goodson BM, Pietrass T, et al. NMR of laser-polarized xenon in human blood. Proceedings of the National Academy of Sciences of the United States of America. 1996;93(23):12932-6.

58. Amor N, Hamilton K, Kuppers M, Steinseifer U, Appelt S, Blumich B, et al. NMR and MRI of Blood-Dissolved Hyperpolarized Xe-129 in Different Hollow-Fiber Membranes. ChemPhysChem. 2011;12(16):2941-7.

59. Amor N, Zanker PP, Blumler P, Meise FM, Schreiber LM, Scholz A, et al. Magnetic resonance imaging of dissolved hyperpolarized Xe-129 using a membrane-based continuous flow system. J Magn Reson. 2009;201(1):93-9.

60. Baumer D, Brunner E, Blumler P, Zanker PP, Spiess HW. NMR spectroscopy of laser-polarized Xe-129 under continuous flow: A method to study aqueous solutions of biomolecules. Angewandte Chemie-International Edition. 2006;45(43):7282-4.

61. Wolber J, Rowland IJ, Leach MO, Bifone A. Intravascular delivery of hyperpolarized (129)xenon for in vivo MRI. Applied Magnetic Resonance. 1998;15(3-4):343-52.

62. Wolber J, Rowland IJ, Leach MO, Bifone A. Perfluorocarbon emulsions as intravenous delivery media for hyperpolarized xenon. Magn Reson Med. 1999;41(3):442-9.

63. Albert MS, Balamore D, Kacher DF, Venkatesh AK, Jolesz FA. Hyperpolarized Xe-129 T-1 in oxygenated and deoxygenated blood. NMR Biomed. 2000;13(7):407-14.

64. Moller HE, Chawla MS, Chen XJ, Driehuys B, Hedlund LW, Wheeler CT, et al. Magnetic resonance angiography with hyperpolarized Xe-129 dissolved in a lipid emulsion. Magn Reson Med. 1999;41(5):1058-64.

65. Duhamel G, Choquet P, Grillon E, Lamalle L, Leviel JL, Ziegler A, et al. Xenon-129 MR imaging and spectroscopy of rat brain using arterial delivery of hyperpolarized xenon in a lipid emulsion. Magn Reson Med. 2001;46(2):208-12.

66. Choquet P, Hyacinthe JN, Duhamel G, Grillon E, Leviel JL, Constantinesco A, et al. Method to determine in vivo the relaxation time T-1 of hyperpolarized xenon in rat brain. Magn Reson Med. 2003;49(6):1014-8.
67. Swanson SD, Rosen MS, Coulter KP, Welsh RC, Chupp TE. Distribution and dynamics of laser-polarized Xe-129 magnetization in vivo. Magn Reson Med. 1999;42(6):1137-45.
68. Driehuys B, Möller HE, Cleveland ZI, Pollaro J, Hedlund LW. Pulmonary Perfusion and Xenon Gas Exchange in Rats: MR Imaging with Intravenous Injection of Hyperpolarized 129Xe. Radiology. 2009;252(2):386-93.
69. Venkatesh AK, Zhao L, Balamore D, Jolesz FA, Albert MS. Evaluation of carrier agents for hyperpolarized xenon MRI. NMR Biomed. 2000;13(4):245-52.
70. Goodin TH, Kaufman RJ. Method of pretreating an animal with a corticosteroid prior to infusion of a perfluorochemical emulsion. Google Patents; 1997.
71. Spence MM, Rubin SM, Dimitrov IE, Ruiz EJ, Wemmer DE, Pines A, et al. Functionalized xenon as a biosensor. Proceedings of the National Academy of Sciences of the United States of America. 2001;98(19):10654-7.
72. Huber G, Brotin T, Dubois L, Desvaux H, Dutasta JP, Berthault P. Water soluble cryptophanes showing unprecedented affinity for xenon: Candidates as NMR-based biosensors. J Am Chem Soc. 2006;128(18):6239-46.
73. Chambers JM, Hill PA, Aaron JA, Han ZH, Christianson DW, Kuzma NN, et al. Cryptophane Xenon-129 Nuclear Magnetic Resonance Biosensors Targeting Human Carbonic Anhydrase. J Am Chem Soc. 2009;131(2):563-9.
74. Taratula O, Dmochowski IJ. Functionalized Xe-129 contrast agents for magnetic resonance imaging. Current Opinion in Chemical Biology. 2010;14(1):97-104.
75. Schroder L, Lowery TJ, Hilty C, Wemmer DE, Pines A. Molecular imaging using a targeted magnetic resonance hyperpolarized biosensor. Science. 2006;314(5798):446-9.

76. Garcia S, Chavez L, Lowery TJ, Han SI, Wemmer DE, Pines A. Sensitivity enhancement by exchange mediated magnetization transfer of the xenon biosensor signal. J Magn Reson. 2007;184(1):72-7.

77. Klippel S, Freund C, Schroder L. Multichannel MRI Labeling of Mammalian Cells by Switchable Nanocarriers for Hyperpolarized Xenon. Nano Lett. 2014;14(10):5721-6.

78. Stupic KF, Cleveland ZI, Pavlovskaya GE, Meersmann T. Quadrupolar Relaxation of Hyperpolarized Krypton-83 as a Probe for Surfaces. Solid State Nuclear Magnetic Resonance. 2006;29:79-84.

79. Cleveland ZI, Stupic KF, Pavlovskaya GE, Repine JE, Wooten JB, Meersmann T. Hyperpolarized ^{83}Kr and ^{129}Xe NMR Relaxation Measurements of Hydrated Surfaces: Implications for Materials Science and Pulmonary Diagnostics. J Am Chem Soc. 2007;129(6):1784-92.

80. Six JS, Hughes-Riley T, Lilburn DML, Dorkes AC, Stupic KF, Shaw DE, et al. Pulmonary MRI contrast using Surface Quadrupolar Relaxation (SQUARE) of hyperpolarized Kr-83. Magnetic Resonance Imaging. 2014;32(1):48-53.

81. Viallon M, Cofer GP, Suddarth SA, Moller HE, Chen XJ, Chawla MS, et al. Functional MR microscopy of the lung using hyperpolarized He-3. Magn Reson Med. 1999;41(4):787-92.

82. Chen BT, Brau ACS, Johnson GA. Measurement of regional lung function in rats using hyperpolarized (3)helium dynamic MRI. Magn Reson Med. 2003;49(1):78-88.

83. Thomas AC, Potts EN, Chen BT, Slipetz DM, Foster WM, Driehuys B. A robust protocol for regional evaluation of methacholine challenge in mouse models of allergic asthma using hyperpolarized 3He MRI. NMR Biomed. 2009;22(5):502-15.

84. Ajraoui S, Lee KJ, Deppe MH, Parnell SR, Parra-Robles J, Wild JM. Compressed Sensing in Hyperpolarized (3)He Lung MRI. Magn Reson Med. 2010;63(4):1059-69.

85. Nouls J, Fanarjian M, Hedlund L, Driehuys B. A Constant-Volume Ventilator and Gas Recapture System for Hyperpolarized Gas MRI of Mouse and Rat Lungs. Concepts Magn Reson Part B. 2011;39B(2):78-88.

86. Hedlund LW, Cofer GP, Owen SJ, Johnson GA. MR-compatible ventilator for small animals: computer-controlled ventilation for proton and noble gas imaging. Magnetic Resonance Imaging. 2000;18(6):753-9.

87. de Alejo RP, Ruiz-Cabello J, Villa P, Rodriguez I, Perez-Sanchez JM, Peces-Barba G, et al. A fully MRI-compatible animal ventilator for special-gas mixing applications. Concepts Magn Reson Part B. 2005;26B(1):93-103.

88. Chen BT, Johnson GA. Dynamic lung morphology of methacholine-induced heterogeneous bronchoconstriction. Magn Reson Med. 2004;52(5):1080-6.

89. Hedlund LW, Moller HE, Chen XJ, Chawla MS, Cofer GP, Johnson GA. Mixing oxygen with hyperpolarized He-3 for small-animal lung studies. NMR Biomed. 2000;13(4):202-6.

90. Wakayama T, Kitamoto M, Ueyama T, Imai H, Narazaki M, Kimura A, et al. Hyperpolarized Xe-129 MRI of the mouse lung at a low xenon concentration using a continuous flow-type hyperpolarizing system. Journal of Magnetic Resonance Imaging. 2008;27(4):777-84.

91. Hori Y, Kimura A, Wakayama T, Kitamoto M, Imai F, Imai H, et al. 3D Hyperpolarized Xe-129 MRI of Mouse Lung at Low Xenon Concentration using a Continuous Flow-type Hyperpolarizing System: Feasibility for Quantitative Measurement of Regional Ventilation. Magnetic Resonance in Medical Sciences. 2009;8(2):73-9.

92. Wolthuis EK, Vlaar APJ, Choi G, Roelofs J, Juffermans NP, Schultz MJ. Mechanical ventilation using non-injurious ventilation settings causes lung injury in the absence of pre-existing lung injury in healthy mice. Crit Care. 2009;13(1).

93. Lilburn DML, Hughes-Riley T, Six JS, Stupic KF, Shaw DE, Pavlovskaya GE, et al. Validating Excised Rodent Lungs for Functional Hyperpolarized Xenon-129 MRI. PLoS One. 2013;8(8).

94. Lilburn DM, Tatler AL, Six JS, Lesbats C, Habgood A, Porte J, et al. Investigating lung responses with functional hyperpolarized xenon‐129 MRI in an ex vivo rat model of asthma. Magn Reson Med. 2015.

CHAPTER 3

HYPERPOLARIZED ^{83}KR MAGNETIC RESONANCE IMAGING OF ALVEOLAR DEGRADATION IN A RAT MODEL OF EMPHYSEMA

The results presented in this chapter appear in parts in the journal publication: David M.L. Lilburn, Clémentine Lesbats, Joseph S. Six, Eric Dubuis, Liang Yew-Booth, Dominick E. Shaw, Maria G. Belvisi, Mark A. Birrell, Galina E. Pavlovskaya and Thomas Meersmann, "Hyperpolarized ^{83}Kr magnetic resonance imaging of alveolar degradation in a rat model of emphysema", J. R. Soc. Interface (2015) 12:20150192 (1).

Experiments presented in this chapter were performed collectively at the Sir Peter Mansfield Imaging Centre at the University of Nottingham and at the Respiratory Pharmacology group at Imperial College London. Original concept and protocol design were developed by Prof. Meersmann and Dr. Lilburn. The animal model preparation, handling and care, and histological analysis were performed by Dr. Birrell, Mr. Dubuis and Ms. Yew-Booth at Imperial College London. The lungs harvesting was performed by Dr. Lilburn and Dr. Birrell. The hyperpolarized ^{83}Kr imaging was carried out by Dr. Lilburn, Dr. Six, and Ms. Lesbats at the Sir Peter Mansfield Imaging Centre. Image processing and T_1 map reconstruction were performed by Dr. Pavlovskaya. The first data analyseis were performed by the authors included in the published article cited above. Further image and statistical analysis by Ms. Lesbats is presented at the end of this chapter.

3.1. Introduction

^{83}Kr quadrupolar relaxation behaviour has been shown to be of interest in biomedical research. Hyperpolarized ^{83}Kr had originally been investigated using packed beads surface models, showing a relationship between the relaxation rate, R_1, and the surface to volume (S/V) ratio, the surface chemistry and temperature (2). An augmentation in S/V ratio induced a reduction of T_1, and a reduction of the signal intensity. The ^{83}Kr surface quadrupolar relaxation (SQUARE) has subsequently been demonstrated in *ex vivo* lungs where the T_1 relaxation was observed to be shorter in the alveoli as compared to the main airways, confirming the S/V ratio dependency of the ^{83}Kr relaxation behaviour (3).

In this chapter, the surface to volume ratio-sensitive SQUARE contrast in the lungs is investigated in an animal model of a component of chronic obstructive pulmonary disease (COPD), namely emphysema. COPD is a complex and not yet fully understood pulmonary disease composed of an airways obstruction (chronic bronchiolitis) and a parenchymal destruction (emphysema). Emphysema is characterised by a progressive alveolar destruction over time caused by inflammation and hyperinflation (4). New screening techniques are of particular interest considering COPD is the fourth leading cause of death worldwide and is estimated to become the third in 2030 (5). The main cause of such parenchymal tissue damage is chronic inflammation. The principal known risk factor is cigarette smoking, but pollution, occupational exposure, intrinsic factors, gender and aging seem to be involved as well (6,7). Smoking has been the cause of death of 73 % of COPD patients in the high-income countries, and 40 % of low-income countries (5). An intrinsic genetic risk factor is also involved in emphysema causing an α-1 antitrypsin enzyme imbalance in 1-3 % of the patients with COPD, inducing an antiprotease deficiency, and an increased extracellular matrix proteolysis from the neutrophil elastase (6,8,9). The destruction of the parenchyma leads to a loss in lung elasticity and of gas exchange surface area, inducing a decrease in airflow (ventilation defects), and in the ability to transfer the oxygen from the air to the blood (diffusing capacity) respectively (10). Patients will suffer of increasing dyspnoea and congestion over time, and various other symptoms ranging from sleep

disturbance to anxiety or even alienation, decreasing the overall quality of life (11). The only treatment at the moment is avoidance or reduction of the exposure to the risk factors such as cigarette smoke accompanied by bronchodilators treating the associated asthmatic symptoms, and in some cases bullectomy to excise the extremely damaged lung areas, or in cases of extreme severity lung transplant (12).

Lung function tests are currently used to diagnose pulmonary impairments such as emphysema (4). However, they do not allow a diagnosis before an advanced stage of the disease, when most symptoms are already established, and more importantly they give a global measurement of the lung function. High resolution computed tomography (HRCT) also show some bigger alveolar holes, called bullae within the distal lung (13). Because of this late diagnosis and high mortality, the importance of investigating emphysema and finding new biomarkers is paramount for an early diagnosis and the preservation of the lung function at an early stage of the disease. Numerous clinical and preclinical studies used computed tomography (CT), providing an excellent resolution of the scattered alveolar 'holes', but also a lowered diaphragm caused by the whole lung enlargement (14). Magnetic resonance imaging (MRI) has also been of interest for clinical imaging research of emphysema. When ^{1}H imaging is already a difficult method for healthy lung imaging, the decreased tissue density due to the emphysematous injuries makes ^{1}H MRI even more challenging (15). On the other hand, hyperpolarized ^{3}He and ^{129}Xe MRI can provide ventilation imaging, showing ventilation defects in the lungs (16). The most interesting hyperpolarized ^{3}He MRI exploration is the gas diffusion in the lungs, directly correlated to histological analysis of the alveolar dimensions (17). The ^{3}He apparent diffusion coefficient (ADC) has been shown to increase from 0.225 cm^2/s to 0.452 cm^2/s in human emphysematous lungs (18,19). In the same way, hyperpolarized ^{129}Xe MRI allows ventilation imaging and ADC analysis (20,21).

Several animal models have been used to reproduce the emphysematous pulmonary damages. The traditional rodent model created in the 1960's (22) uses an elastase proteinase, such as the human neutrophilic elastase papain or the porcine pancreatic elastase PPE, that destroys the extracellular matrix protein elastin, inducing the emphysematous lesions. These injuries cause a

destruction of the alveolar macrostructure, therefore decreasing the surface area in the parenchyma (23,24). These structural changes go along with a secretory cell metaplasia, comparable to chronic bronchitis (25). Animal models of emphysema have been assessed using histology (26), micro-CT (27), lung function tests (28), exercise capacity evaluation (29), but also hyperpolarized noble ^{3}He and ^{129}Xe MRI (30,31).

This chapter aims to confirm the ^{83}Kr SQUARE contrast using the established PPE animal model of emphysema. This *ex vivo* rat lung hyperpolarized ^{83}Kr MRI study demonstrates that the ^{83}Kr T_1 contrast can be used as a biomarker for emphysema. A global and regional analysis shows a ^{83}Kr R_1 correlation with the S/V ratio changes in the alveolar parenchyma.

3.2. Material and methods

3.2.1 Motivation

The ^{83}Kr nuclear spin $I = 9/2$ leads to a non-uniform nuclear charge distribution. The non-spherical symmetry of the nuclear charges distribution creates a nuclear electric quadrupole moment. Any interaction of the noble gas with a surface, such as collisions or adsorption, will induce an electronic cloud distortion and create an electric field gradient (EFG). Quadrupolar relaxation ensues from interactions between the EFG and the nuclear electric quadrupolar moment, resulting in shorter T_1 relaxation in the presence of surfaces as compared to the bulk gas phase (more detail in Section 2.7.2.).

The low gyromagnetic ratio and the surface-induced T_1 relaxation create low intensity NMR hp ^{83}Kr signal and thus make structural gas imaging challenging but not impossible at lower resolution (32). However, the ^{83}Kr surface quadrupolar relaxation (SQUARE) MRI contrast is influenced by the S/V ratio but also by surface chemistry, temperature, and surface adsorption of molecules (32-35). In this study, hyperpolarized ^{83}Kr is used to introduce a new source of contrast within the lungs, dependent on the S/V ratio. The confirmation of ^{83}Kr contrast caused by emphysematous damages represents a first stage in the ^{83}Kr lung imaging development. This contrast can also be extended to other lung diseases caused by lung surfactant chemistry changes that can be due for instance to prematurity (36).

3.2.2. Elastase-induced pulmonary emphysema in rats: induction and preparation for *ex vivo* MRI

12 male Sprague-Dawley rats, ranging between 260 and 300 g (Harlan UK Ltd., Bicester, IK) were used for imaging and histology. 2 in 5 control rats and 2 in 7 elastase-treated rats were used solely for histology purposes. The other rats were used for both *ex vivo* imaging and histology.

Animals were anaesthetised using Isoflurane 4% with medical grade O_2 for 3 to 4 min. Emphysema was induced by intratracheal instillation of one dose of 120 U/kg Porcine Pancreatic Elastase, PPE (Merk Chemicals Ltd, Nottingham, UK) at 1 mL/kg. Control animals were similarly treated with 1 mL/kg sterile saline (Fresenus Kabi Ltd., Manor Park, UK). 28 days after intratracheal instillation, animals were weighted (see Table 3.1) and euthanized with an intraperitoneal overdose of sodium pentobarbital 200 mg/Kg (Merial Animal Health, Harlow, UK). Death was confirmed by assessing: the cessation of the circulation, and the non-response to a painful stimulus by pinching the legs with surgical forceps. Severing the aorta and caudal vena cava as rapidly as possible will cause the exsanguination, and avoid quick coagulation in the heart and pulmonary circulation, therefore minimising the presence of paramagnetic iron that would depolarize the hyperpolarized ^{83}Kr. A catheter is placed in the caudal vena cava and tightened with a suture. This catheter is used to flush the pulmonary circulation with 20 mL heparin 100 IU/mL (Wockhardt UK Ltd., Wrexham, UK) in 0.9 % saline solution (Baxter Healthcare Ltd., Thetford, UK). Then, 20 mL Dublecco's phosphate buffer solution (D-PBS, Sigma Aldrich Ltd, Gillingham, UK) were flown through it to remove residual blood. The lungs and heart are excised *en masse*. A polytetrafluorethylene (PTFE) adaptor tube is inserted in the trachea 5 – 10 mm above the carina and tightened with a suture. A syringe is inserted in the adaptor, the lungs are inhaled to 10 mL and exhaled a few times to ensure they are not leaking. Finally, the lungs are suspended in 5 % (weight/volume) glucose solution (Baxter Healthcare Ltd., Thetford, UK) in a custom-built acrylic 30 mm diameter ventilation chamber, pointing downwards for hyperpolarized gas experiments (37).

	Identifier	*Rat Weight (g)*	*Whole lung MAA (10^4 μm²)*	Lung usage: MRI: *hp ^{83}Kr MRI including histology* Histology: *satellite group*	*Inhaled volume in MRI, V_i (mL)*
Control	CL.1	492	-	MRI	7.0 ± 0.3
	CL.2	555	2.5 ± 0.1	MRI	6.8 ± 0.1
	CL.3	499	3.7 ± 0.6	MRI	6.8 ± 0.1
	CL.4	400	1.9± 0.1	Histology	N/A
	CL.5	412	2.5± 0.4	Histology	N/A
Elastase (PPE) treated	EL.1	390	6.3 ± 1.1	MRI	5.9 ± 0.7
	EL.2	508	6.8 ±1.1	MRI	6.1 ± 0.6
	EL.3	416	5.1 ± 1.0	MRI	6.9 ± 0.3
	EL.4	440	4.5 ± 0.6	MRI	7.3 ± 0.4
	EL.5	513	3.6 ± 1.0	MRI	6.1 ± 0.2
	EL.6	382	4.8 ± 1.4	Histology	N/A
	EL.7	436	10.8 ± 6.2	Histology	N/A

Table 3.1 Demographic data from satellite animals (histology) and those used for hp ^{83}Kr imaging. Summary of rat weights, whole lung mean alveolar area ± standard deviation of the mean, inhaled volumes (V_i) ± standard deviation corresponding to inflation (syringe) volume V_s = 8 mL. No values for V_i were determined in the histology groups. Values omitted were not measured.

3.2.3. Alveolar cross-section measurements

Emphysema is described as a degradation of the alveolar sacs structure, leading to enlarged airways and resulting in a decreased gas exchange area. Elastase-induced emphysema is a well-known animal model in rats, reproducing the human histological feature of emphysema: the airspace enlargement (25,38). The porcine pancreatic elastase (PPE) is a protease degrading elastic fibres, giving rise to a rapid enlargement of the airspace.

Experimental emphysema can be assessed by measuring the average air space area. This technique was first described by Belloni et al. (39) and used previously (40). The lungs were inflated to forced vital capacity (25 cm H_2O) with 5 % formalin – saline solution (Sigma-Aldrich Ltd, Gillingham, UK). The trachea was tied off and the lungs were then placed in formalin. After at least 24 h in formalin, an experienced histologist processed the lungs. The lungs

were wax-embedded, sectioned using a microtome, and stained with hematoxylin and eosin (H&E) stain. Five slices per lobe were selected in each lung for analysis using an Olympus BX40 microscope and a Zeiss image-processing software (Imaging Associates, Bicester, UK), excluding slices from the fields containing vasculature and large airways. The mean air space area was averaged for each lobe, and subsequently averaged for each lung, giving a mean alveolar area (MAA). Results are displayed in Table 3.1 and illustrated in Figure 3.1.

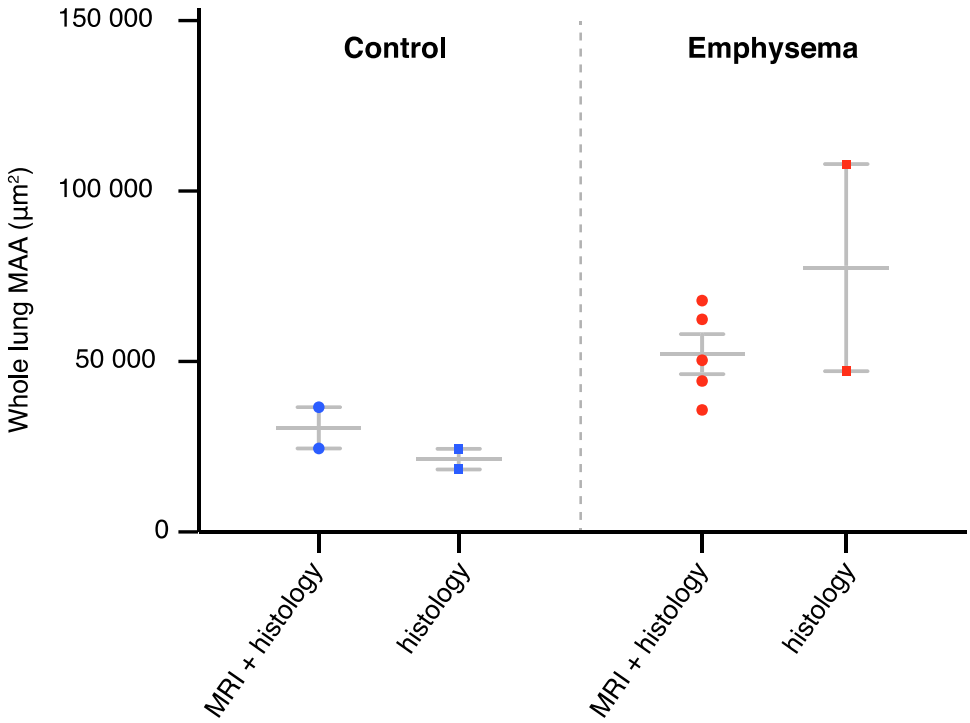

Figure 3.1 Line and whiskers diagram of the histological data. The individual data from control lungs (in blue) and emphysematous lungs (in red) are displayed for each group, overlaid with the mean, and standard error of the mean, SEM (in grey). No significant difference is observed between the lungs used for MRI and subsequent mean alveolar area (MAA) determination ('MRI + histology' group) and the histology-only group within the control group and the emphysema group.

As described in Table 3.1 some lungs were used for MRI and histological analysis, whereas some other rats were only utilised for histology. In order to compare the whole lung MAA results for each sub-group of the control and emphysema groups, results were displayed in Figure 3.1. Despite the small sample size, the Mann-Whitney U-test shows a non-significant difference between the MRI + histology and histology groups within the control (*p*-value

= 0.33) and emphysema groups (p-value = 0.57). This non-significant different between the sub-groups allows us to cluster them into a control group and an emphysema group for statistical analysis (see results Section 3.3.3.).

Furthermore, although the *ex vivo* lung functional ^{129}Xe imaging methodology has already been demonstrated to be of use for physiological studies, the non-significant difference between the sub-groups in this work validates the *ex vivo* experimental protocol for the study of histological features of lungs using hp ^{83}Kr. No significant alveolar damage has been induced by *ex vivo* mechanical ventilation and MR imaging.

3.2.4. Hyperpolarization, gas recompression, transfer and hp gas inhalation

Hp ^{83}Kr was produced in batch mode spin exchange optical pumping (SEOP). The gas mixture used was composed of 15 % enriched ^{83}Kr (99.925 % ^{83}Kr, CHEMGAS, Boulogne, France) and 85 % N_2 (99.999 % purity, Air Liquide, Coleshill, UK). The SEOP was realised at 55 – 65 kPa with a build-up time was 12 min. A recompression unit described in (41) was used to bring back up the hp gas to ambient pressure, an inhalable pressure. The spin polarization reached P = 16 – 17 % after extraction and recompression of the gas, and an apparent polarization of P_{app} = 2.5 % (42). The method produced 12 – 16 mL of hp gas mixture every 12 min. This volume was enough to fill the transmission lines and allow the inhalation of 6 – 7 mL of hp gas by the *ex vivo* lungs.

3.2.5. MRI protocol

The ^{83}Kr imaging has been performed using a 9.4 T Bruker Avance III microimaging system (Bruker Biospin GmbH, Rheinstetten, Germany) and a 30 mm inner diameter Bruker double saddle coil tuned to the ^{83}Kr resonance frequency (15.40 MHz).

Non-slice selective coronal imaging of the lungs was performed by using a variable flip angle (VFA) FLASH sequence (43). The 32 x 32 matrix was acquired with a rectangular RF pulse of constant width of 0.3 ms and variable power, and the parameters TE = 1.8 ms, and TR = 12.6 ms, leading to a field of view FOV = 50.9 x 40.7 mm^2. The total acquisition time was 0.405 s.

T_1-weighted imaging was realised by acquiring five images as in previous works published by Six and coworkers (3). Each image acquisition was started after a post-inhalation delay τ_d = 0.2 s, 0.7 s, 1.2 s, 1.7 s, 2.2 s. Note that some maps were calculated from a series of 0.5 s, 1.0 s, 1.5 s, 2.0 s. The manual inhalation of the hp gas was achieved by pulling a ventilation syringe, leading to a reduction of the pressure in the artificial pleural cavity created by the ventilation chamber (as in Figure 2.19).

3.2.6. Image reconstruction and analysis

The 32 x 32 data were reconstructed in Prospa (Magritek, Wellington, New Zealand). Sine-bell squared apodization, zero filling to 64 points, and Fourier transform are applied to the raw data. 64 x 64 magnitude data are then exported to Igor Pro (Wavemetric, Lake Oswego, OR, USA) for T_1 analysis. T_1 data sets were created for each series of images by combining the images acquired at the individual time delays τ_d into a three dimensional dataset with increasing τ_d (see Figure 3.3). As described by Six et al. (3), spatially resolved T_1 was calculated from the linear regression of the natural logarithm of the signal intensity as a function of delay time. All T_1 values out of the range $0 \leq T_1 \leq 6s$ were rejected as physically not meaningful. Furthermore, a ROI was defined by selecting the lung contour on the image acquired with the shortest τ_d. Any T_1 values out of this ROI were also rejected. The resulting T_1 maps were used to plot T_1 histograms for each lung. T_1 data were binned into 200 intervals with 0.03 s increments. The Igor Pro Multipeak 1.4 function was used for an automated peak picking. A bi-modal Gaussian distribution was fitted on each histogram. The parameters of the distribution provided numerical biomarkers that were used for analysis. Moreover, a T_1 bimodal distribution was assumed due to the existence of two pulmonary compartments of different dimension scales, the large airways and the small alveolar areas, where ^{83}Kr would experience different relaxation behaviours.

The results of the histogram analysis returned the most probable (expected value, EV) relaxation time and the full width at half maximum (FWHM) for each of the two Gaussian components (see Figure 3.2). The fast component was described by its highest probability (the highest number of voxels) $T_1^{EV(f)}$

and its full width at half maximum $FWHM\left(T_1^{(f)}\right)$. The slow component was described by $T_1^{EV(sl)}$ and $FWHM\left(T_1^{(sl)}\right)$. All the bimodal fitting parameters were stored in Table 3.2.

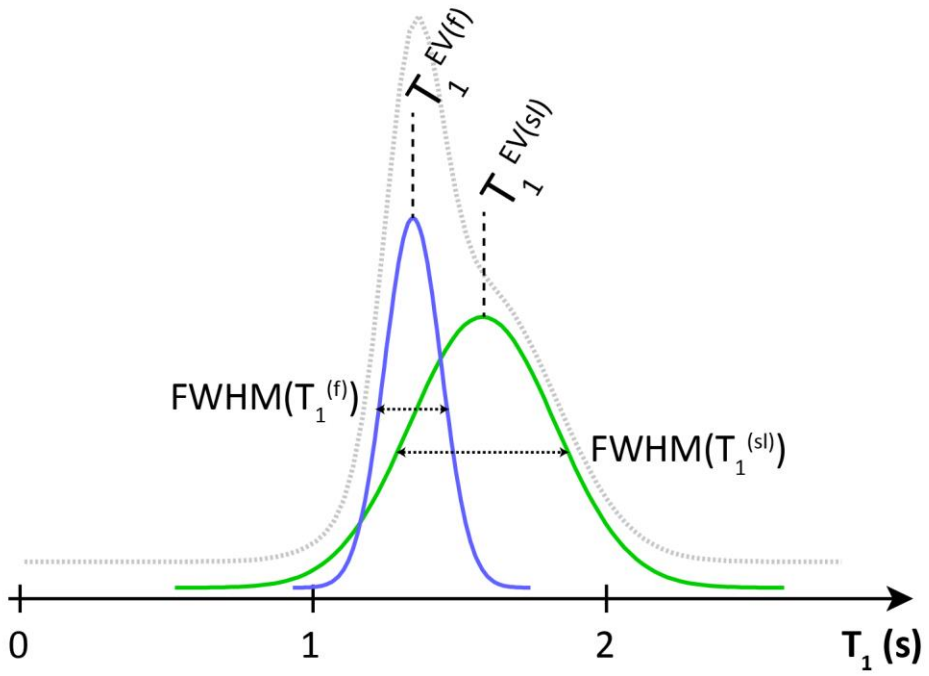

Figure 3.2 Description of the bi-modal fitting parameters. The T_1 distribution within the lungs (dashed grey curve) is decomposed into two Gaussian in blue and green. Two modes are therefore identifiable $T_1^{EV(f)}$ and $T_1^{EV(sl)}$, with their respective full width at half maximum $FWHM\left(T_1^{(f)}\right)$ and $FWHM\left(T_1^{(f)}\right)$.

	Rat identifier	$T_1^{EV(f)}$ *(s)* *mean*	$FWHM(T_1^{(f)})$ *(s)* *mean*	$T_1^{EV(sl)}$ *(s)* *mean*	$FWHM(T_1^{(sl)})$ *(s)* *mean*
Control lung	CL.1	0.9958	0.19619	1.2353	0.53927
	CL.2	1.0130	0.091234	1.2189	0.30050
	CL.3	1.0099	0.14987	1.3556	0.48057
	Average ± standard deviation	**1.00620** ± 0.009	**0.14576** ± 0.053	**1.2699** ± 0.075	**0.44011** ± 0.124
Combined histogram of control lungs (Figure 3.6 – blue histogram)		1.0112	0.13073	1.2494	0.38797
Elastase (PPE) treated lung	EL.1	1.2559	0.12770	1.4787	0.32787
	EL.2	1.2311	0.30498	1.7067	0.52674
	EL.3	1.3697	0.28202	2.0474	0.63887
	EL.4	1.1576	0.21975	1.5708	0.71203
	Average ± standard deviation	**1.25358** ± 0.088	**0.23361** ± 0.079	**1.7009** ± 0.249	**0.55138** ± 0.167
Combined histogram of elastase (PPE) treated lungs (Figure 3.6 – red histogram)		1.2734	0.28201	1.7288	0.54928
	EL.5	0.94994	0.1333	1.2257	0.4500

Table 3.2 Characteristic T_1 times from bimodal fitting of the histograms of all lungs used in this work.

3.3. Results and discussion

3.3.1. SQUARE contrast in the control and emphysema groups

An example of hp ^{83}Kr MRI of a control lung and a PPE-treated lung is shown in Figure 3.3. The series of coronal images at different τ_d show the signal decay caused by the T_1 relaxation, with a faster decay in the alveolar space than in the bronchial tree. The bronchial signal is persisting longer than the alveolar signal, and is still visible at 2.2 s. The PPE-treated lungs show more signal heterogeneity than the control lungs. However, heterogeneous ventilation was not the scope of the study and was even observed in some control lungs (Figure 3.4.c) and can be caused by various physiopathological reasons. The hp ^{83}Kr T_1 relaxation time has been measured to be 90 – 150 s in a 10 mm diameter 5 cm

long glass cylinder, at 289 K, 100 kPa and 9.4 T (2). Shorter T_1 values recorded in the lungs are predominantly caused by the ^{83}Kr atoms interaction with the lung surface. The alveolar space has a significantly higher S/V ratio than the bronchi. As reported in Six et al. paper (3), a faster T_1 relaxation was expected in the alveolar space due to the SQUARE effect. Regions with a low S/V ratio such as the bronchi will have a longer ^{83}Kr T_1 relaxation, and remain "bright" longer than regions with a higher S/V ratio and shorter T_1 such as the alveolar regions. This prolonged T_1 relaxation time in the airways is illustrated in the T_1 map in Figure 3.3. The PPE-treated lung SQUARE T_1 map (Figure 3.3.d) reveals higher T_1 values than the control lung (Figure 3.3.b), displaying an elevated level of green colour.

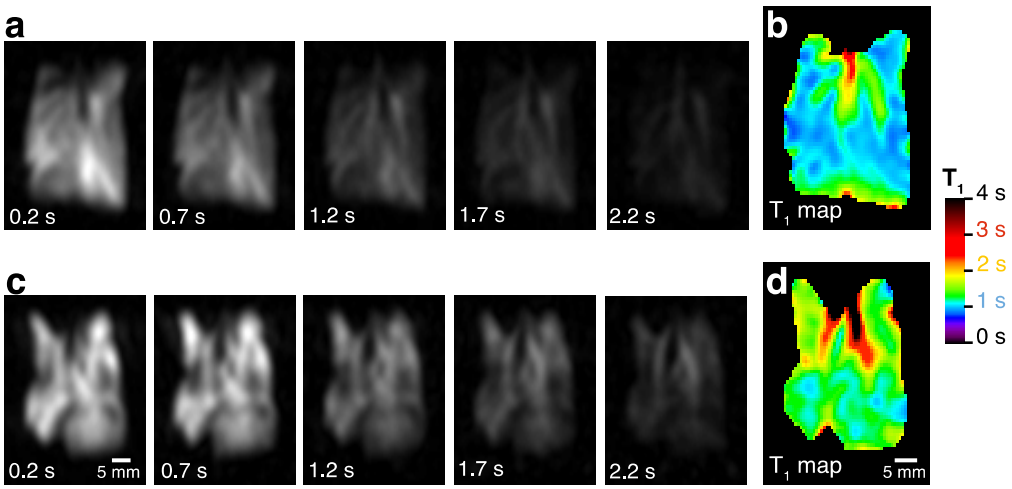

Figure 3.3 Series of hp ^{83}Kr images with resultant T_1 maps in control and PPE-treated lungs. VFA FLASH MRI with no slice selection in control lung CL.2 using a variable relaxation delay τ_d values, ranging from 0.2 s to 2.2 s between the hp gas inhalation and acquisition of the image. Each image in (a) and (c) was acquired using a new delivery of hp ^{83}Kr. (b) The resultant SQUARE T_1 map displays longer T_1 values for the major airways and shorter values for the alveolar region. (c) VFA FLASH MRI in the PPE-treated lung EL.1. (d) The resultant SQUARE T_1 map displays prolonged relaxation times in the alveolar area compared with the control T_1 map (b).

Three control lungs T_1 maps are displayed in Figure 3.4. The data were plotted into histograms for comparative analysis. The pixel count for each T_1, between 0.0 and at 4.0 s at intervals of 0.03 s, were analysed using a bi-modal Gaussian distribution function. The Gaussian distribution of the fast relaxing component is represented in blue under the histograms, whereas the slow relaxing component is represented in green. The sum of the two Gaussians results in the histogram contour, in black, suggesting the bimodal fitting is an accurate method to characterise the SQUARE behaviour in lungs. Figure 3.5 represents the T_1 maps and their histograms for four PPE-treated lungs. The SQUARE T_1 maps depict visually some marked differences between the control lungs and the PPE-treated lungs, revealing more green and yellow colour than the control maps in Figure 3.4. The characteristic parameters from the bimodal fitting are listed in Table 3.2.

Control lungs show some average values of 1.0 s and 1.3 s for $T_1^{EV(f)}$ and $T_1^{EV(sl)}$ respectively, with the corresponding full width at half maximum 0.1 s and 0.4 s. On the other hand, PPE-treated lungs seem to have longer T_1^{EV} and broader Gaussian distributions with 1.3 s and 1.7 s for $T_1^{EV(f)}$ and $T_1^{EV(sl)}$ respectively and 0.3 s and 0.6 s as full width at half maximum.

3.3.2. T_1 maps and histograms comparison

Some ventilation defects are observed in two out of the three control lungs (Figure 3.4.a and c). This ventilation heterogeneity might be due to the 3-hours transport of the *ex vivo* lungs between the Respiratory Pharmacology Laboratory at Imperial College London and the hp MRI facility in Nottingham.

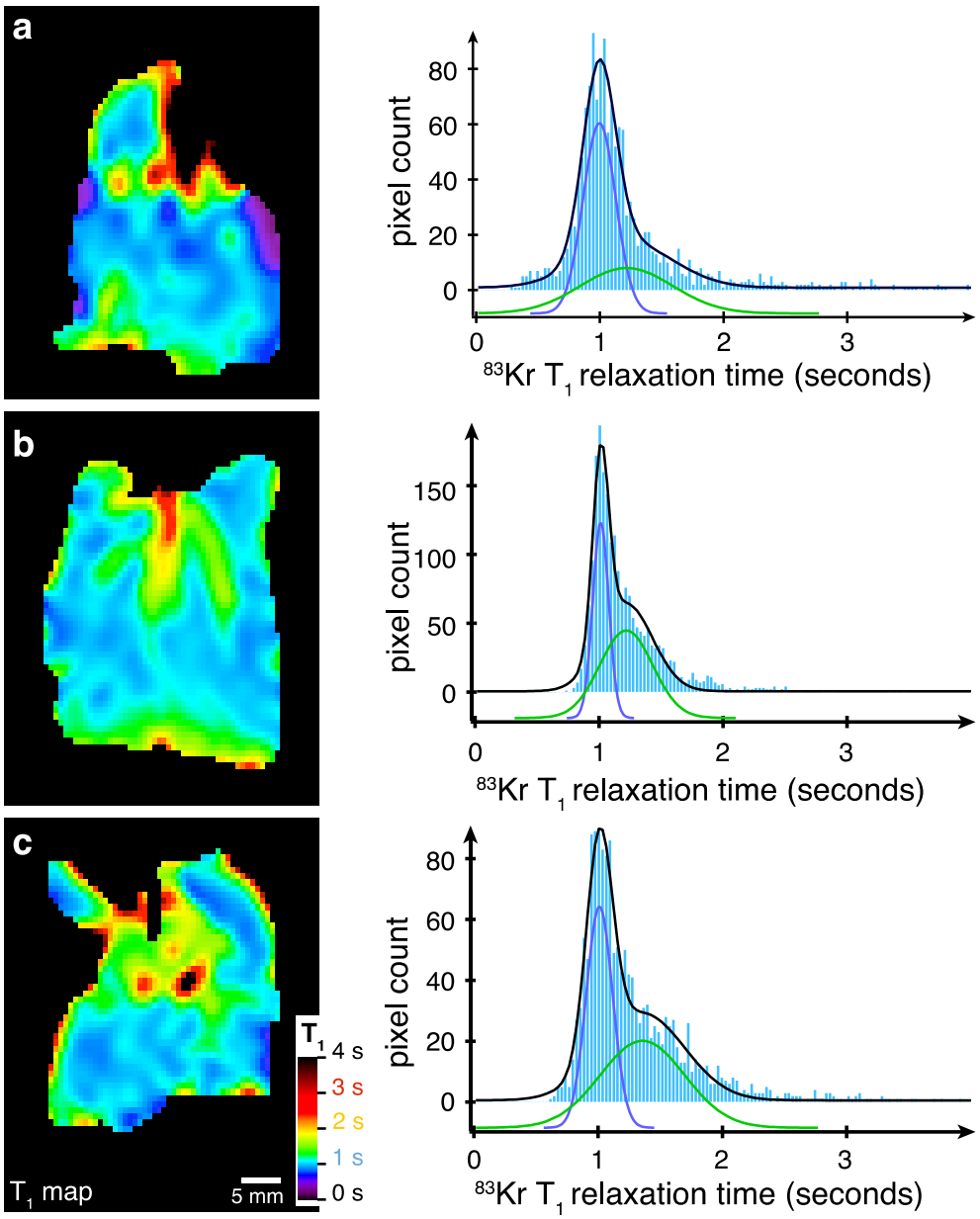

Figure 3.4 ^{83}Kr MRI T_1 maps (SQUARE contrast) of three control lungs and their corresponding histograms: (a) Lung CL.1, (b) CL.2 and (c) CL.3. Blue colour in the alveolar regions indicates short T_1 values around 1 s. The histograms represent the pixel count from the T_1 maps of T_1 values within 0.03 s intervals. A bimodal fitting leads to a narrow Gaussian distribution of fast relaxing pixels (blue sold line) centred around $T_1^{EV(f)} \approx 1s$, and a broader distribution (green solid line) centred around $T_1^{EV(sl)} \approx 1.3s$.

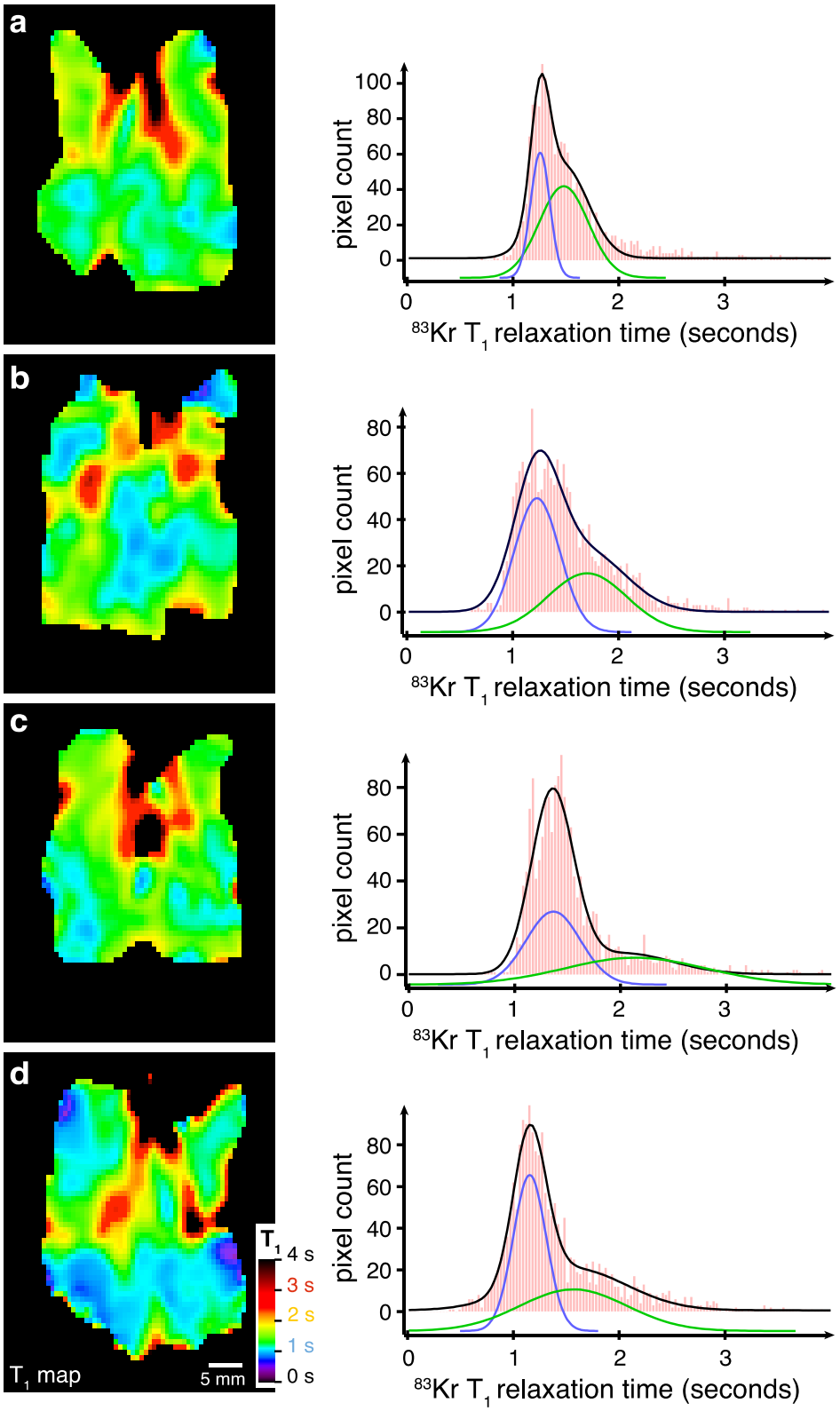

Figure 3.5 ^{83}Kr MRI T_1 maps (SQUARE contrast) of four PPE-treated lungs and their corresponding histograms as described in Figure 3.4: (a) EL.1, (b) EL.2, (c) EL.3 and (d) EL.4. The characteristic T_1 values are shifted to larger values than the control lungs (Figure 3.4) with $T_1^{EV(f)} \approx 1.3s$ (blue solid line) and $T_1^{EV(sl)} \approx 1.7s$ (green solid line).

Combined histograms for the three control lungs and four PPE-treated lungs are represented in Figure 3.6. This summary of the two groups represents the sum of all pixels for each T_1. The T_1^{EV} and FWHM parameters resulting from these combined histograms are listed in Table 3.2 along with the individual histograms values.

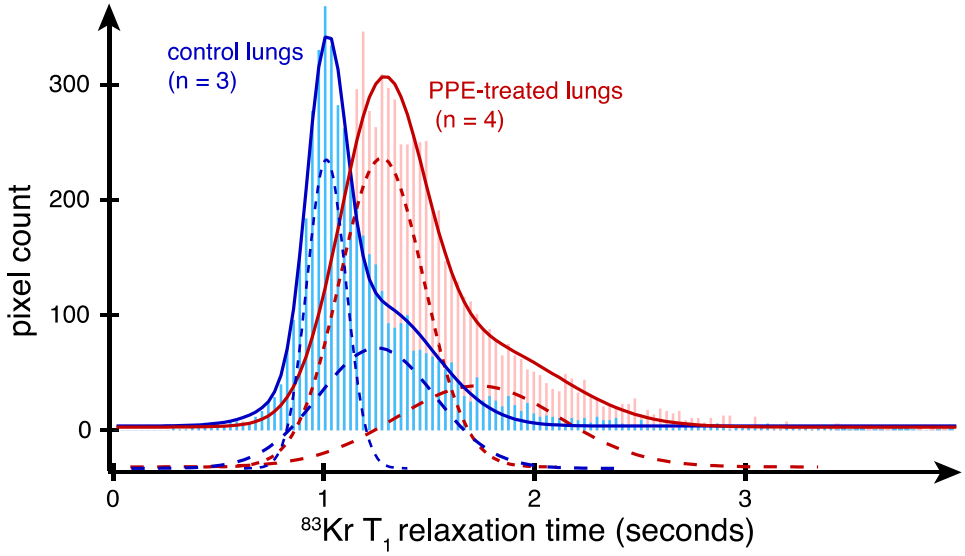

Figure 3.6 Combined histograms of all added T_1 in the control and PPE-treated groups. Data were obtained from three control lungs (blue) in Figure 3.4 and PPE-treated (red) in Figure 3.5. The characteristic T_1 data from bimodal fitting (solid lines) are decomposed into slow and fast components (dashed lines).

A fifth lung (EL.5) from the PPE-treated group was excluded from the statistical analysis because the MAA increased developed asymmetrically in the left lobe only, possibly due to a very localised elastase deposition. The histological data for this lung in Table 3.1 (MAA = 3.6 x 104 μm^2) prefigure a T_1 map similar to those in control lungs. All lobar MAA were in line with the control group except for the left lung that exhibits very high MAA values (Figure 3.7.c). The T_1 map for this lung EL.5 and the corresponding histogram (Figure 3.7.a and b) are very similar to the control lungs'. Although the left lobe has very high MAA values, the T_1 map and histogram are not showing the expected locally high T_1 values in this lobe. This might be due to the extreme damage of the lung on this side, preventing any ventilation of these areas during the imaging. The unventilated areas should appear as 'dark' regions on

the hp ^{83}Kr SQUARE map, but they also could be masked by other ventilated areas, contributing to the non-slice selective image.

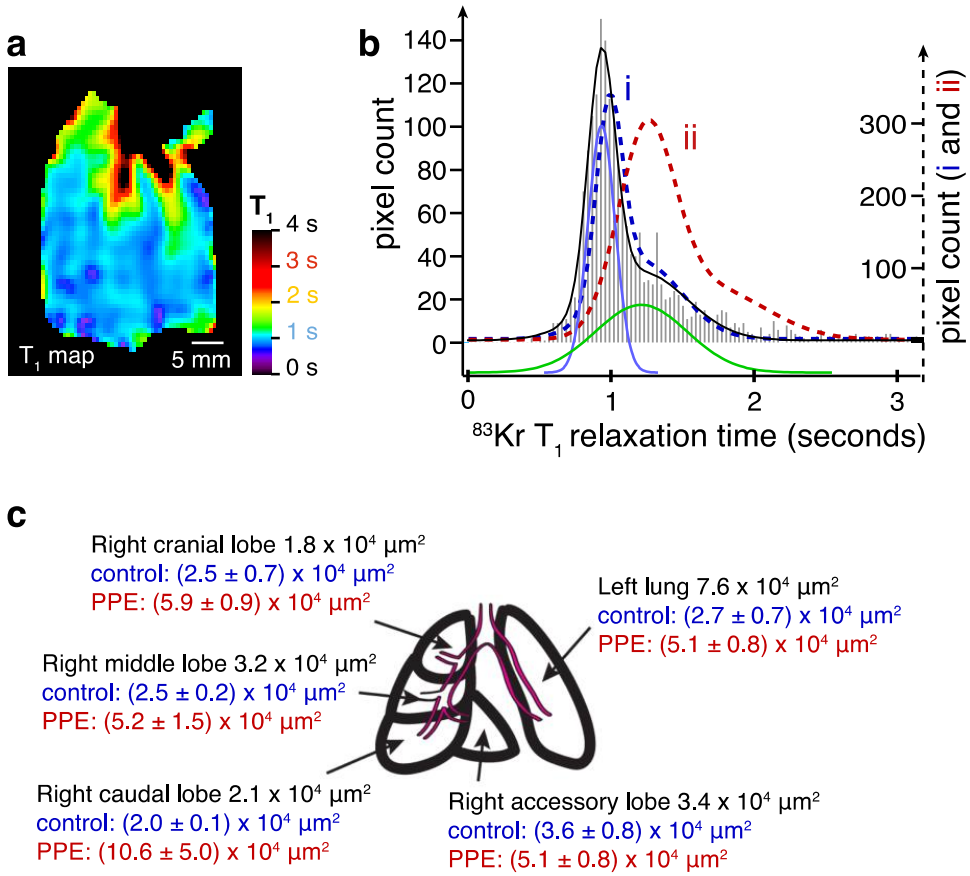

Figure 3.7 (a) ^{83}Kr MRI T_1 map (SQUARE contrast) of the PPE-treated lung EL.5 with (b) its corresponding histogram and (c) comparative lobar mean alveolar area values. The grey histogram has a bimodal function fitted in black solid line and decomposed in two Gaussians in blue (fast mode) and green (slow mode). For comparison, the outline of the histograms represented in Figure 3.6 are displayed in blue (control) and red (PPE-treated) dashed line. The T_1 maps (SQUARE contrast) and the histogram seem to demonstrate that the lung EL.5 has similar ^{83}Kr T_1 values to the control lungs.

The boxplots in Figure 3.8 illustrate a graphical overview of all of the bimodal parameters for the control lungs (in blue) and the PPE-treated lungs (in red) also listed in Table 3.2. The boxes represent the first quartile, the mean and third quartile, and the whiskers represent the minimum and maximum of each group's dataset. Note that the control group was only composed of 3 lungs, not allowing a box plot. A Student's t-test (α = 0.05) has been used to test the statistical difference between the two groups. The null hypothesis is assuming no statistically significant difference between the control and the PPE-treated

groups. $T_1^{EV(f)}$ and $T_1^{EV(sl)}$ exhibited p-values of 0.00517 and 0.03629 respectively. These values suggest that the two T_1^{EV} markers are useful biomarkers for the elastase model of emphysema and may be used as a sensor for changes of the MAA in the lungs.

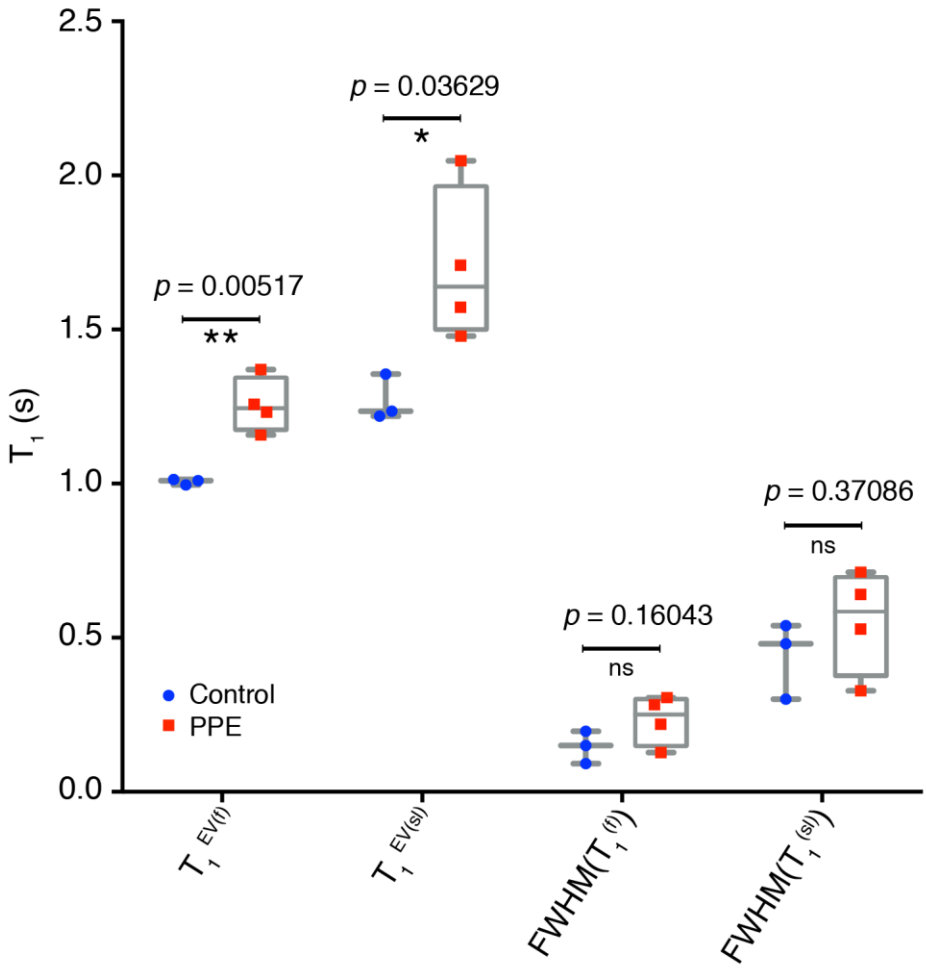

Figure 3.8 Boxplot of the characteristic data listed in Table 3.2. The MRI $T_1^{EV(f)}$ data between control and elastase (PPE) group do not overlap. The same observation is made for the $T_1^{EV(sl)}$ data. In contrast, the distribution of T_1 values for the two modes of the histograms (characterized by $FWHM(T_1)$) significantly overlaps between control and PPE groups, indicating no significant statistical difference from the T_1 spread. However, the variation in $T_1^{EV(sl)}$ is more pronounced in the treated animals than in the control animals.

3.3.3. ^{83}Kr T_1 relaxation as a biomarker of the alveolar dimensions

The non-significant difference of the whole lung MAA between the lungs used for histology only and the lungs used for MRI and histology allows for a clustering of the data in a control group and an emphysema group (Figure 3.1). The mean control MAA was $26654 \pm 7586\ \mu m^2$ whereas the mean PPE-treated MAA was $59809 \pm 23788\ \mu m^2$ (Figure 3.9), confirming an increase of the alveolar dimensions caused by the proteinase. As expected, a p-value of 0.0121 calculated with the Mann-Whitney U-test reveals a significantly different MAA in the control and the emphysema groups.

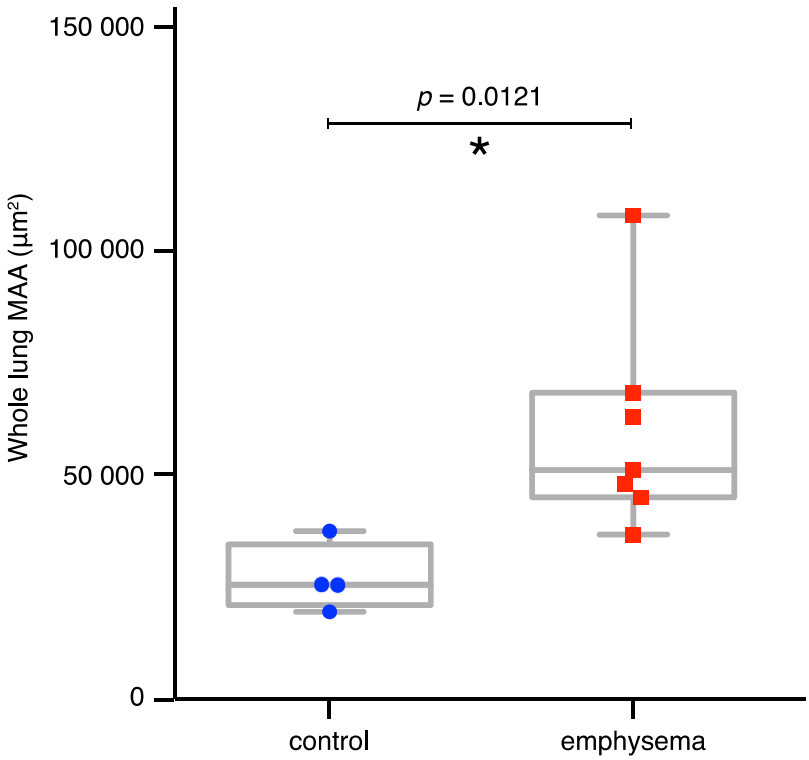

Figure 3.9 Box and whiskers plot representing the repartition of the histological data in the control and emphysema groups. Bars in the box represent the mean, the first and third quartiles of the distribution, the whiskers bars represent the minimum and maximum. A significant difference between the two groups' whole lung MAA is observed.

The potential relationship between the SQUARE data T_1^{EV}, and the histological data MAA has been analysed. It has been previously shown that ^{83}Kr $T_1 \propto {}^{V}/_{S}$ (2). In this work, a significant statistical difference has been observed between the control group and the PPE-treated group lungs for the $T_1^{EV(f)}$, $T_1^{EV(sl)}$ and

the whole lung MAA (Figure 3.8 and Figure 3.9). The correlation between $T_1^{EV(f)}$, $T_1^{EV(sl)}$ and MAA was evaluated. Previous findings in material science showed that in presence of packed spherical beads, a relationship between the ^{83}Kr relaxation rate R_1 and the surface-to-volume ratio was observed, ^{83}Kr R_1 was therefore proportional to the inverse radius of the beads (2). Consequently, the assumption that ^{83}Kr R_1 was behaving similarly in the lungs was established. Assuming naively a spherical alveolar geometry, R_1 is expected to be proportional to the inverse of the alveolar radius (r) (Eq. 3.1 to 3.3), therefore proportional to the inverse of the $\sqrt{MAA}$.

$$1/T_1 \propto S/V \quad \text{Eq. 3.1}$$

$$S/V \propto 1/r \quad \text{Eq. 3.2}$$

$$R_1 = 1/T_1 \propto 1/r \quad \text{Eq. 3.3}$$

Note that even in the cases of model surfaces, deviation from this dependency was observed due to non-uniform bead size and varying beads surfaces microstructure (2). Nevertheless, this behaviour can be assumed as an initial guess for the pulmonary data where it provides a reasonable starting point. In the following, the relationship between the two T_1 modes of the SQUARE maps histograms and the whole lung mean alveolar area will be evaluated. Subsequently, the mean lobar T_1 calculated from regions of interest directly in the SQUARE maps will be compared to the corresponding histological lobar mean alveolar area.

	$R_1^{EV(f)} = 1/T_1^{EV(f)}$ (s^{-1})	$error = T_1^{-2} \times FWHM$ (s^{-1})	$1/\sqrt{MAA}$ ($10^{-3}\ \mu m^{-1}$)	$error = \frac{1}{2} MAA^{-\frac{3}{2}} \times stdevMAA$ ($10^{-3}\ \mu m^{-1}$)
CL.2	0.987167	0.0889074	6.32455	0.126491
CL.3	0.990197	0.146946	5.19875	0.42152
EL.1	0.796242	0.0809619	3.98409	0.347818
EL.2	0.812282	0.201226	3.83483	0.31017
EL.3	0.730087	0.150324	4.42807	0.434125
EL.4	0.863856	0.163988	4.71405	0.31427
EL.5	1.0527	0.147719	5.27046	0.732009

Table 3.3 Characteristic ^{83}Kr $R_1^{EV(f)}$ parameters and $1/\sqrt{MAA}$ histological data with their respective errors used for correlation analysis.

	$R_1^{EV(sl)} = 1/T_1^{EV(sl)}$ (s^{-1})	$error = T_1^{-2} \times FWHM$ (s^{-1})	$1/\sqrt{MAA}$ ($10^{-3}\ \mu m^{-1}$)	$error = \frac{1}{2} MAA^{-\frac{3}{2}} \times stdevMAA$ ($10^{-3}\ \mu m^{-1}$)
CL.2	0.820411847	0.820411847	6.32455	0.126491
CL.3	0.737680732	0.737680732	5.19875	0.42152
EL.1	0.676269696	0.149948296	3.98409	0.347818
EL.2	0.585926056	0.180834763	3.83483	0.31017
EL.3	0.488424343	0.152407766	4.42807	0.434125
EL.4	0.636618284	0.28857354	4.71405	0.31427
EL.5	0.815860325	0.299532631	5.27046	0.732009

Table 3.4 Characteristic ^{83}Kr $R_1^{EV(sl)}$ parameters and $1/\sqrt{MAA}$ histological data with their respective errors used for correlation analysis.

3.3.3.1. Whole lung ^{83}Kr relaxation as a biomarker for whole lung mean alveolar area

Tables 3.3 and 3.4 show data for the fast and slow relaxation components of the bimodal relaxation behaviour $R_1^{EV(f)}$, $R_1^{EV(sl)}$ and the inverse square root of the whole lung mean alveolar area, $1/\sqrt{MAA}$. As functions of the measured variables were used for correlation analysis, the uncertainty was calculated for each plotted variable using the propagation of uncertainty equation (Eq. 3.4).

$$\Delta(F) = \sqrt{\left(\frac{\partial F}{\partial x}\right)^2 \Delta^2(x)} \qquad \text{Eq. 3.4}$$

Where the error is $\Delta(x) = FWHM$ for the T_1^{EV} variables and $\Delta(x) = StDev(MAA)$ for the MAA variable.

The relationship between the relaxation rates $R_1^{EV(f)}$ and $R_1^{EV(sl)}$ and $1/\sqrt{MAA}$ is represented in Figure 3.10 where the error bars represent the error propagated from the T_1^{EV} and MAA measurements.

Linear regression following the least-square method using GraphPad Prism version 6.0 (GraphPad Software, La Jolla, California, USA) led to linear fitting (Figure 3.10), following the linear equations Eq. 3.5 and Eq. 3.6 for the fast and the slow T_1 mode respectively.

$$R_1^{EV(f)} = 107.5 \times 1/\sqrt{MAA} + 0.3719 \qquad \text{Eq. 3.5}$$

$$R_1^{EV(sl)} = 105.7 \times 1/\sqrt{MAA} + 0.1704 \qquad \text{Eq. 3.6}$$

A linear correlation is observed between the relaxation rates $R_1^{EV(f)}$ and $R_1^{EV(sl)}$ and the histological measurements $1/\sqrt{MAA}$ with a coefficient of determination $r^2 = 0.59$ and $r^2 = 0.56$ respectively, the value $0.5 < r^2 < 1$ suggests that the linear model is an appropriate model confirming a strong association between the MRI variables R_1^{EV} and the histological variable $1/\sqrt{MAA}$. In fact, 59 % of the variation in $R_1^{EV(f)}$ and 56 % of the variation in $R_1^{EV(sl)}$ can be explained by a change in $1/\sqrt{MAA}$.

A F-test has also been used to confirm the slope was significantly deviated from a zero-slope line, about the mean value of R_1^{EV}. A $p - value = 0.0436$

and $p - value = 0.0536$ was observed for the $R_1^{EV(f)}$ and $R_1^{EV(sl)}$ fittings respectively, confirming a significant deviation of the correlation line from the zero-slope for the $R_1^{EV(f)}$ linear fitting, whereas $R_1^{EV(sl)}$ was not significantly deviating from a zero-slope line. This can be explained by the higher T_1 values in the T_1 map predominantly arising from the main airways, which were not included in the MAA measurements. But it can also be caused by an important alveolar destruction due to the elastase treatment; in which case, the relaxation behaviour will depend on many other variables such as the diffusion of the hp ^{83}Kr atoms to adjacent intact alveoli, or even a modification of the surface chemistry in the alveoli.

A higher correlation was observed between $R_1^{EV(f)}$ and $1/\sqrt{MAA}$ (Figure 3.10.a) than $R_1^{EV(sl)}$ (Figure 3.10.b). This higher correlation was expected as the fast mode $T_1^{EV(f)}$ was exhibiting higher significant difference between the two groups (Figure 3.8). The fastest $R_1^{EV(f)}$ values are produced by the alveolar parenchyma. Consequently, the correlation between $R_1^{EV(f)}$ and $1/\sqrt{MAA}$ means changes in $R_1^{EV(f)}$ directly depend on the alveolar radius.

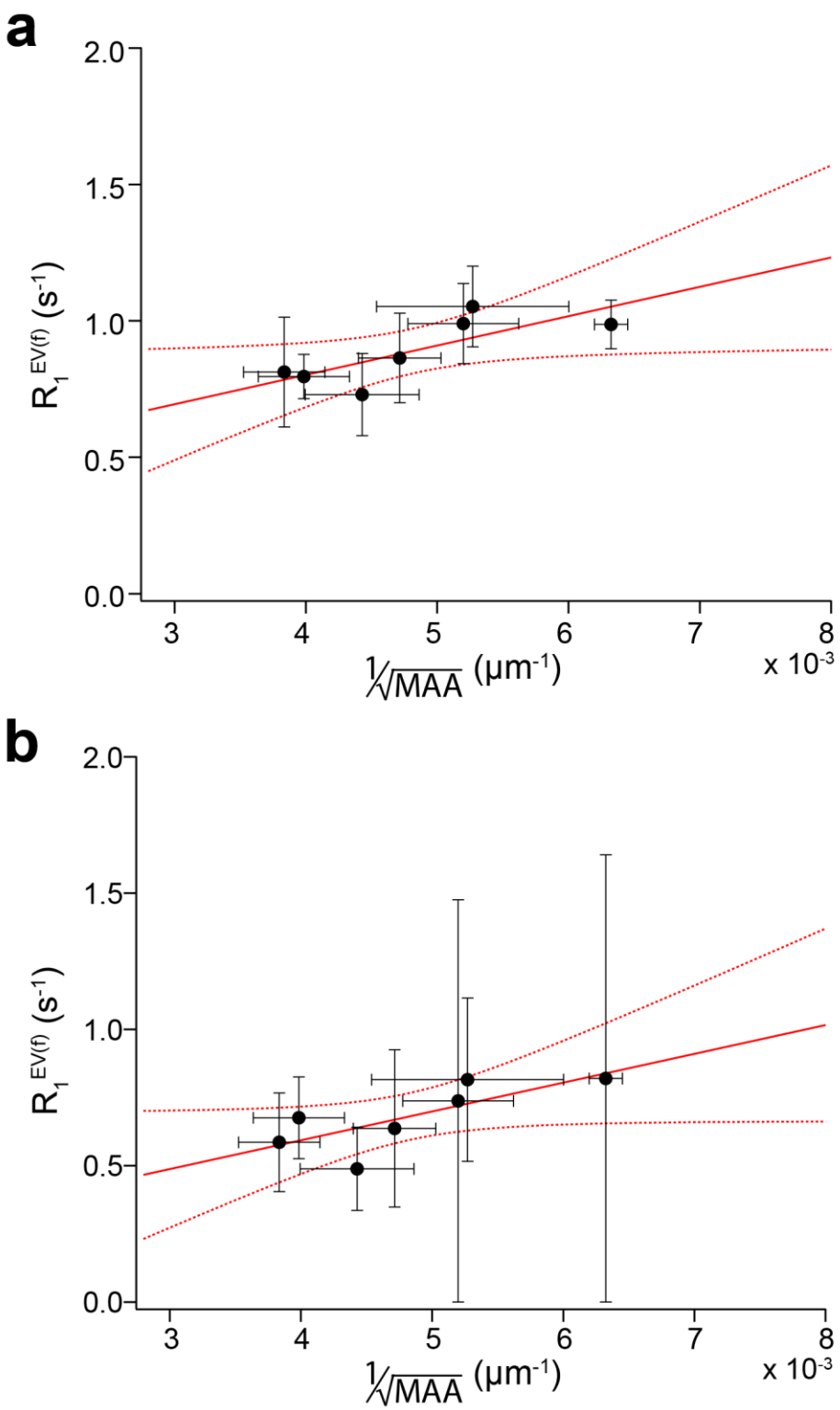

Figure 3.10 Scatter diagram of the relaxation rates $R_1^{EV(f)}$ (a) and $R_1^{EV(sl)}$ (b) of the fast mode and slow mode of the bimodal fitting respectively against $1/\sqrt{MAA}$. Error bars represent the propagated error for the two variables in x and y. The best-fitting linear regression line is plotted in solid red line with the 95 % confidence interval in dotted red line.

3.3.3.2. Regional ^{83}Kr relaxation as a biomarker for lobar mean alveolar area

Six et al. showed longer T_1 in the airways than in the parenchyma where the S/V ratio is higher (3). One could expect that the alveolar wall degradation caused by the elastase proteinase will create a regional ^{83}Kr SQUARE contrast. Region of interests were manually selected when clearly visible using ImageJ (Imagej.nih.gov/ij/, National Institutes of Health, USA). The mean T_1 value and standard deviation were measured in regions of interest from the right cranial lobe, the right caudal lobe, and left lobe, which were the only lobes identifiable with certainty. The right middle lobe and the right accessory lobe were not included because of their difficulty to differentiate from the surrounding lobes. More lobes were excluded from the data analysis when a ventilation defect was observed in this lobe or near the region of interest. The average T_1 and corresponding standard deviation are measured for each lobar region, and the calculated R_1 data and inversed squared root of MAA are reported in Table 3.5.

The relationship between the lobar R_1 and $1/\sqrt{lobarMAA}$ is represented in Figure 3.11. Linear regression using the least-square method led to a linear fitting with the equation (Eq. 3.7):

$$R_1 = 71.7 \times 1/\sqrt{lobarMAA} + 0.4735 \qquad \text{Eq. 3.7}$$

A linear correlation is observed between the two parameters, with a coefficient of determination $r^2 = 0.61$. Similarly to the whole lung characteristic R_1^{EV} modes analysis, this coefficient suggests that the linear model is an appropriate model to quantitatively correlate the two variables. More than 60 % of the changes in lobar R_1 can be explained by the changes in $1/\sqrt{lobarMAA}$. This is in agreement with the previous results correlating R_1^{EV} with $1/r$.

A F-test confirmed the slope was significantly deviated from a zero-slope line, about the mean value of lobar R_1, with a $p - value < 0.0001$.

	Lobe	ROI area (voxels)	$R_1 = 1/T_1$ (s^{-1})	$error = T_1^{-2} \times stdevT_1$ (s^{-1})	$1/\sqrt{lobarMAA}$ (10^{-3} µm^{-1})	$error = \frac{1}{2} MAA^{-\frac{3}{2}} \times stdevMAA$ (10^{-3} µm^{-1})
CL.2	Left	189	0.9751341	0.072771	0.006437618	0.000527179
	Right cranial	48	0.8928571	0.128348	0.006318761	0.000503071
	Right caudal	89	0.9242144	0.064063	0.006668633	0.00078311
CL.3	Right cranial	60	0.9337068	0.209234	0.005533474	0.000865373
	Right caudal	91	0.9578544	0.111016	0.006875601	0.000330779
EL.1	Left	96	0.8237232	0.054282	0.005558919	0.001667787
	Right cranial	58	0.7593014	0.078986	0.004738923	0.000650874
	Right caudal	149	0.7867821	0.095330	0.003811215	0.000574466
EL.2	Left	69	0.6161429	0.192473	0.003535096	0.000762941
	Right cranial	80	0.7980846	0.112101	0.004050135	0.001570891
	Right caudal	98	0.7042254	0.047610	0.003964682	0.000797613
EL.3	Left (upper)	57	0.7220217	0.037013	0.005199137	0.000389679
	Left (lower)	98	0.7593014	0.067455	0.003413924	0.001215676
	Right cranial	47	0.7220217	0.037013	0.004596865	0.000687732
	Right caudal	93	0.8591065	0.071592	0.003675152	0.000659299
EL.4	Left (upper)	55	0.8012821	0.066774	0.004200986	0.000965453
	Right cranial	69	0.8474576	0.076846	0.004258851	0.000853734
EL.5	Right cranial	77	0.9514748	0.077856	0.007354658	0.001105535
	Right caudal	158	1.1248594	0.129061	0.006907996	0.001492845

Table 3.5 Mean lobar ^{83}Kr R_1 and $1/\sqrt{lobarMAA}$ lobar histological data with their respective errors used for correlation analysis.

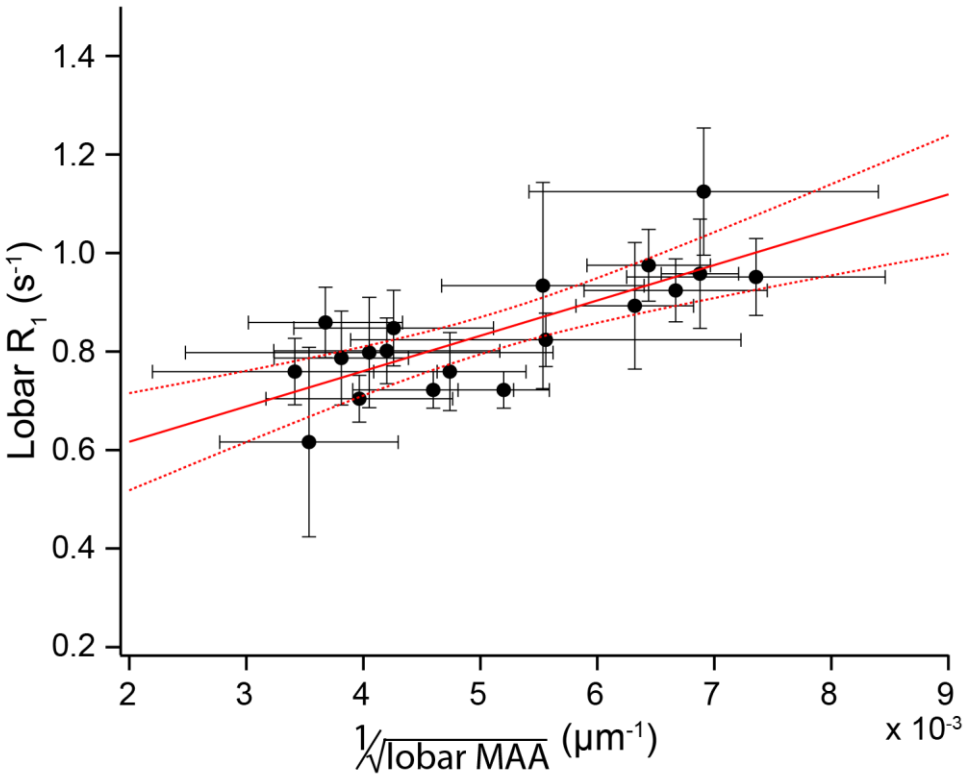

Figure 3.11 Scatter diagram of the lobar relaxation rate R_1 against $1/\sqrt{lobarMAA}$. Error bars represent the propagated error for the two variables in x and y. The best-fitting linear regression line is plotted in solid red line with the 95 % confidence interval in dotted red line.

3.4. Conclusions

This study investigated the effect of the alveolar destruction on the hyperpolarized ^{83}Kr relaxation in the elastase animal model of emphysema. The elastase rat model consists in degrading the alveolar extracellular matrix using the porcine pancreatic elastase (PPE). The induced increase in surface-to-volume (S/V) ratio in the parenchyma of the treated animals was observed *post* mortem with a significant increase of the mean alveolar area (MAA) (Figure 3.9).

Hyperpolarized ^{83}Kr ventilation coronal imaging of the lungs shows some spin density heterogeneities where the gas is not delivered to the lungs (Figure 3.3). An heterogeneous gas distribution was also observed in hyperpolarized ^{3}He and ^{129}Xe human studies of COPD (20,44-47) and rodent models of emphysema (48,49). These ventilation defects can be explained by some airways obstruction, but also by a loss of elasticity inducing a reduced inflation of the diseased overdistended rigid parenchyma (24). These ventilation defects

were emphasized by using ^{129}Xe spin density imaging as ^{129}Xe has a higher viscosity than ^{3}He and a 6 times lower diffusion coefficient (50). It has been shown that ventilation imaging was not an adequate technique to at early stages of COPD (30) whereas the apparent diffusion coefficient imaging has shown to be more effective and was correlated to the alveolar S/V ratio (18,19).

The hyperpolarized ^{83}Kr imaging of the elastase animal model permitted a three levels analysis of the surface quadrupolar relaxation (SQUARE) contrast in the lungs.

Pulmonary T_1 maps with an appropriately chosen colour code permit a visual assessment of the hyperpolarized ^{83}Kr relaxation behaviour within the lungs. The two groups were easily differentiable just by their respective T_1 maps overall appearance. The control lungs were showing a mostly blue map whereas the PPE-treated lungs were more heterogeneously coloured with a tendency towards the greens (Figure 3.4 and Figure 3.5). This first level of analysis gives a qualitative evaluation of the slower relaxation in the impaired lungs.

The pixel counts of the previously described T_1 maps were plotted in histograms (Figure 3.4 and Figure 3.5). A cohort analysis of the histograms resulting from the T_1 maps from 3 control lungs and 4 PPE-treated lungs indicated a bi-modal Gaussian T_1 distribution within all lungs. The two T_1 modes are very likely to originate from two different pulmonary compartments. A fast component $T_1^{EV(f)}$ and a slow component $T_1^{EV(sl)}$ were observed in all lungs. Both were evaluated significantly faster in control lungs than PPE-treated lungs (Figure 3.8) and can therefore be considered as relevant biomarkers for surface degradation in the emphysematous rat lungs.

A correlation is observed between the two characteristics whole lung R_1^{EV} and the whole lung mean $1/\sqrt{MAA}$. This correlation between whole lung MRI data and histological data could allow some non-spatially resolved NMR evaluation of emphysematous lungs. However, the low S/V ratio in the main airways providing a significantly longer T_1 would bias the results, overestimating the alveolar destruction in all lungs. It is certainly possible to realise such a spectroscopic experiment, but it would require a well designed inhalation

scheme for the hyperpolarized ^{83}Kr, so that it is delivered to the alveoli only, filling the airways with thermal gas (51). This way, the signal would arise from the parenchyma only and the recorded T_1 would be comparable to $T_1^{EV(f)}$, that was recorded in the parenchymal areas of the imaged lungs.

The quadrupolar property of ^{83}Kr gives the atom the unique property to have a surface-induced relaxation. This property has been demonstrated in a porous model composed of packed beads of defined size (2). The ^{83}Kr relaxation rate R_1 was shown to be linearly correlated to the inverse of the beads radius. In this study, hyperpolarized ^{83}Kr relaxation behaviour has been directly compared with the alveolar radius. However, the alveolar radius was not a measured value. Considering the alveolus as a spherical unit, the histological mean alveolar area (MAA) was assumed circular. The alveolar radius was therefore estimated proportional to $\sqrt{MAA}$.

The relaxation values resulting from the whole lung $T_1^{EV(f)}$ and $T_1^{EV(sl)}$, $R_1^{EV(f)}$ and $R_1^{EV(sl)}$ respectively are shown to be inversely proportional to the whole lung $\sqrt{MAA}$ (Figure 3.10).

The regional ^{83}Kr relaxation was analysed by selecting regions of interest in each lobe from all the T_1 maps, without differentiating the cohorts. The lobar R_1 was inversely proportional to $\sqrt{lobar\ MAA}$ (Figure 3.11).

^{83}Kr R_1^{EV} and lobar R_1 were correlating only imperfectly with $1/\sqrt{MAA}$, with coefficients of determination evaluating the correlation not higher than 0.61. The initial hypothesis was that ^{83}Kr R_1 is correlated to the inverse of the alveolar radius. The deviation from this linear model might be due to the use of the MAA as histological data for an estimate of the alveolar radius despite a non-perfect spherical geometry of the alveoli. This imperfect correlation is also in accordance with the previously shown ^{83}Kr properties. Indeed, the hyperpolarized ^{83}Kr R_1 is not only dependent on the S/V ratio, but also on the surface chemistry. Different surface chemical compositions have been authenticated using hp ^{83}Kr NMR and MRI of hydrophobic-treated beads and non-treated beads (2,32), but also hp ^{83}Kr NMR and MRI of surfactant-treated beads, some of them exposed also to tobacco smoke (34). An acceleration of the T_1 relaxation was observed when the surface was coated with hydrophobic

agents, but also when in presence of tobacco smoke deposit. In the elastase-induced emphysema animal model, the proteolysis of extracellular matrix induces a secretory cells metaplasia, and a subsequent increase in mucous production, comparable to bronchitis (25,52,53). This change in alveolar surface chemistry, not measured in the MAA, is very likely to induce a faster relaxation of the hp ^{83}Kr. In addition, an imperfect spherical alveolar shape would also reduce the correlation between the two variables.

On an additional note, although the ^{83}Kr MRI results presented in this chapter were correlating with the histological marker mean alveolar area (MAA), some comparisons should be done with the intercept measurement, which is the most commonly used histological estimator for the volume-to-surface ratio in the lung (54).

This study has identified ^{83}Kr T_1 as an appropriate biomarker for the alveolar surface-to-volume ratio. This unique property allows the hyperpolarized noble ^{83}Kr gas to be used as a probe for the alveolar wall degradation induced by the elastase in a widely used animal model of emphysema in rodents. Some more experiments should be conducted to evaluate whether the numerical biomarker R_1 would also correlate with a pathologic alveolar change in surface chemistry. For example, an animal model of chronic bronchitis could be used to evaluate the ^{83}Kr T_1 relaxation behaviour in presence of a significantly increased production of mucus. All investigation should be accompanied by appropriate histological analysis measuring the mucous quantity changes.

The potential of this technique will be tested by Prof. Thomas Meersmann's research group at lower field, in a 7 T research human scanner. The T_1 relaxation will be measured for the first time at 7 T and in a larger scale alveolar system, close to the human alveolar dimensions. The first stage in this project towards human ^{83}Kr pulmonary imaging would be to acquire some ^{83}Kr spectroscopy in some large animal *ex vivo* lungs. The knowledge of the T_1 relaxation time in such a system will help to image the hyperpolarized ^{83}Kr in live human lungs. The expensive cost of a lung scan using isotopically enriched ^{83}Kr is an obstacle to the fast development of this technique for clinical application and broad use of it. Such problem can however be tackled thanks to the use of hydrogen as a buffer gas during the hyperpolarization

process. The replacement of nitrogen by hydrogen followed by a catalytic removal of this buffer gas induces a sevenfold increase of the apparent polarization (55), when isotopic enrichment provides an approximately eightfold signal increase. Even with the use of the expensive isotopically enriched gas, this technique could be useful for pharmaceutical trials where the cost of an experiment is less of a limitation. This technology could be used for drug testing in the case of novel treatments for COPD such as emphysema.

3.5. References

1. Lilburn DML, Lesbats C, Six JS, Dubuis E, Yew-Booth L, Shaw DE, Belvisi MG, Birrell MA, Pavlovskaya GE, Meersmann T. Hyperpolarized Kr-83 magnetic resonance imaging of alveolar degradation in a rat model of emphysema. Journal of the Royal Society Interface 2015;12(107).
2. Stupic KF, Cleveland ZI, Pavlovskaya GE, Meersmann T. Quadrupolar Relaxation of Hyperpolarized Krypton-83 as a Probe for Surfaces. Solid State Nuclear Magnetic Resonance 2006;29:79-84.
3. Six JS, Hughes-Riley T, Lilburn DML, Dorkes AC, Stupic KF, Shaw DE, Morris PG, Hall IP, Pavlovskaya GE, Meersmann T. Pulmonary MRI contrast using Surface Quadrupolar Relaxation (SQUARE) of hyperpolarized Kr-83. Magnetic Resonance Imaging 2014;32(1):48-53.
4. Ley-Zaporozhan J, Ley S, Kauczor H-U. Morphological and functional imaging in COPD with CT and MRI: present and future. Eur Radiol 2008;18(3):510-521.
5. World Health Statistics. Geneva, Switzerland: World Health Organization; 2011.
6. Mannino DM, Buist AS. Global burden of COPD: risk factors, prevalence, and future trends. Lancet 2007;370(9589):765-773.
7. Han MK, Agusti A, Calverley PM, Celli BR, Criner G, Curtis JL, Fabbri LM, Goldin JG, Jones PW, MacNee W, Make BJ, Rabe KF, Rennard SI, Sciurba FC, Silverman EK, Vestbo J, Washko GR, Wouters EFM, Martinez FJ. Chronic Obstructive Pulmonary Disease Phenotypes The Future of COPD. American Journal of Respiratory and Critical Care Medicine 2010;182(5):598-604.

8. Crystal RG. The alpha-1-antitrypsin gene and its deficiency states. Trends Genet 1989;5(12):411-417.

9. Crystal RG. Alpha-1-antitrypsin deficiency, emphysema, and liver disease - Genetic basis and strategies for therapy. Journal of Clinical Investigation 1990;85(5):1343-1352.

10. Global strategy for the diagnosis, management, and prevention of chronic obstructive pulmonary disease (updated 2016): Global Initiative for Chronic Obstructive Lung Disease; 2015.

11. Kinsman RA, Yaroush RA, Fernandez E, Dirks JF, Schocket M, Fukuhara J. Symptoms and experiences in chronic-bronchitis and emphysema. Chest 1983;83(5):755-761.

12. Thabut G, Dauriat G, Stern JB, Logeart D, Levy A, Marrash-Chahla R, Mal H. Pulmonary hemodynamics in advanced COPD candidates for lung volume reduction surgery or lung transplantation. Chest 2005;127(5):1531-1536.

13. Gould GA, Macnee W, McLean A, Warren PM, Redpath A, Best JJK, Lamb D, Flenley DC. CT measurements of lung density in life can quantitate distal airspace enlargement - an essential defining feature of human emphysema. Am Rev Respir Dis 1988;137(2):380-392.

14. Friedman PJ. Imaging studies in emphysema. Proceedings of the American Thoracic Society 2008;5(4):494-500.

15. Marsh S, Aldington S, Williams MV, Nowitz MR, Kingzett-Taylor A, Weatherall M, Shirtcliffe PM, McNaughton AA, Pritchard A, Beasley R. Utility of lung density measurements in the diagnosis of emphysema. Respir Med 2007;101(7):1512-1520.

16. Marshall H, Deppe MH, Parra-Robles J, Hillis S, Billings CG, Rajaram S, Swift A, Miller SR, Watson JH, Wolber J, Lipson DA, Lawson R, Wild JM. Direct visualisation of collateral ventilation in COPD with hyperpolarised gas MRI. Thorax 2012;67(7):613-617.

17. Woods JC, Choong CK, Yablonskiy DA, Bentley J, Wong J, Pierce JA, Cooper JD, Macklem PT, Conradi MS, Hogg JC. Hyperpolarized He-3 diffusion MRI and histology in pulmonary emphysema. Magn Reson Med 2006;56(6):1293-1300.

18. Salerno M, de Lange EE, Altes TA, Truwit JD, Brookeman JR, Mugler JP. Emphysema: Hyperpolarized helium 3 diffusion MR imaging of the lungs compared with spirometric indexes - Initial experience. Radiology 2002;222(1):252-260.

19. Swift AJ, Wild JM, Fichele S, Woodhouse N, Fleming S, Waterhouse J, Lawson RA, Paley MNJ, Van Beek EJR. Emphysematous changes and normal variation in smokers and COPD patients using diffusion He-3 MRI. European Journal of Radiology 2005;54(3):352-358.

20. Ouriadov A, Farag A, Kirby M, McCormack DG, Parraga G, Santyr GE. Lung Morphometry Using Hyperpolarized Xe-129 Apparent Diffusion Coefficient Anisotropy in Chronic Obstructive Pulmonary Disease. Magn Reson Med 2013;70(6):1699-1706.

21. Mata JF, Altes TA, Cai J, Ruppert K, Mitzner W, Hagspiel KD, Patel B, Salerno M, Brookeman JR, de Lange EE, Tobias WA, Wang HTJ, Cates GD, Mugler JP. Evaluation of emphysema severity and progression in a rabbit model: comparison of hyperpolarized He-3 and Xe-129 diffusion MRI with lung morphometry. J Appl Physiol 2007;102(3):1273-1280.

22. Gross P, Pfitzer EA, Tolker E, Babyak MA, Kaschak M. Experimental emphysema - its production with papain in normal and silicotic rats. Archives of Environmental Health 1965;11(1):50-58.

23. Shapiro SD. Animal models for COPD. Chest 2000;117(5):223S-227S.

24. Karlinsky JB, Snider GL. Animal models of emphysema. Am Rev Respir Dis 1978;117(6):1109-1133.

25. Antunes MA, Rocco PRM. Elastase-induced pulmonary emphysema: insights from experimental models. Anais Da Academia Brasileira De Ciencias 2011;83(4):1385-1395.

26. Knudsen L, Weibel ER, Gundersen HJG, Weinstein FV, Ochs M. Assessment of air space size characteristics by intercept (chord) measurement: an accurate and efficient stereological approach. J Appl Physiol 2010;108(2):412-421.

27. Munoz-Barrutia A, Ceresa M, Artaechevarria X, Montuenga LM, Ortiz-de-Solorzano C. Quantification of lung damage in an elastase-induced mouse model of emphysema. International journal of biomedical imaging 2012;2012:734734.

28. Vanoirbeek JAJ, Rinaldi M, De Vooght V, Haenen S, Bobic S, Gayan-Ramirez G, Hoet PHM, Verbeken E, Decramer M, Nemery B, Janssens W. Noninvasive and Invasive Pulmonary Function in Mouse Models of Obstructive and Restrictive Respiratory Diseases. Am J Respir Cell Mol Biol 2010;42(1):96-104.

29. Vidal D, Fortunato G, Klein W, Cortizo L, Vasconcelos J, Ribeiro-dos-Santos R, Soares M, Macambira S. Alterations in pulmonary structure by elastase administration in a model of emphysema in mice is associated with functional disturbances. Revista Portuguesa De Pneumologia 2012;18(3):128-136.

30. Peces-Barba G, Ruiz-Cabello J, Cremillieux Y, Rodriguez I, Dupuich D, Callot V, Ortega M, Arbo MLR, Cortijo M, Gonzalez-Mangado N. Helium-3 MRI diffusion coefficient: correlation to morphometry in a model of mild emphysema. European Respiratory Journal 2003;22(1):14-19.

31. Boudreau M, Xu X, Santyr GE. Measurement of 129Xe gas apparent diffusion coefficient anisotropy in an elastase-instilled rat model of emphysema. Magn Reson Med 2013;69(1):211-220.

32. Pavlovskaya GE, Cleveland ZI, Stupic KF, Meersmann T. Hyperpolarized Krypton-83 as a New Contrast Agent for Magnetic Resonance Imaging. Proceedings of the National Academy of Sciences of the United States of America 2005;102:18275-18279.

33. Cleveland ZI, Meersmann T. Density-independent contributions to longitudinal relaxation in Kr-83. ChemPhysChem 2008;9(10):1375-1379.

34. Cleveland ZI, Pavlovskaya GE, Stupic KF, Wooten JB, Repine JE, Meersmann T. Detection of Tobacco Smoke Deposition by Hyperpolarized Krypton-83 MRI. Magnetic Resonance Imaging 2008;26:270-278.

35. Cleveland ZI, Stupic KF, Pavlovskaya GE, Repine JE, Wooten JB, Meersmann T. Hyperpolarized ^{83}Kr and ^{129}Xe NMR Relaxation Measurements of Hydrated Surfaces: Implications for Materials Science and Pulmonary Diagnostics. J Am Chem Soc 2007;129(6):1784-1792.

36. Ballard PL, Gonzales LW, Godinez RI, Godinez MH, Savani RC, McCurnin DC, Gibson LL, Yoder BA, Kerecman JD, Grubb PH, Shaul PW. Surfactant Composition and Function in a Primate Model of Infant Chronic

Lung Disease: Effects of Inhaled Nitric Oxide. Pediatr Res 2006;59(1):157-162.

37. Lilburn DML, Hughes-Riley T, Six JS, Shaw DE, Pavlovskaya GE, Meersmann T. Validating excised rodent lung for functional hyperpolarized xenon-129 MRI. 2013.

38. Snider GL, Lucey EC, Stone PJ. Animal-Models of Emphysema. Am Rev Respir Dis 1986;133(1):149-169.

39. Belloni PN, Garvin L, Mao CP, Bailey-Healy I, Leaffer D. Effects of all-trans-retinoic acid in promoting alveolar repair. Chest 2000;117(5):235S-241S.

40. Birrell MA, Wong S, Hele DJ, McCluskie K, Hardaker E, Belvisi MG. Steroid-resistant inflammation in a rat model of chronic obstructive pulmonary disease is associated with a lack of nuclear factor-kappa B pathway activation. American Journal of Respiratory and Critical Care Medicine 2005;172(1):74-84.

41. Hughes-Riley T, Six JS, Lilburn DML, Stupic KF, Dorkes AC, Shaw DE, Pavlovskaya GE, Meersmann T. Cryogenics free production of hyperpolarized 129Xe and 83Kr for biomedical MRI applications. J Magn Reson 2013;237:23-33.

42. Stupic KF, Cleveland ZI, Pavlovskaya GE, Meersmann T. Hyperpolarized Xe-131 NMR spectroscopy. J Magn Reson 2011;208(1):58-69.

43. Zhao L, Mulkern R, Tseng CH, Williamson D, Patz S, Kraft R, Walsworth RL, Jolesz FA, Albert MS. Gradient-echo imaging considerations for hyperpolarized Xe-129 MR. Journal of Magnetic Resonance Series B 1996;113(2):179-183.

44. Kirby M, Svenningsen S, Kanhere N, Owrangi A, Wheatley A, Coxson HO, Santyr GE, Paterson NAM, McCormack DG, Parraga G. Pulmonary ventilation visualized using hyperpolarized helium-3 and xenon-129 magnetic resonance imaging: differences in COPD and relationship to emphysema. J Appl Physiol 2013;114(6):707-715.

45. Salerno M, Altes TA, Mugler JP, Nakatsu M, Hatabu H, de Lange EE. Hyperpolarized noble gas MR imaging of the lung: Potential clinical applications. European Journal of Radiology 2001;40(1):33-44.

46. Fain SB, Panth SR, Evans MD, Wentland AL, Holmes JH, Korosec FR, O'Brien MJ, Fountaine H, Grist TM. Early emphysematous changes in asymptomatic smokers: Detection with He-3 MR imaging. Radiology 2006;239(3):875-883.

47. Kirby M, Kanhere N, Etemad-Rezai R, McCormack DG, Parraga G. Hyperpolarized helium-3 magnetic resonance imaging of chronic obstructive pulmonary disease exacerbation. Journal of Magnetic Resonance Imaging 2013;37(5):1223-1227.

48. Perez-Sanchez JM, de Alejo RP, Rodriguez I, Cortijo M, Peces-Barba G, Ruiz-Cabello J. In vivo diffusion weighted F-19 MRI using SF6. Magn Reson Med 2005;54(2):460-463.

49. Chen XJ, Hedlund LW, Moller HE, Chawla MS, Maronpot RR, Johnson GA. Detection of emphysema in rat lungs by using magnetic resonance measurements of He-3 diffusion. Proceedings of the National Academy of Sciences of the United States of America 2000;97(21):11478-11481.

50. Kirby M, Svenningsen S, Owrangi A, Wheatley A, Farag A, Ouriadov A, Santyr GE, Etemad-Rezai R, Coxson HO, McCormack DG, Parraga G. Hyperpolarized He-3 and Xe-129 MR Imaging in Healthy Volunteers and Patients with Chronic Obstructive Pulmonary Disease. Radiology 2012;265(2):600-610.

51. Stupic KF, Elkins ND, Pavlovskaya GE, Repine JE, Meersmann T. Effects of pulmonary inhalation on hyperpolarized krypton-83 magnetic resonance T-1 relaxation. Phys Med Biol 2011;56(13):3731-3748.

52. Campbell EJ. Animal models of emphysema: the next generations. Journal of Clinical Investigation 2000;106(12):1445-1446.

53. Breuer R, Christensen TG, Lucey EC, Bolbochan G, Stone PJ, Snider GL. Elastase causes secretory discharge in bronchi of hamsters with elastase-induced secretory-cell metaplasia. Exp Lung Res 1993;19(2):273-282.

54. Weibel ER. Stereological Methods. Vol. 1. Practical Methods for Biological Morphometry. Journal of Microscopy 1981;121(1):131-132.

55. Rogers NJ, Hill-Casey F, Stupic KF, Six JS, Lesbats C, Rigby SP, Fraissard J, Pavlovskaya GE, Meersmann T. Molecular hydrogen and catalytic combustion in the production of hyperpolarized Kr-83 and Xe-129 MRI

contrast agents. Proceedings of the National Academy of Sciences of the United States of America 2016;113(12):3164-3168.

CHAPTER 4

HP ^{129}XE CHEMICAL EXCHANGE RELAXATION TRANSFER OF CRYPTOPHANE-GDDOTA BIOSENSORS

The results presented in this chapter appear in the journal communication: Francesco Zamberlan[†], Clémentine Lesbats[†], Nicola J. Rogers, James L. Krupa, Galina E. Pavlovskaya, Neil R. Thomas, Henryk M. Faas and Thomas Meersmann, "Molecular Sensing with Hyperpolarized ^{129}Xe Using Switchable Chemical Exchange Relaxation Transfer", ChemPhysChem. (2015) 16: 2294–2298.

Chemical synthesis of the different molecules was carried out by Dr. Francesco Zamberlan with the assistance of James L. Krupa and supervision of Prof. Neil R. Thomas and Henryk M. Faas. The samples preparation was done by Dr. Francesco Zamberlan. The experimental apparatus for the NMR experiments was designed and assembled by Clémentine Lesbats and Dr. Nicola Rogers, supervised by Prof. Thomas Meersmann and Galina E. Pavlovskaya. Relaxation measurements were performed by Clémentine Lesbats, Dr. Nicola J. Rogers and Dr. Francesco Zamberlan. Clémentine Lesbats would be responsible of the polarizer and gas delivery while Dr. Nicola J. Rogers or Dr. Francesco Zamberlan would run the spectrometer. Clémentine Lesbats performed the data processing.

4.1. Introduction

The xenon's high solubility in biologic tissues and fluids is used in medical anaesthesia, and is now of great interest to research in hyperpolarized gas lung imaging. ^{129}Xe's solubility in tissue, red blood cells and plasma has been vastly studied in the last decade. The wide chemical shift arising from the different phases has allowed dissolved phase spectroscopy and imaging in animal and human lungs (1-4).

The National Institutes of Health (NIH) defined a biomarker as "a characteristic that is objectively measured and evaluated as an indicator of normal biological processes, pathogenic processes, or pharmacologic responses to a therapeutic intervention" (5). By monitoring biomarkers *in vivo*, molecular imaging has allowed progress in disease or treatment monitoring but also drug development. Hp ^{129}Xe can be used for molecular sensing. This is usually realised thanks to encapsulating agents such as cryptophane cages (6-8). Cryptophane A is a large molecule which main characteristic is its 5.7 Å diameter cavity (9) able to encapsulate the hyperpolarized ^{129}Xe (4.3 Å diameter) dissolved in solution. ^{129}Xe encapsulated in molecular cages produces a signal located at an independent chemical shift, about 100 ppm upfield to the ^{129}Xe signal from the bulk solvent often located around 200 ppm. The biosensors pioneered by Pines, Wemmer, and co-workers, but also used by Berthault, Schröder and their respective coworkers were composed of a cryptophane A (CrA) able to encapsulate ^{129}Xe, connected by a linker to a ligand that will bind another molecule. The chemical shift of the signal produced by the biosensor will vary depending on its molecular conformation or the complexation with the ligand or not for example. The first functionalised CrA biosensor was composed of a short linker and a biotin ligand, capable of complexation with avidin (6, 7). The protein binding led to an important broadening of the signal and a shift of the signal 3 ppm downfield. Berthault and coworkers modified the cryptophane molecule, making it soluble in water at a physiological pH, suitable for injection in the bloodstream (10).

A major difficulty with the detection of the hyperpolarized biosensor signal is the low signal intensity due to low concentration of cages (i.e. the actual biosensors molecules) and by extension of the cage bound hp ^{129}Xe. In order to improve the signal to noise ratio (SNR), one could increase the concentration

to the extent possible for *in vivo* application. The hp ^{129}Xe local concentration has also been increased by using the bacteriophage M13 as a scaffold for numerous CrA to covalently bind to its outer proteins (11). Another way to improve the SNR would be to do some signal averaging and selective excitation of the cage-bound ^{129}Xe, allowing for some fast exchange with the bulk hyperpolarized ^{129}Xe. The large chemical shift between the bulk signal and the ^{129}Xe in cage signal easily allows selective excitation pulses. Hyperpolarized ^{129}Xe Chemical Exchange Saturation Transfer (HyperCEST) uses this selective excitation to destroy the encapsulated ^{129}Xe signal, the constant chemical exchange with the dissolved phase induces a decrease of the dissolved phase signal, and this indirect detection allows a drastic improvement of the sensitivity over direct detection and averaging of the encapsulated hp ^{129}Xe (11, 12).

4.2. Motivation

Molecular sensing using encapsulated ^{129}Xe is usually based on the detection of a small chemical shift change up created by the change in conformation of the biosensor after interaction with a biomarker, such as an enzyme or a receptor (6, 7). This has been of particular interest for biomolecular NMR applications such as for *in vitro* assays and cells suspensions explorations (13), but the *in vivo* applications are often limited by the lower spectral resolution achievable in bigger coils and lower field, and more importantly in complex organisms.

Moreover, the cryptophane-bound ^{129}Xe phase signal intensity is very small to be detected; this work focuses on the ^{129}Xe signal from the solution in which the biosensor is dissolved, providing a larger source of signal.

Paramagnetic relaxation causes the rapid decay of the non-renewable ^{129}Xe signal, and is therefore usually avoided for hyperpolarized gases probes. As discussed in Chapter 3, noble gas induced relaxation can however be used as a source of contrast. ^{83}Kr longitudinal relaxation was shown to be linearly dependent on the surface-to-volume ratio in *ex vivo* rat lungs. The concept underlying this project is to use this disadvantage as a tool to create a positive contrast. In this work, the ^{129}Xe's solubility property is used to investigate a new sensor composed of a CrA, tethered to a gadolinium-DOTA chelate. The

paramagnetic property of gadolinium chelated in DOTA and attached to the CrA induces the fast decay of the dissolved hyperpolarized ^{129}Xe signal through fast exchange with the cage-bound ^{129}Xe. The rapid relaxation of the dissolved ^{129}Xe induced by the CrA-GdDOTA has been explored. This proof-of-concept study demonstrates a 'switchable' paramagnetic relaxation contract agent. The finale aim is to develop a biosensor that would lead to a positive contrast, providing a high hp ^{129}Xe signal when deactivated by the presence of the biormarker of interest.

Of course, the future design of the depolarizing biosensor will have to include some considerations, such as the length of the linker. Förster resonance energy transfer (FRET) shows a r^{-6} dependence of the fluorescence transfer efficiency between the donor and the acceptor (14). Similarly, the depolarization of the cage-bound ^{129}Xe caused by the paramagnetic GdDOTA will be dependent on the distance between them. The enzymatic cleavage of the linker will increase the distance between the paramagnetic agent and the host cage and deactivate it. The resulting cleavable biosensor will enable the detection of a biomarker and its spatial distribution, providing insights on physiological process such as enzymatic reactions within an organ.

4.3. Material and methods

4.3.1. Synthesis of the molecule

In this work, the model sensor consists of a Cryptophane A (CrA) and a gadolinium-DOTA (GdDOTA) chelate, a symmetrical linker was used to tether them together. CrA-GdDOTA was retrosynthesized from a DOTA chelator, modified with a short linker, and cryptophanol. This section gives a brief overview of the reactions leading to the final molecules. Further details on the chemical synthesis can be found in the supplementary information of the communication presenting this work (15).

CrA (Figure 4.1) was synthesized following Berthault and coworkers report (16). They used their biosensor *in vitro* as an intracellular probe for ^{129}Xe.

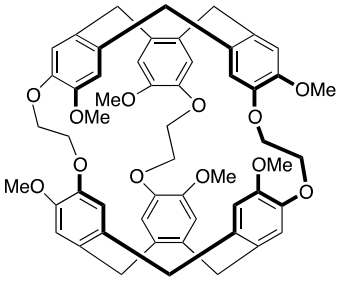

Figure 4.1 Cryptophane A molecule.

DOTA-linker was obtained by reacting an appropriately protected Do3A with one of the α-bromoacetyl termini of a short bisamide linker. The cryptophanol was then reacted with the other α-bromoacetyl group, leading to the CrA-DOTA compound in Figure 4.2.

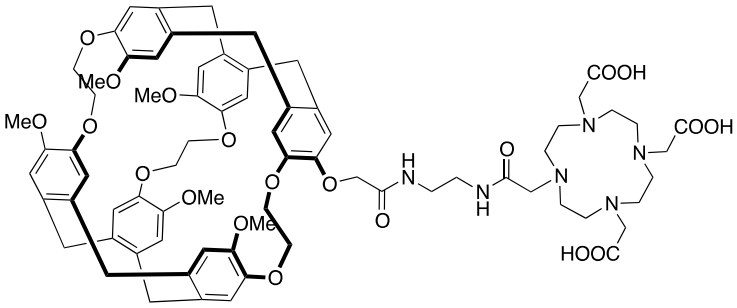

Figure 4.2 CrA-DOTA compound.

After deprotection of the DOTA carboxylic groups, the Gd^{3+} cation was successfully chelated, yielding to the compound CrA-GdDOTA, as showed in Figure 4.3.

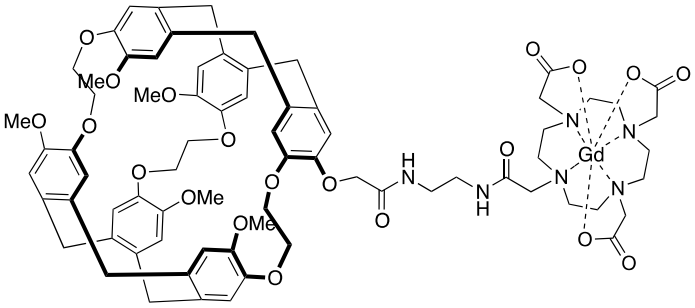

Figure 4.3 CrA-GdDOTA compound.

The biosensor was not soluble in H_2O. A 1:1 v/v mixture water and acetonitrile (H_2O/ACN) was found to be the most suitable solvent for the sensor, $Gd^{3+}_{(sol)}$, and ^{129}Xe. In this study, relaxation properties of 5 molecules, called Rx, have been compared:

- GdDOTA
- CrA-GdDOTA
- CrA-DOTA + $Gd^{3+}_{(sol)}$
- $Gd^{3+}_{(sol)}$
- CrA-DOTA

4.3.2. Experimental design

Hp ^{129}Xe gas was produced using batch mode spin exchange optical pumping (SEOP) in a custom built polarizer extensively described in Six et al. paper (17) with a 25 % natural abundance ^{129}Xe and 75 % N_2 gas mixture. The polarization build-up was achieved for 6 minutes at a temperature of 110 °C and a pump cell pressure of about 1300 mbar. Experiments have been performed on a 9.4 T spectrometer (Bruker BioSpin GmbH, Germany) at 293 K. All NMR spectra were obtained using a custom-built 15 mm double saddle coil tuned to the ^{129}Xe resonance frequency of 110.71546 MHz.

Prior to any spectrum acquisition, the sample was degassed from any trace of oxygen dissolved in solution by bubbling through it for 2 minutes with research grade nitrogen at 40 mL/min.

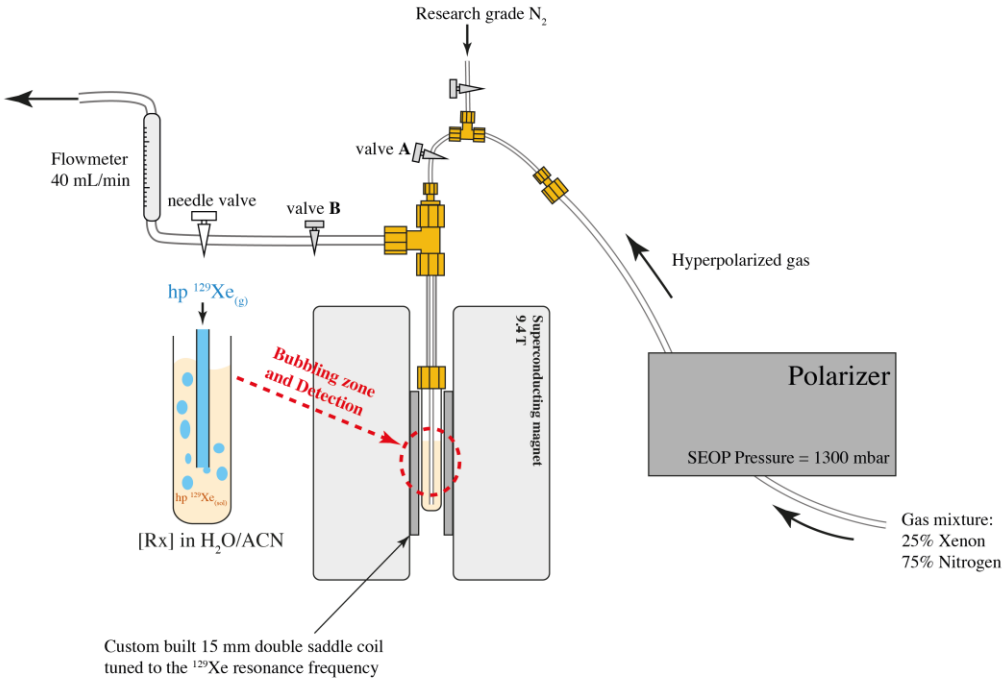

Figure 4.4 Overview of the experimental setup for hp $^{129}Xe_{(sol)}$ relaxation measurements. The gas mixture enters the polarizer to be hyperpolarized. After 6 minutes, it is delivered to the sample at a flow of 40 mL/min determined by the flowmeter at the end of the circuit. For spectrum acquisition no valve is closed, whereas valves A and B are closed for small flip angle T_1 measurement.

As sketched in Figure 4.4, a 5 mm sample tube containing 2 mL of the molecules Rx dissolved in 1:1 H_2O/ACN at different concentrations is connected to the polarizer delivering the hyperpolarized noble gas, and to a flowmeter and exhaust line. A research grade nitrogen line is also located before the test tube in order to degas the sample as described previously.

The hyperpolarized noble gas is flowed for 45 seconds at 40 mL/min before starting the spectrum acquisition sequence or T_1 measurement. This process allows replacing any nitrogen or dark gas (depolarized gas mixture) by freshly polarized noble gas mixture.

4.3.2.1. Continuous flow spin exchange optical pumping

The hyperpolarized noble gas is continuously delivered (40 mL/min) during the initial spectrum acquisition. This qualitative spectrum was used to verify the signal-to-noise level in both gas phase and dissolved phase. It also

permitted to determine the resonance frequency offset for later selective radiofrequency (RF) excitation pulses on the ^{129}Xe dissolved in solution.

4.3.2.2. Stopped flow spin exchange optical pumping

The hyperpolarized noble gas flow is interrupted during the longitudinal relaxation (T_1) sequence measurement. This is achieved by closing two manual valves A and B located before and after the sample tube (Figure 4.4).

4.3.3. NMR protocol for longitudinal relaxation measurements

^{129}Xe spectrum

A hyperpolarized ^{129}Xe spectrum is acquired prior to any relaxation measurements in order to identify and set the radiofrequency (RF) pulse to the dissolved phase resonance frequency.

A previously calibrated 90 ° hard pulse (63 µs, 3 dB) induces a free induction decay (FID). The spectral width was set to 30 kHz, with 8192 complex points. These parameters allowed a spectral width of 268.8 ppm, covering the entire range of ^{129}Xe frequencies in our system. Signal is averaged 8 times to compensate the weaker dissolved signal. The FID is Fourier transformed directly in Topspin 2.0 (Bruker, Germany) and the dissolved ^{129}Xe resonance frequency is determined.

^{129}Xe longitudinal relaxation

A sequence composed of 16 equally spaced small flip angle RF pulses (12 °) has been used to measure the T_1 relaxation times (Figure 4.5). As the time increases, signal decay will be caused by the T_1 relaxation, diffusion, but also by the RF pulse polarization destruction (18).

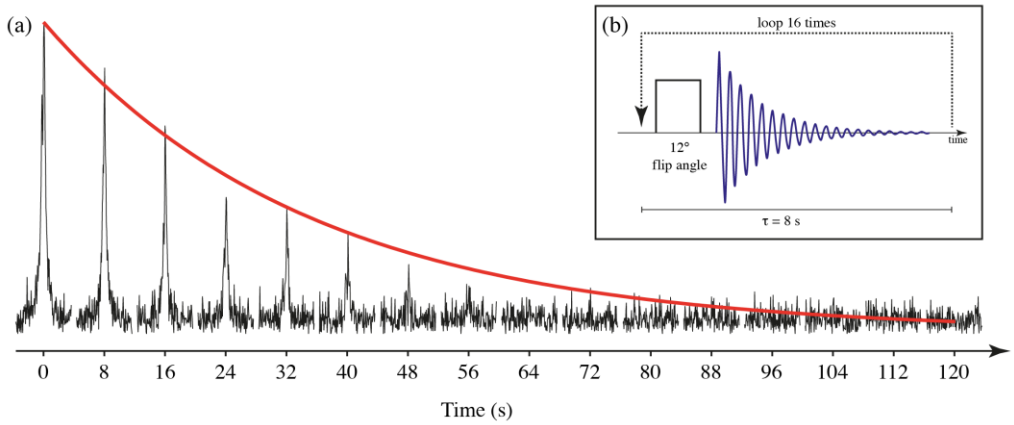

Figure 4.5 (a) Illustration of the hp ^{129}Xe dissolved in solution signal decay during a Small Flip Angle sequence and (b) schematics of the pulse sequence used. Spectra in black represent the dissolved ^{129}Xe in 0.07 mM CrA-GdDOTA in 1:1 H_2O/ACN, fitted with the Eq. 4.1 in red.

The FIDs were composed of 4096 complex points, with a spectral width of 6 250 Hz (equivalent to 56.4 ppm). The spectra are Fourier transformed, phase corrected and baseline corrected using Prospa (Magritek, Wellington, New Zealand). After Fourier transform, the signal intensity is integrated for each spectrum and normalised to the first and greater spectrum. T_1 is calculated using Igor Pro (Wavemetrics, Portland, USA) from a linear fitting of the natural logarithm of the normalised integrated signal of the spectra as a function of time (19) described by Eq. 4.1 to Eq. 4.4.

$$M_z(n) = M_z(0) \times cos^{\,n}(\theta) \times e^{-n \times \tau / T_1} \quad \text{Eq. 4.1}$$

$$\frac{M_z(n)}{M_z(0)} = \cos^n \theta \times e^{-n \times \tau / T_1} \quad \text{Eq. 4.2}$$

$$\ln\left(\frac{M_z(n)}{M_z(0)}\right) = n \times \ln(\cos\theta) - \frac{n \times \tau}{T_1} \quad \text{Eq. 4.3}$$

$$\ln\left(\frac{M_z(n)}{M_z(0)}\right) = n \times \left(\ln(\cos\theta) - \frac{\tau}{T_1}\right) \quad \text{Eq. 4.4}$$

The decay of the longitudinal magnetization M_z as a function of the excitation pulse number n, is caused by T_1 relaxation during the time $t = n \times \tau$. The fixed time constant τ is the time duration between two successive RF pulses. Furthermore, the polarization is diminished by $sin(\theta)$ by each of the small flip angle pulses. The remaining signal after n RF pulses is proportional to

$cos^n(\theta)$ and this term is multiplied by the exponential T_1 relaxation decay in the full equation (20).

^{1}H longitudinal relaxation

The proton signals produced from the bulk solution of water and acetonitrile have been identified prior to acquiring an inversion-recovery sequence that was used in order to evaluate T_1 in water. ^{1}H from the H_2O and the ACN molecules resonate at 4.79 ppm and 2.44 ppm respectively (Figure 4.6) in accordance with reported common laboratory solvents chemical shifts (21, 22).

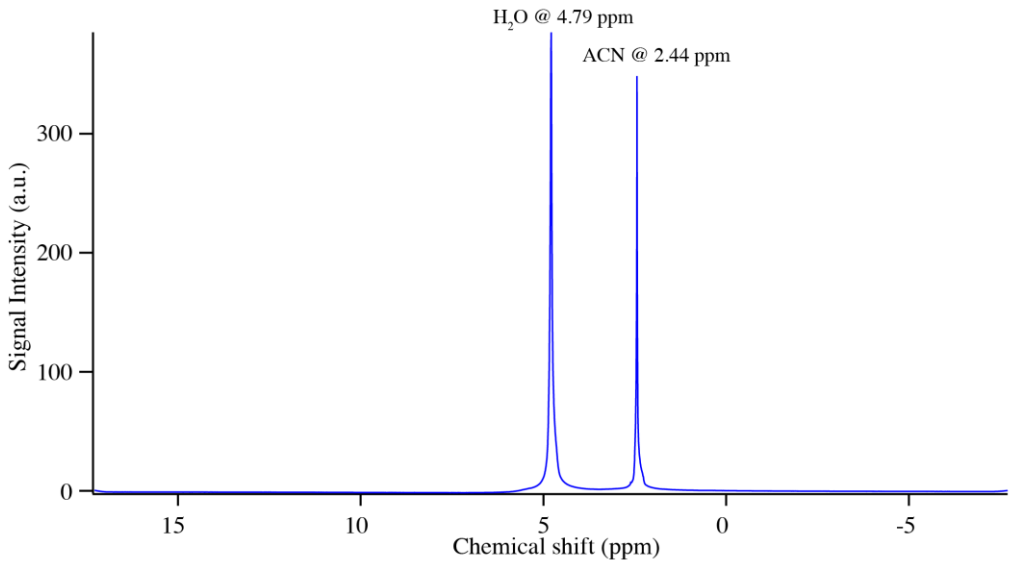

Figure 4.6 ^{1}H spectrum in a 2 mL sample of 1 mM GdDOTA dissolved in 1:1 ACN/H_2O. The spectral width was 10 000 Hz acquired with 8192 complex points.

The Topspin inversion-recovery 'T1ir' inbuilt sequence has been used to measure T_1 of proton in H_2O. The sequence consists of consecutive 180 ° and 90 ° pulses, separated by a delay τ (Figure 4.7.b). The first pulse rotates the net magnetization in the orientation of the –z axis. After a delay τ, the second pulse will rotate the magnetization of 90 ° in the xy plane. The signal intensity will therefore vary as a function of τ, time during the spin-lattice relaxation T_1 occurs. When $\tau < T_1$, very little of the magnetization will have returned to the +z axis, inducing a negative phase signal after the 90 °, resulting in a negative signal. When $\tau \gg T_1$, the magnetization will have fully recovered from the

inversion pulse, and the second 90 ° pulse will produce a maximal positive signal.

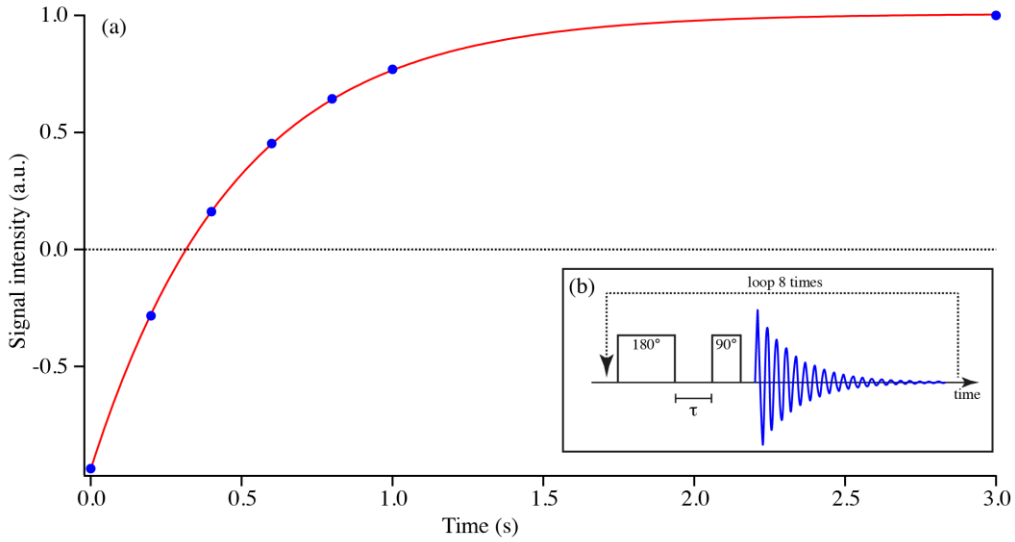

Figure 4.7 Inversion recovery NMR sequence. (a) in blue the experimental data point acquired with different τ in 0.5 mM GdDOTA dissolved in 2 mL 1:1 ACN/H_2O, fitted with the Eq. 4.2. in red. The inversion-recovery sequence has been sketched in (b).

The signal intensity for different τ has been plotted Figure 4.7.a with a zero-crossing point at $\tau = T_1 \times ln2$. The resulting fit can therefore be used to extrapolate T_1, according to Eq. 4.2.

$$I(\tau) = I_0 \times \left(1 - 2e^{-\frac{\tau}{T_1}}\right) \qquad \text{Eq. 4.2}$$

4.3.4. HPLC

High-Performance Liquid Chromatography (HPLC) is an analytical tool allowing the separation and identification of organic compounds. The different molecules will be separated depending on their adsorption level on a column they are flown through. In this experiment, HPLC has been used to follow the transformation of CrA-GdDOTA into CrA-DOTA, induced by the acidification of the solvent.

HPLC was performed using an Agilent 1200 series system at 1.0 mL/min equipped with a 4.6 x 150 mm Agilent Eclipse XDB-C18 analytical column with a 5 µm pore size and a single channel UV detector at λ = 215 nm. The mobile phase used was a 0.1 % formic acid in milli Q water solvent, followed by a gradient elution (0 to 95 % over 30 min) of a second solvent composed of 0.1 % formic acid in acetonitrile.

4.4. Results and discussion

After synthesis of CrA, a hp ^{129}Xe spectrum of CrA dissolved in chloroform ($CDCl_3$) has been acquired to verify that the ^{129}Xe signal arises from the three different phases. As illustrated in Figure 4.8 the three peaks identified as ^{129}Xe signal appear from the gas phase at 0 ppm, from the chloroform phase at 216 ppm and from the CrA cage at 64 ppm. Spence et al. already reported a ^{129}Xe signal in CrA peak located at 71 ppm using water as solvent in their study (6). In this study, the highly concentrated 13 mM CrA solution in $CDCl_3$ only allows a very small and broad peak arising from the CrA.

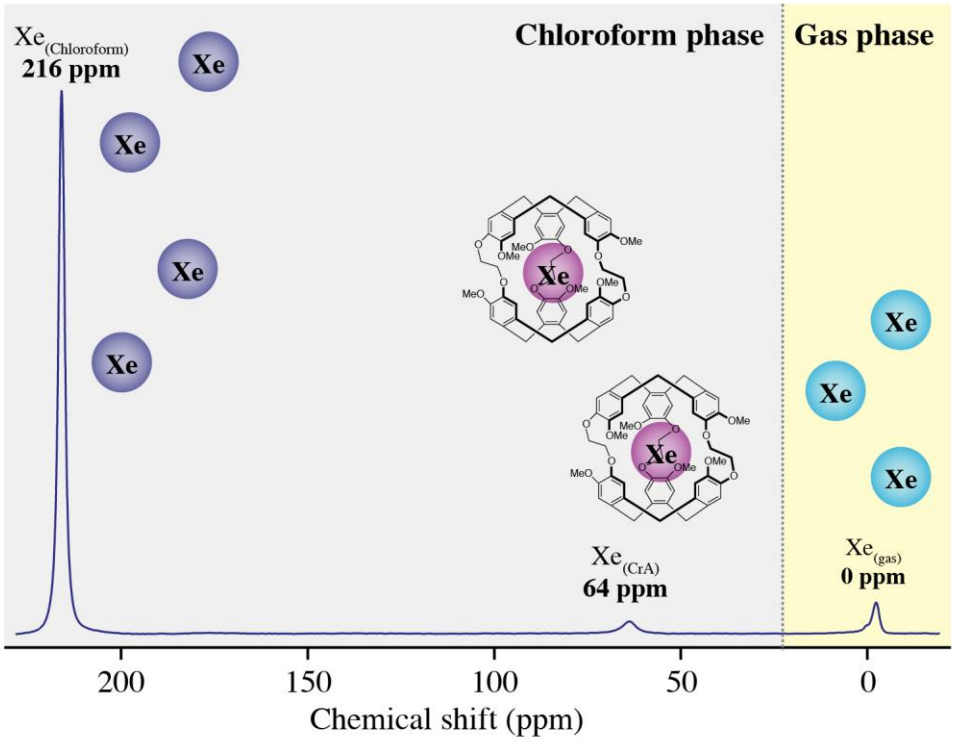

Figure 4.8 Hp ^{129}Xe spectrum of 13 mM CrA in chloroform ($CDCl_3$). A hard pulse (63 µs, 3 dB) has been used to acquire 64 averages during the bubbling of hp gas. The FID was multiplied by an exponential weighted function (lb = 30) before Fourier transformed.

Once the full synthesis of the three parts of the molecules, i.e. CrA, GdDOTA and the linker; and tethering of the GdDOTA to the CrA have been accomplished successfully, spectra were acquired and relaxation rates measured. Longitudinal relaxation rates T_1 were measured as a function of the concentration of the CrA-GdDOTA and its derivatives, [Rx].

As showed in Figure 4.9, when hp ^{129}Xe is bubbled in the solution, the ^{129}Xe exchanges from the gas compartment to the dissolved compartment (H_2O/ACN solvent), but also gets encapsulated in the CrA cage. The encapsulation of the ^{129}Xe in the CrA cages prolongs the ^{129}Xe's presence in close proximity to the paramagnetic chelated Gd^{3+} and induces a fast decay of the $^{129}Xe_{(sol)}$ NMR signal.

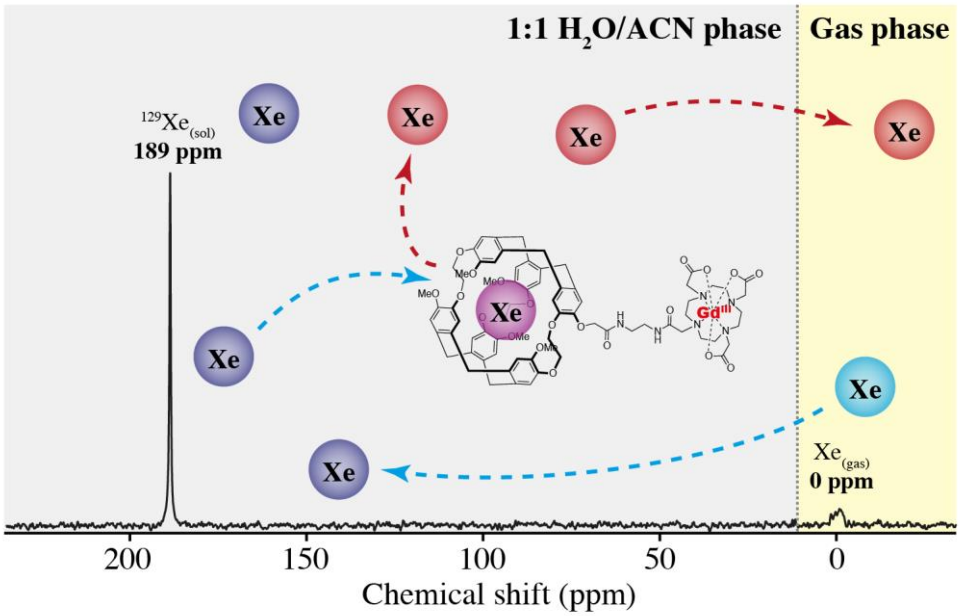

Figure 4.9 Hp ^{129}Xe spectrum of 0.035 mM CrA-GdDOTA in 1:1 H_2O/ACN. Signal from the ^{129}Xe encapsulated in Cryptophane A is not visible due to important line broadening. The FID was multiplied by an exponential weighted function (lb = 30) before Fourier transformed.

The dissolved phase chemical shift, $\delta_{Xe(sol)}$, is varying with the concentration of the different CrA-GdDOTA derivatives. Figure 4.10 shows an illustration of the chemical shift dependency on the concentration of the molecules [Rx]. Only GdDOTA and CrA-GdDOTA allowed linear fitting. GdDOTA and CrA-GdDOTA have a chemical shift dependence of $\delta_{Xe(sol)} = 1.3 \pm 0.1 ppm.mM^{-1}$ and $\delta_{Xe(sol)} = 3.5 \pm 0.4 ppm.mM^{-1}$ respectively. A large variation of the concentration will only induce a small change in chemical shift. The small chemical shift range does not appear to be useful as a sensor of the different molecules concentrations.

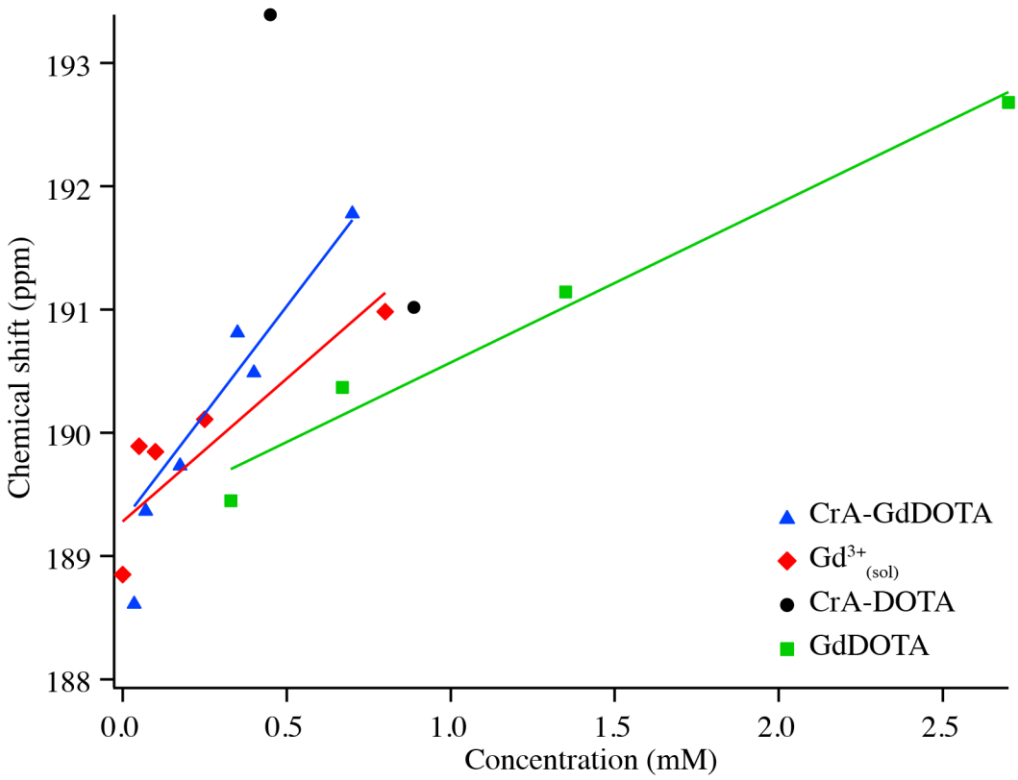

Figure 4.10 Chemical shift dependency on the concentration of CrA-GdDOTA (blue triangles), $Gd^{3+}_{(sol)}$ (red diamonds), CrA-DOTA (black circles), GdDOTA (green squares) dissolved in 1:1 H_2O/ACN. Note that the $Gd^{3+}_{(sol)}$ has also been fitted in red with a dependency of $2.3 \pm 0.5 ppm.mM^{-1}$.

4.4.1. T_1 characterization of the compound and its derivatives

The solubility of hyperpolarized ^{129}Xe gas in solvents allows for a quick dissolved signal build up after the start of bubbling at 40 mL/min. The signal typically reached a saturated plateau after 40 s. The dissolved ^{129}Xe will and continuously exchange with the CrA cages where it is temporarily encapsulated. The ^{129}Xe's temporary confinement in the cages causes it to remain in close proximity of the paramagnetic GdDOTA for the duration of the encapsulation. During this time period, ^{129}Xe experiences very fast paramagnetic relaxation leading to accelerated hp ^{129}Xe depolarization. The continuous chemical exchange between the cages and the solvent will transfer the depolarized atoms to the dissolved phase where the effect is measured by an increase in the relaxation (or depolarization) rate.

As explained in Section 4.3.3., a low flip angle series of RF pulses has been used to characterise T_1. The signal from the dissolved phase, at 190 ppm, is

integrated, and the T_1 value is calculated from the natural logarithm of the normalised integrated signal.

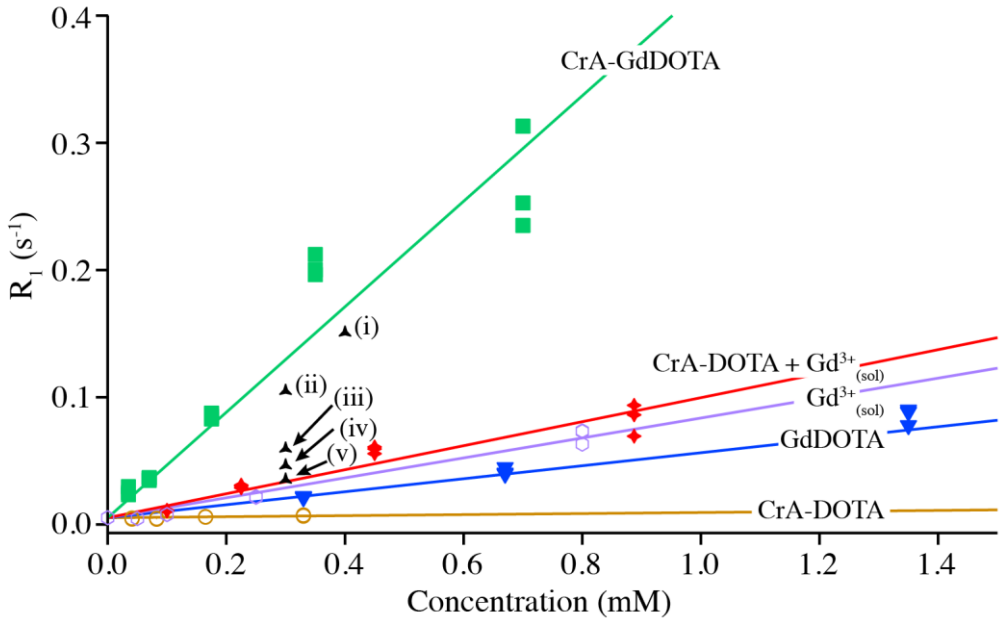

Figure 4.11 Relaxation rates of the dissolved phase ^{129}Xe in different concentrations of CrA-GdDOTA (green squares), CrA-DOTA + Gd^{3+} (red diamonds), Gd^{3+} (purple circles), GdDOTA (blue triangles), and CrA-DOTA (yellow circles). All the compounds are dissolved in a 1:1 H_2O/ACN solution. (i)-(v) represent the time course of CrA-GdDOTA before and after addition of HCl. (i) shows the 0.4 mM CrA-GdDOTA start point before acidification (n=3), (ii) the start point after acidification and dilution to 0.3 mM (n=7), (iii) after 20 h (n=10), (iv) after 24 h (n=4), and (v) after 96 h (n=6).

	Concentration (mM)	*#1 T_1 (s)*	*#2 T_1 (s)*	*#3 T_1 (s)*
CrA-GdDOTA	0.035	33.673	42.708	39.721
	0.07	28.878	27.149	27.522
	0.175	12.059	11.775	11.423
	0.35	4.9935	5.0901	4.7121
	0.7	4.255	3.194	3.9558
CrA-DOTA + Gd^{3+}	0.1	89.387	91.688	95.341
	0.225	34.737	32.305	33.085
	0.5	17.979	16.835	16.399
	0.8875	14.405	11.61	10.675
CrA-DOTA	0.041	205	197.48	233.85
	0.0825	217.03	207.84	239.14
	0.165	161.4	163.63	174.41
	0.33	144.03	132.86	153.92
GdDOTA	0.33	46.899	45.218	46.768
	0.67	24.703	22.327	25.222
	1.35	12.839	11.311	11.105
	2.7	7.292	7.1942	7.3708
Gd^{3+}	0	191.39	190.03	185.01
	0.05	214.89	217.84	214.39
	0.1	126.62	129.93	127.98
	0.25	46.476	46.92	45.652
	0.8	13.675	13.578	15.831

Table 4.1 T_1 individual data for different concentrations of all biosensor derivatives. 3 repeats #1, #2 and #3 have been acquired at each biosensor concentration.

The longitudinal relaxation T_1 has been recorded 3 times for each concentration of each derivative of the CrA-GdDOTA molecule, dissolved in 1:1 H_2O/ACN. These values are displayed in Table 4.1. $^{129}Xe_{(sol)}$ relaxation rates $R_1 = 1/T_1$ have been measured and plotted as a function of the concentration in Figure 4.11 and summarized in Table 4.2.

The relaxivity of GdDOTA for $^{129}Xe_{(sol)}$ was $R_1 = 0.0515 \pm 0.0014 s^{-1}.mM^{-1}$. This value means that a high concentration of GdDOTA would induce only a minor acceleration in the ^{129}Xe relaxation *in vivo*. Indeed, a 1 mM of GdDOTA shows a T_1 for ^{129}Xe of $T_1 = 19s$, that will have a very little effect if injected *in vivo* where ^{129}Xe T_1 in the whole lung is of the order of 20 s (23).

The synthesis precursor CrA-DOTA, free of Gd^{3+} had a relaxivity for ^{129}Xe of $R_1 = 0.00725 \pm 0.0007 s^{-1}.mM^{-1}$ (Table 4.2). This very low relaxivity is explained by the absence of paramagnetic gadolinium. This control experiment demonstrates the very small relaxation induced by the CrA cage itself on the hp ^{129}Xe.

Once Gd^{3+} has been introduced to the system and chelated with the DOTA, the relaxivity of CrA-GdDOTA for $^{129}Xe_{(sol)}$ was recorded to be $R_1 = 0.416 \pm 0.023 s^{-1}mM^{-1}$. This eightfold relaxivity increase as compared to CrA-DOTA can be explained by the encapsulation of $^{129}Xe_{(sol)}$ in the cryptophane cages, placing the hyperpolarized atoms in the immediate proximity of the paramagnetic GdDOTA. Paramagnetic relaxation follows an r^6 dependence (24), where r is the distance between the nuclear spin (encapsulated ^{129}Xe) and the paramagnetic centre. The chemical exchange transfers the relaxation effect from the encapsulated ^{129}Xe to the dissolved phase, leading to an acceleration of R_1 rates for the dissolved $^{129}Xe_{(sol)}$.

The relaxivity of GdDOTA and CrA-GdDOTA for H_2O protons is 150 times higher than that of ^{129}Xe (see Table 4.2), explained by proton's highest gyromagnetic ratio and the γ^2 dependence of paramagnetic relaxation. In addition, the paramagnetic relaxation will be more efficient on water's proton as they will directly coordinate with the Gd^{3+} centre in the GdDOTA chelates (23, 24).

	$^{129}Xe\ R_1\ (s^{-1}.mM^{-1})$	$^{1}H\ R_1\ (s^{-1}.mM^{-1})$	$^{129}Xe\ \delta\ (ppm.mM^{-1})$
GdDOTA	0.0515 ± 0.0014	7.66 ± 0.17	1.3 ± 0.1
CrA-GdDOTA	0.416 ± 0.023	7.36 ± 0.11	3.5 ± 0.4
CrA-DOTA + $Gd^{3+}_{(sol)}$	0.0955 ± 0.0051	15.0 ± 0.14	-
$Gd^{3+}_{(sol)}$	0.0847 ± 0.0029	23.4 ± 0.4	2.3 ± 0.5
CrA-DOTA	0.00725 ± 0.0007	-	-

Table 4.2 ^{129}Xe and ^{1}H relaxation rates, R_1, and chemical shift variation, δ, of the CrA-GdDOTA compound and its derivatives.

To demonstrate the deactivation of the sensor's paramagnetic effect on hp ^{129}Xe, a few drops (0.66 mL) of concentrated HCl (37 % v/v) were added to a 0.4 mM CrA-GdDOTA solution, giving a finale concentration of 0.3 mM. The change in pH causes a protonation of the DOTA and the Gd^{3+} to dislodge from the chelator, reducing the ^{129}Xe presence time in the close vicinity of the paramagnetic agent. Relaxation measurements have been acquired before addition of HCl, and at different times after addition of the HCl.

A time-course of this experiment is represented in Figure 4.12 and Table 4.3, illustrating the relaxivity changes during the acidification and the leach of Gd^{3+} from the molecule. The immediate dilution when adding HCl provokes a large increase of T_1 and a decrease of R_1. The acidification process led to a 3-fold decrease in the relaxivity in 96 hours. Figure 4.12 shows the relaxivity decrease from the CrA-GdDOTA $R_1 = 0.416 \pm 0.023 s^{-1}.mM^{-1}$ to the CrA-DOTA + $Gd^{3+}_{(sol)}$ $R_1 = 0.0955 \pm 0.0051 s^{-1}.mM^{-1}$ during the acidification time course. This 4.3-fold drop in the relaxivity is found to be 2 times greater than the one found for GdDOTA ($R_1 = 0.0515 s^{-1}.mM^{-1}$). This is likely to be caused by the increased contact with the unchelated paramagnetic $Gd^{3+}_{(sol)}$, as a similar effect is observed for ^{1}H relaxivity (Table 4.2).

In an additional experiment, the relaxivity of $Gd^{3+}_{(sol)}$ for ^{129}Xe was found to be $R_1 = 0.0847 \pm 0.0029 s^{-1}.mM^{-1}$ (Table 4.2), close to the relaxivity obtained 96 hours after acidification of the CrA-GdDOTA solution (pH = 0) and complete extraction of the Gd^{3+} out of the DOTA chelator.

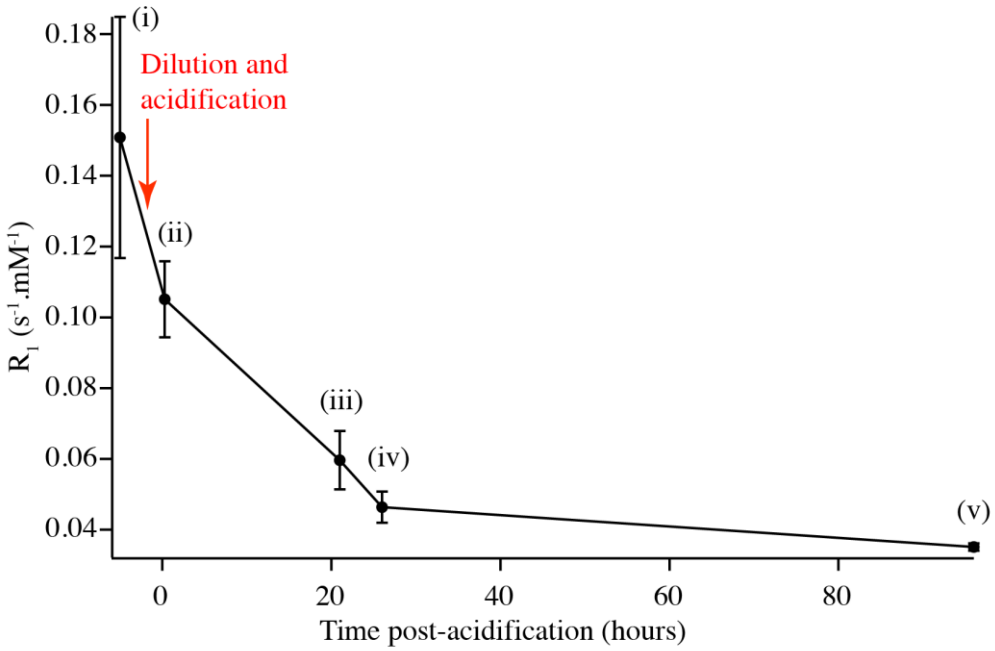

Figure 4.12 CrA-GdDOTA relaxivity before and after adding concentrated HCl to the 1:1 H_2O/ACN solution. (i) shows the relaxivity of a 0.4 mM CrA-GdDOTA solution. The acidification induces the dilution of the solution to 0.3 mM (ii) and the conversion of CrA-GdDOTA into CrA-DOTA + $Gd^{3+}_{(sol)}$. Relaxivities of the conversion process have been acquired 20 h (iii), 24 h (iv) and 96 h (v) after HCl addition to the solution. Note that the data are also represented in Figure 4.11 (black triangles).

Time (h)	***T_1 ± st dev. (s)***	***R_1 ± st dev. (s^{-1})***
Before HCl	6.63 ± 1.46	0.150798 ± 0.034085
0.3	9.51 ± 1.02	0.105106 ± 0.010737
21	16.77 ± 2.06	0.059623 ± 0.008251
26	21.55 ± 1.90	0.046404 ± 0.004410
96	28.45 ± 0.83	0.035150 ± 0.001047

Table 4.3 $^{129}Xe_{(sol)}$ relaxation data for the time-course experiment.

HPLC has been performed on the sampled 20 min, 24 hours and 96 hours after acidification. The chromatograms displayed in Figure 4.13. show the front solvent detection in the early times (peaks before 5 min), the CrA-DOTA peak at 17.2 min, and the CrA-GdDOTA peak at 18.4 min. Integrals of these two peaks are shown in Table 4.4. The chromatogram 20 min after acidification only shows a CrA-GdDOTA peak, illustrating the start point of the experiment, before the Gd^{3+} leaches out of the DOTA. At 24 hours, the second peak for CrA-DOTA appears, confirming a mixture of 13.9 % CrA-DOTA and 86.1 % CrA-GdDOTA. Indeed, the protonation of the DOTA induces the escape of the Gd^{3+} out of the DOTA. Finally, only the CrA-DOTA peak appears at 96 hours, demonstrating the reaction completion and the full leakage of the Gd^{3+} out of the DOTA.

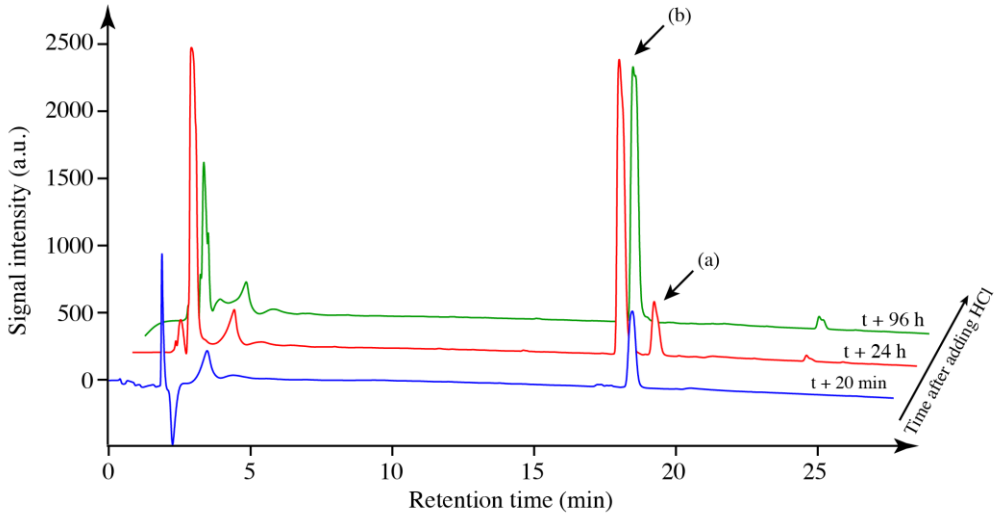

Figure 4.13 Time-course HPLC of the 0.3 mM CrA-GdDOTA in 1:1 H_2O/ACN solution 20 min (blue), 24 h (red) and 96 h (green) after adding concentrated HCl. The CrA-GdDOTA peak (a) appears at 18.4 min of retention time. The CrA-DOTA peak (b) appears at 17.2 min from the 24 h chromatogram in red.

	(a) area (a.u.)	*(b) area (a.u.)*	*%(a)*	*%(b)*
t = 20 min	9443.75	533.04	94.7	0.0
t = 24 h	6210.44	3.85×10^4	13.9	86.1
t = 96 h	-	3.38×10^4	0.0	95.8

Table 4.4 HPLC data. Integration of the indicated peaks in Figure 4.13. (a) refers to the CrA-GdDOTA peak at 18.4 min. (b) refers to the CrA-DOTA peak at 17.2 min. Note that the purity at t = 96 h has been calculated by taking the ratio of peak (b) divided by (b) + impurities peak at 23.8 min.

4.5. Conclusions

The relaxation behaviours obtained in this work show an important increase in the relaxivity of GdDOTA for ^{129}Xe when the chelate is linked to a cryptophane cage. The cage prolongs the presence of the hp ^{129}Xe close to the paramagnetic centre, inducing its depolarization (Figure 4.14). Results showed a 59 % decrease in relaxivity when the chelate does not include the paramagnetic Gd^{3+}. Although the paramagnetic relaxation occurs when the ^{129}Xe is in the cryptophane cage, when the NMR signal appears at about 64 ppm, it is then transferred to the solvent phase at 189 ppm through chemical exchange. The dissolved phase ^{129}Xe relaxation rate will therefore be a weighted average of the solvent phase and the cage phase relaxation rates.

Unlike HyperCEST, this technique does not require radiofrequency irradiation for saturation to accomplish depolarization. The depolarization occurs consequently to the hyperpolarized nuclei's encapsulation, followed by chemical exchange with the dissolved phase, leading to the fast decay of the dissolved phase signal.

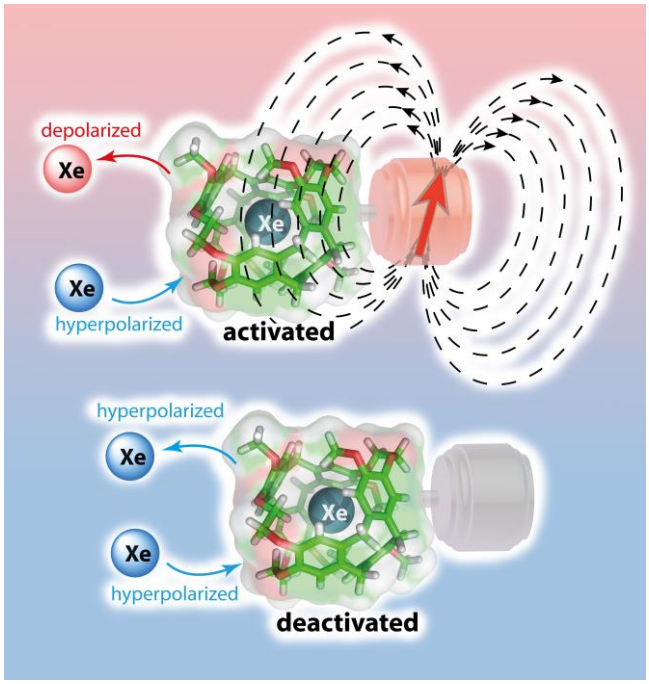

Figure 4.14 Paramagnetic relaxation of the encapsulated ^{129}Xe induced by the activated biosensor (top). No relaxation induced by deactivated biosensor (bottom).

A cleavable linker would functionalize the separation of the cage from the paramagnetic gadolinium that, in turn, would deactivate this relaxation mechanism. In this work, this process has been illustrated by an acidification of the GdDOTA inducing the leakage of the Gd out of the DOTA chelator, deactivating the paramagnetic effect of the complex on the encapsulated ^{129}Xe, and decreasing the relaxation mechanism. This property can be used to gauge enzymatic reactions, and will necessitate a different linker that will be targeted by an enzyme to be cleaved. Matrix metallopeptidase 9 (MMP-9) is a collagenase involved in the degradation of the extracellular matrix and in the lung remodelling. This enzyme is implicated in numerous pulmonary pathologies such as cancer but also IPF and COPD (25). The replacement of the linker by a MMP-9 target peptide will allow the cleavage of the cryptophane cage from the depolarizing GdDOTA where the enzyme is present in the organ. In this future application, the uncleaved biosensor will induce a fast relaxation of the dissolved ^{129}Xe when MMP-9 is absent, therefore producing a positive contrast where the enzyme is present and cleaves the biosensor, preserving the ^{129}Xe magnetization.

After *in vitro* experiments assessing whether the switchable biosensor can quantify the amount of enzyme in the medium, the biosensor can be directly

injected to excised rat lungs via the blood. This method can help gauging the enzymatic composition changes in animal models of lung diseases. The molecule could also be directed to the lung cavity in the form of droplets using a nebulizer or in the form of a powder with a simple inhaler. The deposition of the biosensor in the alveoli could permit a non-invasive evaluation of the enzymatic activity in the airway surface liquid and mucus.

This switchable biosensor is ^{129}Xe specific and does not show any change in ^{1}H relaxation. The paramagnetic relaxation on ^{1}H would allow probing the biosensor location and concentration, independently of the activation state. The ^{129}Xe relaxation is however necessary to differentiate activated and deactivated biosensors with similar relaxation behaviour. Even though a chemical shift change had already been observed using an enzymatic cleavage of a hp ^{129}Xe biosensor (26), this chemical exchange relaxation transfer contrast will not require a high spectral resolution and might be of interest to design new biosensors for *in vivo* application.

4.6. References

1. Driehuys B, Cofer GP, Pollaro J, Mackel JB, Hedlund LW, Johnson GA. Imaging alveolar-capillary gas transfer using hyperpolarized Xe-129 MRI. Proceedings of the National Academy of Sciences of the United States of America. 2006;103(48):18278-83.
2. Berthault P, Huber G, Desvaux H. Biosensing using laser-polarized xenon NMR/MRI. Progress in Nuclear Magnetic Resonance Spectroscopy. 2009;55(1):35-60.
3. Taratula O, Dmochowski IJ. Functionalized Xe-129 contrast agents for magnetic resonance imaging. Current Opinion in Chemical Biology. 2010;14(1):97-104.
4. Couch M, Blasiak B, Tomanek B, Ouriadov AV, Fox MS, Dowhos K, et al. Hyperpolarized and Inert Gas MRI: The Future. Mol Imaging Biol. 2015;17(2):149-62.
5. Strimbu K, Tavel JA. What are biomarkers? Current Opinion in Hiv and Aids. 2010;5(6):463-6.

6. Spence MM, Rubin SM, Dimitrov IE, Ruiz EJ, Wemmer DE, Pines A, et al. Functionalized xenon as a biosensor. Proceedings of the National Academy of Sciences of the United States of America. 2001;98(19):10654-7.
7. Spence MM, Ruiz EJ, Rubin SM, Lowery TJ, Winssinger N, Schultz PG, et al. Development of a functionalized xenon biosensor. J Am Chem Soc. 2004;126(46):15287-94.
8. Schroder L, Lowery TJ, Hilty C, Wemmer DE, Pines A. Molecular imaging using a targeted magnetic resonance hyperpolarized biosensor. Science. 2006;314(5798):446-9.
9. Mecozzi S, Rebek JJ. The 55 % Solution: A Formula for Molecular Recognition in the Liquid State. Chemistry – A European Journal. 1998;4(6):1016-22.
10. Huber G, Brotin T, Dubois L, Desvaux H, Dutasta JP, Berthault P. Water soluble cryptophanes showing unprecedented affinity for xenon: Candidates as NMR-based biosensors. J Am Chem Soc. 2006;128(18):6239-46.
11. Stevens TK, Palaniappan KK, Ramirez RM, Francis MB, Wemmer DE, Pines A. HyperCEST detection of a 129Xe-based contrast agent composed of cryptophane-A molecular cages on a bacteriophage scaffold. Magn Reson Med. 2013;69(5):1245-52.
12. Zaiss M, Schnurr M, Bachert P. Analytical solution for the depolarization of hyperpolarized nuclei by chemical exchange saturation transfer between free and encapsulated xenon (HyperCEST). The Journal of Chemical Physics. 2012;136(14):144106.
13. Witte C, Martos V, Rose HM, Reinke S, Klippel S, Schröder L, et al. Live cell MRI with Xenon Hyper-CEST Biosensors Targeted to Metabolically Labeled Cell Surface Glycans. Angewandte Chemie International Edition. 2015;54(9):2806-10.
14. Zhang J, Campbell RE, Ting AY, Tsien RY. Creating new fluorescent probes for cell biology. Nature reviews Molecular cell biology. 2002;3(12):906-18.
15. Zamberlan F, Lesbats C, Rogers NJ, Krupa JL, Pavlovskaya GE, Thomas NR, et al. Molecular Sensing with Hyperpolarized Xe-129 Using

Switchable Chemical Exchange Relaxation Transfer. ChemPhysChem. 2015;16(11):2294-8.

16. Boutin C, Stopin A, Lenda F, Brotin T, Dutasta J-P, Jamin N, et al. Cell uptake of a biosensor detected by hyperpolarized Xe-129 NMR: The transferrin case. Bioorganic & Medicinal Chemistry. 2011;19(13):4135-43.

17. Six JS, Hughes-Riley T, Stupic KF, Pavlovskaya GE, Meersmann T. Pathway to cryogen free production of hyperpolarized krypton-83 and xenon-129. Plos One (in press). 2012.

18. Gao JH, Lemen L, Xiong JH, Patyal B, Fox PT. Magnetization and diffusion effects in NMR imaging of hyperpolarized substances. Magn Reson Med. 1997;37(1):153-8.

19. Stupic KF, Elkins ND, Pavlovskaya GE, Repine JE, Meersmann T. Effects of pulmonary inhalation on hyperpolarized krypton-83 magnetic resonance T-1 relaxation. Phys Med Biol. 2011;56(13):3731-48.

20. Zhao L, Mulkern R, Tseng CH, Williamson D, Patz S, Kraft R, et al. Gradient-echo imaging considerations for hyperpolarized Xe-129 MR. Journal of Magnetic Resonance Series B. 1996;113(2):179-83.

21. Fulmer GR, Miller AJM, Sherden NH, Gottlieb HE, Nudelman A, Stoltz BM, et al. NMR Chemical Shifts of Trace Impurities: Common Laboratory Solvents, Organics, and Gases in Deuterated Solvents Relevant to the Organometallic Chemist. Organometallics. 2010;29(9):2176-9.

22. Gottlieb HE, Kotlyar V, Nudelman A. NMR chemical shifts of common laboratory solvents as trace impurities. J Org Chem. 1997;62(21):7512-5.

23. Mugler JP, Altes TA. Hyperpolarized 129Xe MRI of the human lung. Journal of Magnetic Resonance Imaging. 2013;37(2):313-31.

24. Abragam A. The Principles of Nuclear Magnetism. Oxford, UK: Oxford University Press; 1961.

25. Atkinson JJ, Senior RM. Matrix Metalloproteinase-9 in Lung Remodeling. Am J Respir Cell Mol Biol. 2003;28(1):12-24.

26. Wei Q, Seward GK, Hill PA, Patton B, Dimitrov IE, Kuzma NN, et al. Designing Xe-129 NMR biosensors for matrix metalloproteinase detection. J Am Chem Soc. 2006;128(40):13274-83.

CHAPTER 5

FLUORINATED SYNTHETIC BLOOD AS A CONTRAST AGENT FOR ^{129}XE NMR OF *EX VIVO* RAT LUNGS

The preliminary results presented in this chapter are based on experiments that were developed by Prof. Thomas Meersmann and Clémentine Lesbats.

In vitro and *ex vivo* spectroscopy measurements were performed by Clémentine Lesbats. The animal preparation and lungs harvesting was performed by Clémentine Lesbats, and Anthony Habgood when using the animal model of pulmonary fibrosis. The recompression unit that allowed for the delivery of hyperpolarized gas to the excised lungs was built and semi-automated by Zahra Rahemtulla, during the course of her M.Sc. The pulse sequences were written by Clémentine Lesbats, supervised by Dr. Galina E. Pavlovskaya and Prof. Thomas Meersmann. Data analysis was carried out by Clémentine Lesbats.

5.1. Introduction

Idiopathic Pulmonary Fibrosis (IPF) is a chronic, progressive interstitial lung disease associated with severe morbidity. At present the aetiology of IPF is unknown, there are no effective means for monitoring disease progression and no treatments available. Whilst structural imaging is useful for diagnostic purposes, and conventional pulmonary function testing gives reliable global assessments of lung function, functional imaging would represent a significant step forward in assessing and monitoring novel therapeutics.

The solubility of ^{129}Xe in lung tissue, and blood plasma, makes hp ^{129}Xe particularly promising for imaging of lung fibrosis (1). The tissue solubility of ^{129}Xe enables regional monitoring of gas-blood exchange in IPF providing a significant advantage over current technology (2, 3).

Due to its large compressible outer electron shell, ^{129}Xe has been shown to exhibit an observable chemical shift between the gas and dissolved phase (4). Furthermore, there are differences in the resonance frequency when ^{129}Xe is bound to a variety of molecules, including haemoglobin (5, 6). This unique property has allowed imaging of hp ^{129}Xe dissolved in the lung tissue and pulmonary circulation and imaging of ^{129}Xe moving in the reverse direction, diffusing from the bloodstream into the lung airspaces (7). The large chemical shift (200 ppm) between the ^{129}Xe gas phase and the dissolved phase permits the study of the diffusing capacity in human and rodent lungs (8-12).

One limiting factor in these experiments is the rather poor solubility of ^{129}Xe in plasma and red blood cells (RBCs) with the result that the intensity of the dissolved phase signal in the lungs is a factor of 100 times smaller than the gas phase signal after inhalation of hp ^{129}Xe (13). Methods to increase the concentration of ^{129}Xe in solution have been investigated using various carrier agents and membrane technologies (14-16).

Another limitation is that the NMR peaks associated with the ^{129}Xe in the tissue and in the blood are adjacent –at approximately 200 ppm, and can be difficult to differentiate. It has been shown that ^{129}Xe dissolved in perfluorocarbon emulsion (PFCE) resonates around 100 ppm (14, 17). In this chapter, a PFCE will be explored to enhance the MRI contrast of hp ^{129}Xe diffusing through the lung parenchyma into the vascular system. The addition of PFCE to the blood will facilitate the discrimination of the hp ^{129}Xe dissolved

in the blood stream from the tissue. The purpose is to provide new MRI contrast for the study of pulmonary gas transfer dynamics in health and disease. For example, gas transfer to the blood compartment is reduced in interstitial diseases such as idiopathic pulmonary fibrosis (18, 19).

It has been shown to be less technically demanding and less invasive to prepare hp ^{129}Xe into a solution and then infuse the prepared solution into the animal itself (20, 21). Hollow-fibre membranes used in blood oxygenators have been employed to increase the concentration of dissolved ^{129}Xe both in blood and in solutions (15, 16, 22, 23). Membranes have been used as they greatly reduce the degree of foaming that occurs when the relatively insoluble gas is delivered to solution as only small bubbles diffuse across. *In vivo* imaging is however still limited by the poor solubility of ^{129}Xe in the blood requiring continuous perfusion of hp ^{129}Xe directly into the bloodstream via a gas exchange module (16). This method may be suitable for *in vivo* animal experimentation but is unlikely to find widespread clinical acceptance due to issues with invasiveness and coagulation within the gas exchange device itself. In addition, numerous signal averaging over many breaths is still required for dissolved phase imaging, limiting resolution at present. Biologically "inert" substances that produce little coagulation can avoid the need for delivery of blood products or the extracorporeal circulation of blood. Carrier agents have been investigated, as ^{129}Xe solubility is much higher in lipid and perfluorocarbon based compounds (24).

5.2. Motivation

Excised rodent lung imaging has been validated and used to study excised healthy rodent lungs with hp ^{129}Xe (25) and ^{83}Kr (26), allowing for the imaging of the lungs prior to histological studies. In this research, a bleomycin-induced animal model of pulmonary fibrosis has been used (19). The initial hypothesis is that if a synthetic blood, perfluorocarbon emulsion (PFCE), is added to the blood compartment of excised lungs (Figure 5.1), the dissolved peaks will be better resolved, allowing an enhanced discrimination of the ^{129}Xe signal in the parenchyma and the capillaries.

The objectives of this project are to investigate the solubility of ^{129}Xe in two PFCEs and assess their suitability for use as a contrast agent in *ex vivo* lungs in

order to study the gas diffusion through the pulmonary parenchyma. This will lead to a new non-invasive monitoring of the gas diffusion kinetics parameters in animal models of pulmonary fibrosis. The practicability of the use of synthetic blood as a hp ^{129}Xe contrast agent in excised rat lungs will be evaluated, involving *in vitro* measurements of the ^{129}Xe chemical shift dissolved in the synthetic blood, and longitudinal relaxation measurements, alongside with some *ex vivo* rat lung spectroscopy applications. These results can be used for the exploration of the gas exchange in small animal disease models where the pulmonary gas diffusion is impaired, or the evaluation of pulmonary treatments on the gas transfer.

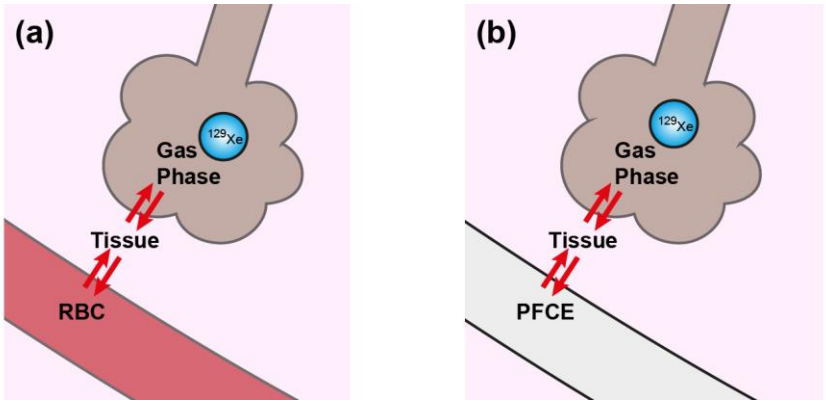

Figure 5.1 Gas diffusion through the lung parenchyma from the alveolar space, through the tissue, to the pulmonary capillaries before (a) and after (b) blood replacement by PFCE.

5.3. Material and methods

5.3.1. *Ex vivo* rat lung MRI protocol

The rat lungs were extracted and were all suitable for hyperpolarized noble gas MR experiments, i.e. they were not damaged nor leaking. Lungs were suspended in a 25 mm or 30 mm ventilation chamber filled with saline solution that was then placed into the magnet, set to 17 °C.

As described in Chapter 2, and similarly to Chapter 3 (Section 3.2.4.), hyperpolarized ^{129}Xe was produced in batch mode spin exchange optical pumping (SEOP). The gas mixture used was composed of 25 % enriched ^{129}Xe (enriched to 83 % ^{129}Xe, Nova Gas Technologies, Charleston, SC, USA) and 75 % N_2 (99.999 % purity, Air Liquide, Coleshill, UK). Low pressure SEOP was performed at 65 – 75 kPa during 6 min. The hp gas mixture was then

delivered to the pre-vacuumed recompression piston (27). The recompression unit was allowing for recompression of the hp gas up to above ambient pressure to permit delivering the gas to the excised lung trachea as described in Section 2.8.

An active inhalation of the hp ^{129}Xe into the excised lungs was accomplished by a ventilation syringe producing a suction in the ventilation chamber (25). The inhalation volume was determined prior to the MR experiments. The lungs were completely inhaled at a fixed volume. The exhaled gas volume was delivered to an inversed measuring cylinder filled with water, and the gas volume was directly measurement by the volume of displaced water. The average inhaled volume in 6 representative rats are listed in Table 5.1.

Rat ID	*Experiment day*	*Weight (g)*	*Inhaled volume (mL)*	*Inhalation pressure (mbar)*	*^{129}Xe NMR and MRI*	*^{83}Kr NMR*
Control 2_2	1	324	4.8 ± 0.1	19 ± 0.9	Yes	No
Bleo 1_1	1	304	4.2 ± 0.4	21 ± 1.5	Yes	Yes
Bleo 1_3	1	302	4.2 ± 0.6	26 ± 0.6	Yes	Yes
Control 2_3	2	330	5.2 ± 0.05	23 ± 2.3	Yes	No
Bleo 3_3	2	307	4.8 ± 0.2	22 ± 1.1	Yes	No
Bleo 3_4	2	302	5.3 ± 0.1	22 ± 0.0	Yes	No

Table 5.1 Demographic data for the emphysematous rat lungs used for ^{129}Xe MRI and NMR, rat weights, inhaled volumes ± standard deviation ($n = 5$), and experiments done with the lungs.

5.3.2. Animal model of pulmonary fibrosis: the bleomycin rat model

Lewis male rat (300-350 g) lungs were used for preliminary investigation on the ^{129}Xe gas transfer through the lung parenchyma in excised fibrotic rat lungs. An *ex vivo* rat model of pulmonary fibrosis was produced by oropharyngeal delivery of bleomycin. Bleomycin is a chemotherapeutic antibiotic well known for its adverse effect of activating fibroblasts and subsequently inducing fibrosis (28). The lungs were excised 21 days after treatment for MR experiment.

A second set of rats was composed of one bleomycin-treated and one control rat received a *post mortem* blood replacement by a perfluorocarbon emulsion as explained in the next section.

5.3.3. Perfluorocarbon emulsion as synthetic blood and ^{129}Xe carrier

Two perfluorocarbon emulsions (PFCE) were used, Oxycyte (Tenax Therapeutics, Inc, Morrisville, USA) and Perftoran (OJSC SPC Perftoran, Moscow, Russia). These two agents were developed to be used as a human blood replacements and oxygen carrier agents (29, 30). In the purpose of this study, they were utilised as ^{129}Xe carrier in the *ex vivo* rat lungs. The synthetic blood was administered *post mortem* to the lungs through the caudal vena cava after flushing of the blood off the heart and lung capillaries. For more detail, the lung extraction and blood replacement were extensively detailed in Section 2.8.

Table 5.2 lists the aims of the three experiments involving rat lungs, the PFCE, and the number of rat that was used for each of them.

Some ^{129}Xe MRI and NMR were first done in some fibrotic and control rat lungs (Stage 1). In a second experiment, ^{129}Xe NMR was evaluated in a treated and a control rat lungs which underwent a blood replacement by Oxycyte (Stage 2).

Finally, for the particularity of the Stage 3 experiment, the original Perftoran 10 % was concentrated by evaporation of the solvent phase. This was achieved using a water bath (RE 300 DB, Stuart equipment, Bibby Scientific Limited, Stone, UK) and a rotary evaporator (RE 300, Stuart equipment, Bibby Scientific Limited, Stone, UK). A 60 mL initial volume of commercial Perftoran, defined by 10 % v/v lipid emulsion, was added, and intermittently warmed up to 313 K bath while rotating in order to preserve the emulsion, with a 50 to 100 mbar vacuum. The final volume was 32 mL, producing a Perftoran solution concentrated to 19.2 % v/v lipid emulsion. This concentrated solution was made to improve the ^{129}Xe signal arising at 90 ppm when dissolved in the lipid emulsion and is used in the latest section of this chapter.

	PFCE	*Aim of the experiment*	*Number of rats*	*MRI*	*NMR*
Stage 1	**N/A**	Comparing the hp ^{129}Xe gas phase MRI and dissolved phase NMR in bleomycin and control Lewis rat lungs	6	Yes	Yes
Stage 2	**Oxycyte**	Comparing the hp ^{129}Xe PFCE signal from a bleomycin and a control Lewis rat lung	2	No	Yes
Stage 3	**Perftoran 19.2 %**	Utilizing two control Sprague-Dawley rats to assess the hp ^{129}Xe gas transfer from the alveoli to the blood compartment containing the PFCE	2	No	Yes

Table 5.2 Experiments overview: PFCE that was used as blood replacement, aim of the experiment, and number of rat used.

5.3.4. ^{129}Xe lung MRI protocol

Imaging experiments were performed using a 9.4 T Bruker Avance III microimaging system (Bruker BioSpin GmbH, Germany). A custom-built 25 mm low-pass birdcage coil tuned to the resonance frequency of ^{129}Xe gas in the rat lung of 110.69 MHz was used for ^{129}Xe gas phase imaging.

Images were acquired using a variable flip angle (VFA) FLASH gradient echo sequence. A sinc shaped pulse of 1000 µs was used to accomplish a 3.8 mm slice selection. The images were acquired in 128 x 64 voxels matrices, and with a field of view (FOV) of 47 x 33 mm in a total acquisition time of 4 s.

5.3.5. ^{129}Xe NMR protocol

Spectroscopy of the *ex vivo* lungs was realised using a 30 mm Bruker-made coil tuned to the ^{129}Xe gas phase (110.69 MHz), tissue (110.715 MHz) or PFCE phase (110.703 MHz) resonance frequency.

A qualitative spectrum was first acquired using a 140 µs hard pulse centred between the gas phase (0 ppm) and the tissue (193 ppm), and a spectral width of $SW = 60\ kHz$ covering all of the ^{129}Xe phases in a rat lung.

A chemical shift selective gauss pulse was also calibrated in order to selectively excite the tissue or the Perftoran phase, with minor excitation of the two other peaks. A 750 µs gauss pulse led to an excitation bandwidth of $BW = 3000\ Hz$.

Chemical shift selective gauss pulses were calibrated to minimize the effect of the excitation on the bulk gas phase (0 ppm) that is used as a reservoir during longer experiments. Figure 5.2 represents three spectra acquired using a single hard pulse centred on the Perftoran phase (grey), compared to 64 averages using a chemical shift selective gauss pulse (750 µs) in a healthy rat lung with blood replacement using Perftoran 19.2 %. The gas phase peak appears smaller when the carrier frequency of the gauss pulse is centred on the tissue phase (red) as compared to the Perftoran phase (blue).

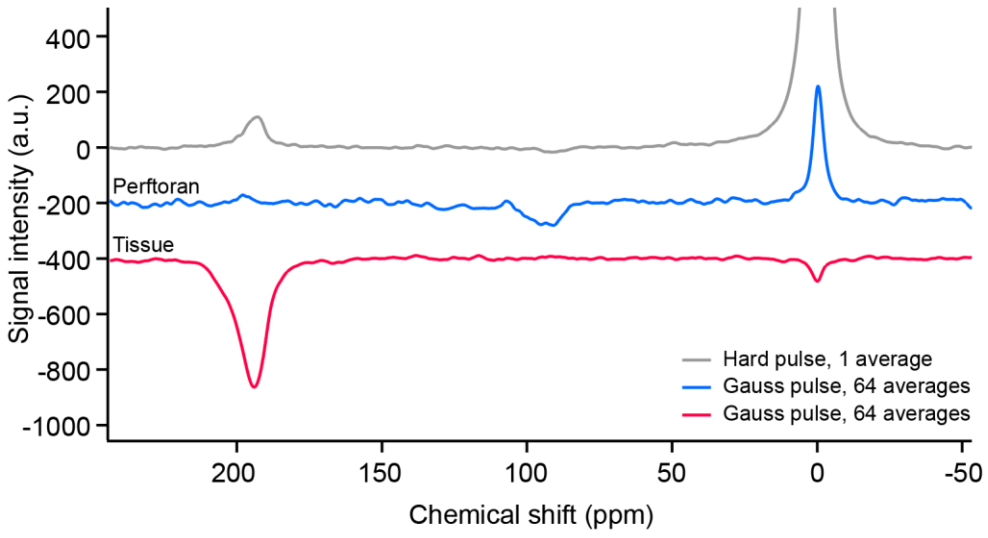

Figure 5.2 Hp ^{129}Xe NMR spectra using a single non-selective hard pulse (grey), or a chemical shift selective gauss pulse (64 averages), centred on the Perftoran phase (blue) or tissue phase (red). Note that the phase was inversed for an easier visualisation.

5.3.6. ^{129}Xe Chemical Shift Saturation Recovery (CSSR)

Dynamic spectroscopy of the ^{129}Xe gas transfer through the parenchyma has been performed using a Chemical Shift Saturation Recovery (CSSR) pulse sequence. The pulse sequence consists in sequentially measuring ^{129}Xe NMR spectra after a selective saturation of the dissolved phase and an increasing exchange time (Figure 5.3). In addition, the saturation pulse was followed by a dephasing gradient (1771.74 Hz/mm, 0.1 ms).

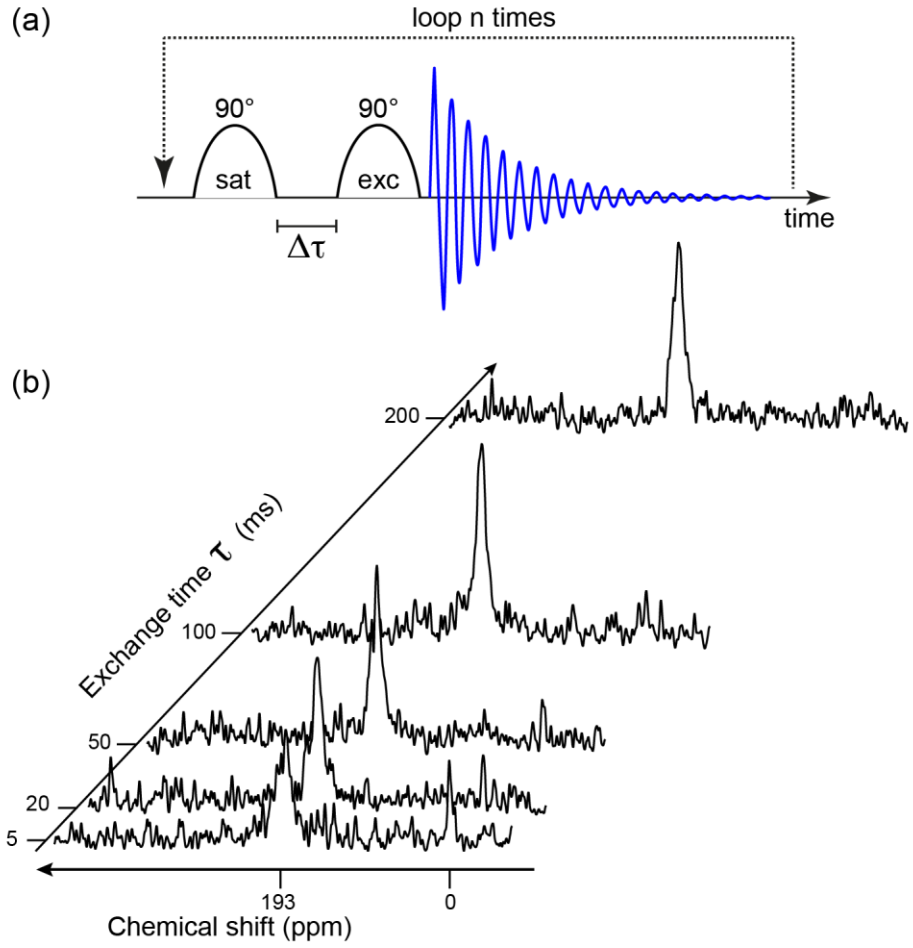

Figure 5.3 (a) Schematics of a chemical shift saturation recovery (CSSR) pulse sequence used in this chapter. The chemical shift selective saturation gauss pulse is followed by an exchange time. A similar chemical shift excitation pulse is employed for signal acquisition. The exchange time is incremented for each new loop. (b) an example of spectra acquired in a single acquisition using the different exchange times in a CSSR sequence, with a tissue phase signal build-up.

5.3.7. ^{83}Kr longitudinal relaxation measurement

In order to evaluate whether the bleomycin instillation induced an alveolar degradation, the ^{83}Kr longitudinal relaxation was measured. A train of 16 small flip angle pulses with an interpulse delay of 1 ms was used. The T_1 relaxation was obtained by linear regression of the natural logarithm of the signal intensity as a function of delay time as explained in Section 2.4.2.

5.3.8. Data analysis

All raw data were processed using Prospa (Magritek, Wellington, New Zealand) and subsequent processing using Igor Pro (Wavemetrics, Lake Oswego, Oregon, USA), followed by figure adjustments using the illustration tool Adobe Illustrator® CS5. A sine-bell squared function was applied in the images k-space both directions and zero filled to 256 x 128 in order to smooth the magnitude images after 2D Fourier transform. NMR raw data were resized to remove the zero-value points present prior to the FID, and an exponential function was applied on them before Fourier transform. Similarly, CSSR matrices were also resized, an exponential function was applied before being Fourier transformed in the direct direction.

5.4. Results and discussion

5.4.1. Preliminary ^{129}Xe MRI and NMR of *ex vivo* fibrotic lungs

The purpose of this first study was to observe the dissolved ^{129}Xe in excised fibrotic lungs (see Stage 1 in Table 5.2). 4 bleomycin-treated and 2 control rats were used, during the course of two days, with 2 bleomycin and 1 control on each day. The excised lungs are the subject of a blood replacement by PBS solution (Sigma-Aldrich Ltd, Gillingham, UK) during the lung dissection. Therefore, we can assume that the sharp peak appearing at 193 ppm in all lungs spectra was arising from the ^{129}Xe dissolved in saline, accompanying the parenchymal tissue phase peak at 195 ppm (see Figure 5.4 for an example).

The Tissue/Total ^{129}Xe ratio was calculated after a single hard pulse spectrum was acquired in the 4 bleomycin rats and 2 control, phase and baseline corrected. Results are listed in Table 5.3. The results are very similar for both control and fibrotic lungs, and do not allow for any correlation between the proportion of the ^{129}Xe dissolved in the lungs and the bleomycin treatment.

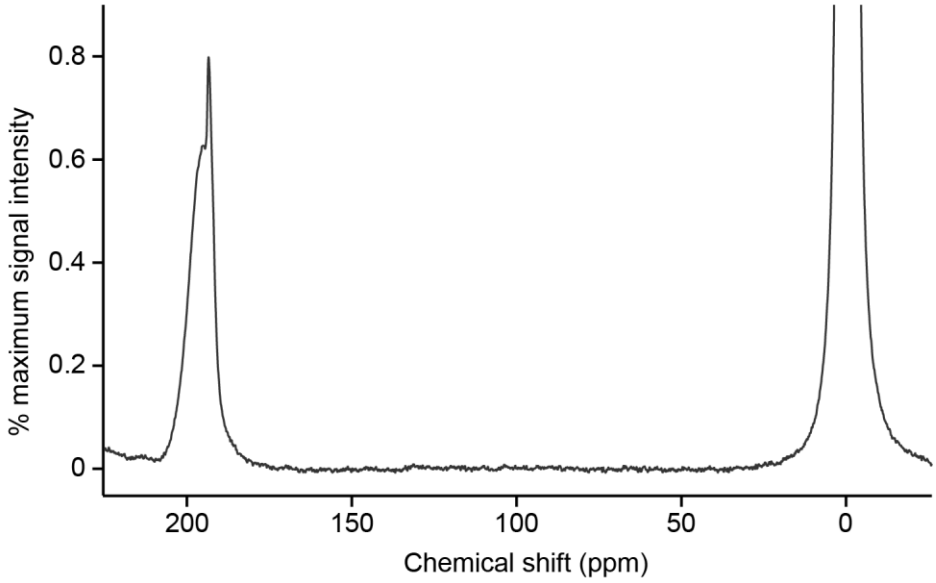

Figure 5.4 Hp ^{129}Xe NMR spectrum in the excised lung Bleo 1_1. The gas phase is set to the conventional 0 ppm and the tissue peak appears at 195 ppm, accompanied by a sharp saline peak at 193 ppm.

	Rat ID	*Tissue/Total ^{129}Xe signal*
Day 1	Control 2_2	3.34 %
	Bleo 1_1	2.70 %
	Bleo 1_3	2.33 %
Day 2	Control 2_3	2.51 %
	Bleo 3_3	2.76 %
	Bleo 3_4	2.73 %

Table 5.3 Proportion of the ^{129}Xe signal arising from the tissue over the total ^{129}Xe signal in the bleomycin-treated lungs and control lungs. One control lung and two bleomycin-treated lungs were studied during two consecutive days. The peaks were integrated after phase correction and baseline correction of the spectra, and the tissue signal ratio was calculated.

A narrower spectral width allowed zooming in on the dissolved peak. Figure 5.5 shows the tissue peak for the 2 control lungs and the 4 fibrotic lungs. Less total signal was observed in both control and fibrotic on the second day due to the SEOP pump cell aging. Spectra were therefore normalised to match similar integral in the control lungs on both days. On days of measurement the control lung showed more signal in the tissue than the two fibrotic lungs. The higher signal in the control lungs on both days can be explained by their 20 – 30 g higher weight. Indeed, the bleomycin instillation induces a weight loss in the treated animal, causing the control rats to be heavier than the rats with the disease model. Finally, a red blood cell peak remains noticeably visible at 213 ppm (see light blue spectrum from the Control lung 2_3 in Figure 5.5), probably due to some very small amount of blood that remained in the heart and pulmonary capillaries.

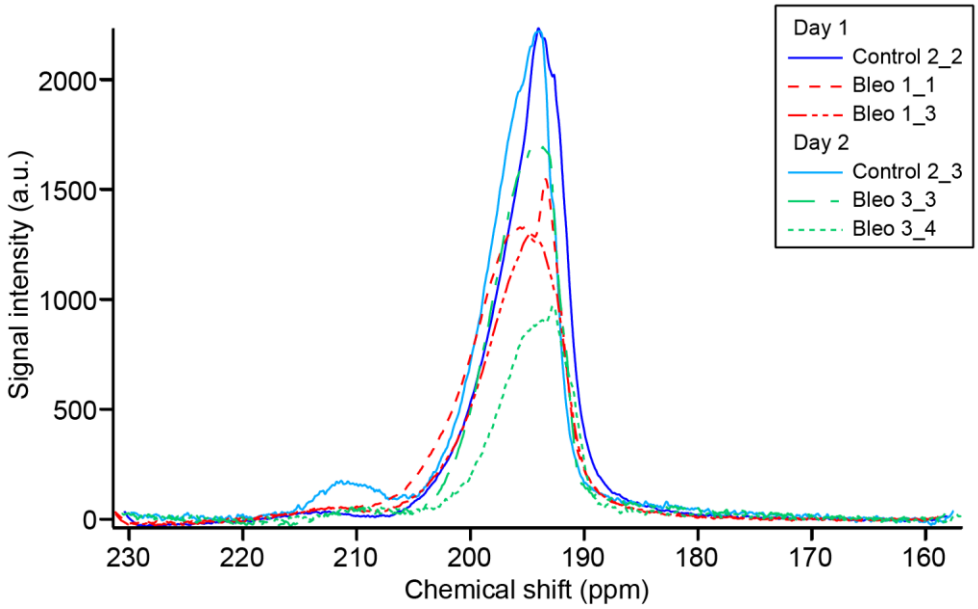

Figure 5.5 Hp ^{129}Xe spectra of the six excised lungs presented in Table 5.1. The control rat lungs are displayed in blue solid lines, the bleomycin-treated rat lungs are presented in dashed and dotted lines. Due to lower signal caused by the SEOP performance, the spectra acquired on the second day were normalised to match the same control spectrum integral (blue spectra).

Hyperpolarized gas phase ^{129}Xe MRI of excised lungs was used to position the lungs in the coil and magnet, prior to the spectroscopy measurements, but also to observe some qualitative characteristics of a bleomycin treatment on excised rat lungs. Slice selective coronal and transverse imaging was done using the VFA FLASH imaging sequence described in Section 5.3.4.

Figure 5.6 and Figure 5.7 present the transverse and coronal images in two representative control and bleomycin lungs respectively. The slice selective transverse images allow for a clear visualisation of the bronchi, brighter than the parenchymal ^{129}Xe signal. The coronal images show the trachea, the division into bronchi, and the different lobes. Numerous ventilation defects are observed in all fibrotic lungs (see also the appendices for all rats MRI). The slice selective coronal images of the fibrotic lung (Figure 5.7, images *vii* and *viii*) depict some ventilation defects mostly located around the main airways on both sides, confirming the disease induction in these animals. The bleomycin-treated lung 1_3 was presenting a collapsed upper left lobe (Appendix, Figure A.5) that might be due to severe fibrosis that weakened the lung structure, but might also have collapsed during the travel or any experimental procedure.

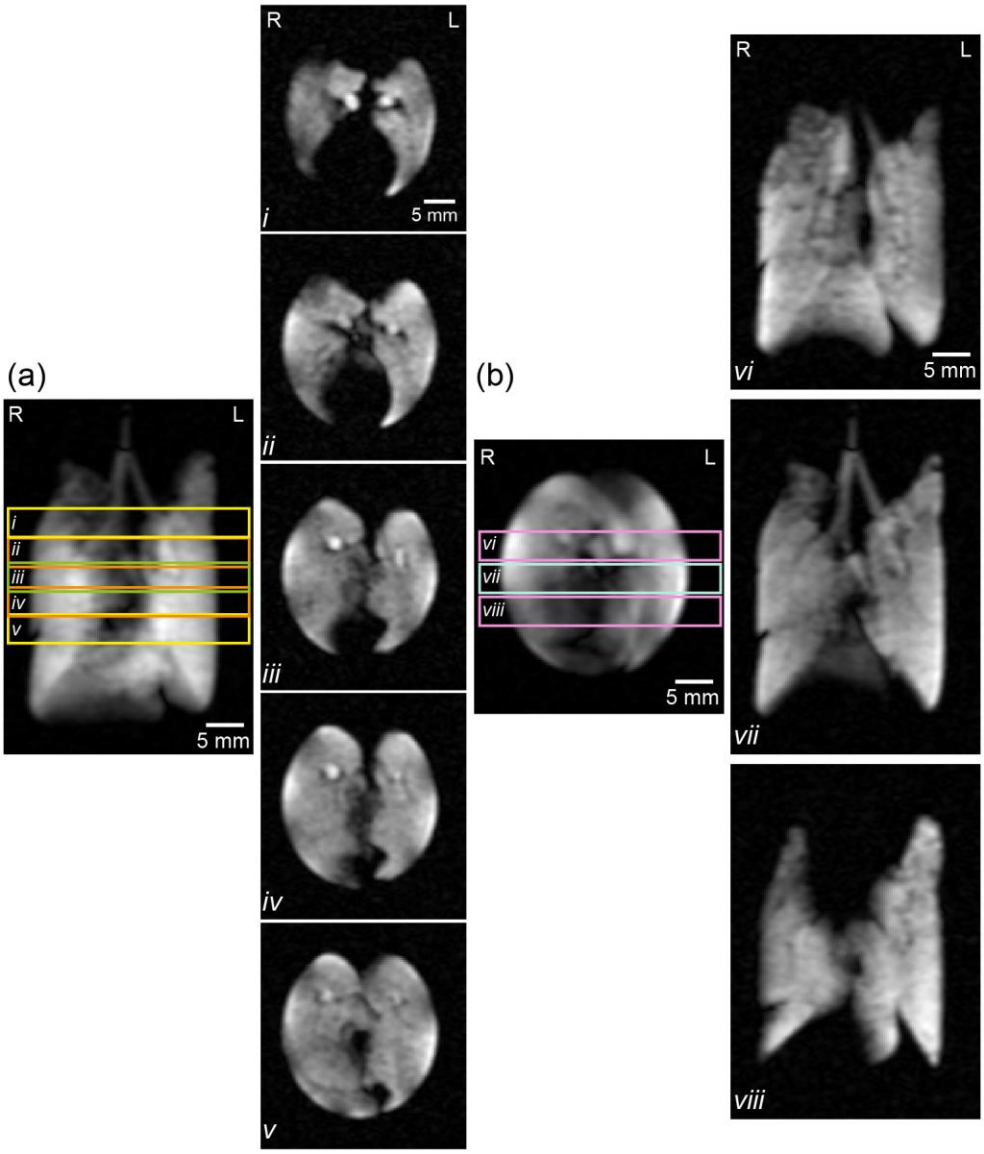

Figure 5.6 Transverse (a) and coronal (b) slice selective VFA FLASH images of the excised Control lung 2_2 accompanied by a non-slice selective image showing the location of the slices.

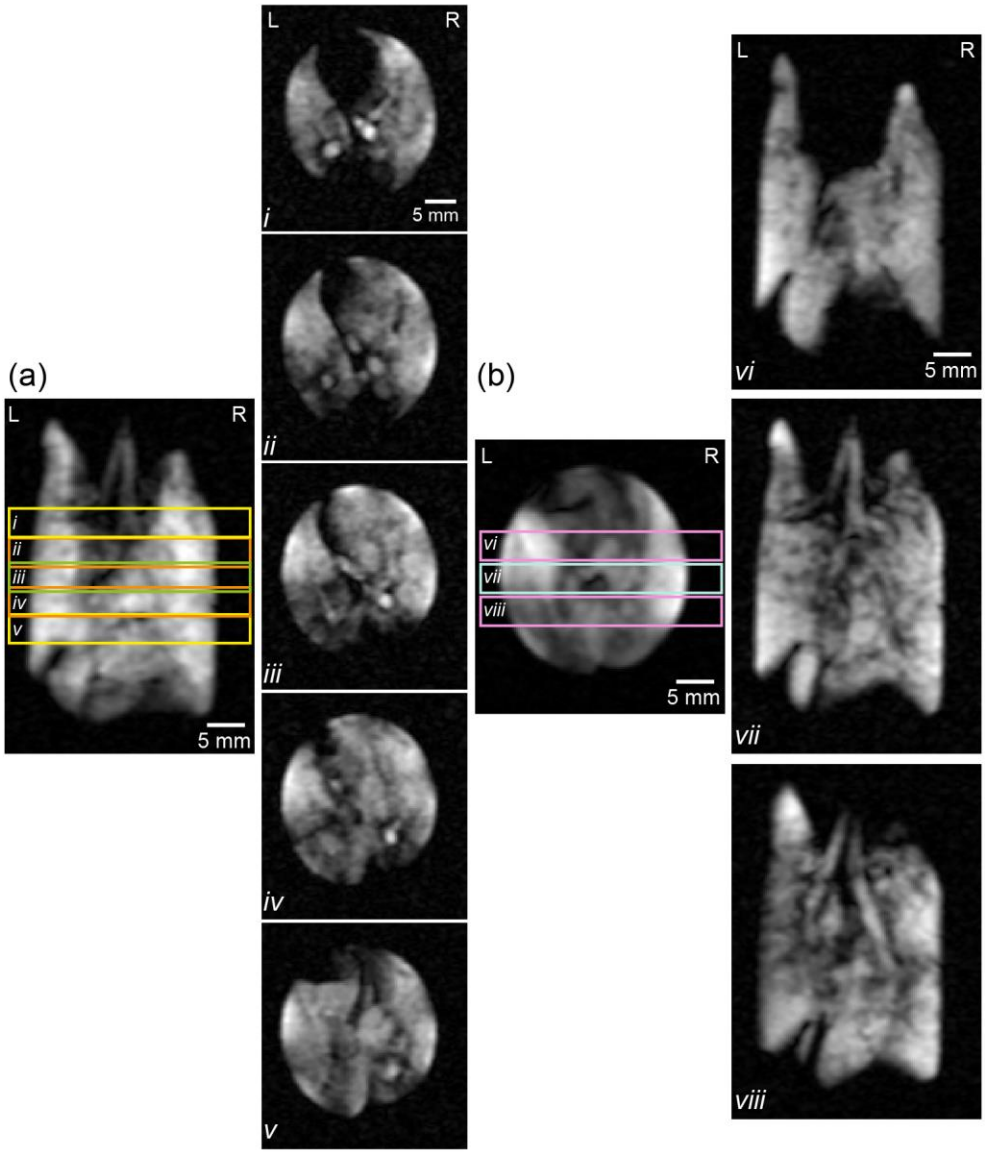

Figure 5.7 Transverse (a) and coronal (b) slice selective VFA FLASH images of the excised Bleo lung 1_1 accompanied by a non-slice selective image showing the location of the slices.

5.4.2. ^{83}Kr NMR of *ex vivo* fibrotic lungs

Whole lung hyperpolarized ^{83}Kr NMR spectroscopy is used to assess whether the whole lung T_1 can be used as a measure for global alveolar impairment. Alveolar degradation not being the main scope of this study, the technically more demanding ^{83}Kr MRI as demonstrated in Chapter 3 was not evaluated on this animal model of fibrotic thickening. It has been shown that fibrotic lungs also show emphysematous damages due to scarring (31). Hp ^{83}Kr T_1 was measured in the two fibrotic Lewis lungs, Bleo 1_1 and Bleo 1_3, without spatial resolution nor specific inhalation scheme. This whole lung longitudinal relaxation measurement was also measured in the emphysematous and control rat lungs used in Chapter 3. The average T_1 for each pathological group is listed in Table 5.4.

	No. of measurements	*Average T_1 ± standard deviation (s)*	*Average weight ± standard deviation (g)*	*Inhaled volume*
Control rats	$n = 5$	1.354 ± 0.101	513 ± 35	6.5 ± 0.6
Elastase-treated rats	$n = 9$	1.401 ± 0.178	453 ± 55	6.9 ± 0.1
Bleo 1_1	$n = 4$	1.255 ± 0.051	304	4.2 ± 0.4
Bleo 1_3	$n = 4$	1.208 ± 0.037	302	4.2 ± 0.6

Table 5.4 ^{83}Kr longitudinal relaxation (T_1) in the control rats and elastase-treated rats from Chapter 3, and in two bleomycin-treated rat lungs.

The whole lung ^{83}Kr T_1 appear to be lower in the bleomycin-treated rat lungs as compared to both elastase-treated and control rat lungs utilised in Chapter 3. This can perhaps be explained by the difference of species in the rats that are used for both animal models. Indeed, the preferred rat species for emphysema are Sprague-Dawley rats while Lewis rats are used for fibrosis models. This difference of species might induce a difference in the alveolar morphology.

In addition, there was an animal weight difference between elastase and bleomycin-treated rats. The bleomycin rats before lung dissection were 303 g on average, which was more than 150 g lower than that of the Sprague-Dawley rats used for the ^{83}Kr study in Chapter 3.

Finally, the inhaled volume in the bleomycin-treated rats was also lower than that of the elastase-treated ones. The reduced alveolar inflation due to a reduced inhalation volume might induce the partial recruitment of some alveoli and could explain the lower T_1 in these lungs (32).

5.4.3. *In vitro* ^{129}Xe NMR of synthetic blood

Hyperpolarized ^{129}Xe was bubbled through the synthetic bloods Oxycyte and commercial Perftoran, containing 10 % v/v lipid emulsion (see Section 5.3.3.). The protocol was the same as used in Chapter 4 (see Section 4.3.2.). The spectra obtained by such protocol allows locating the ^{129}Xe signal dissolved in the perfluorocarbon emulsions.

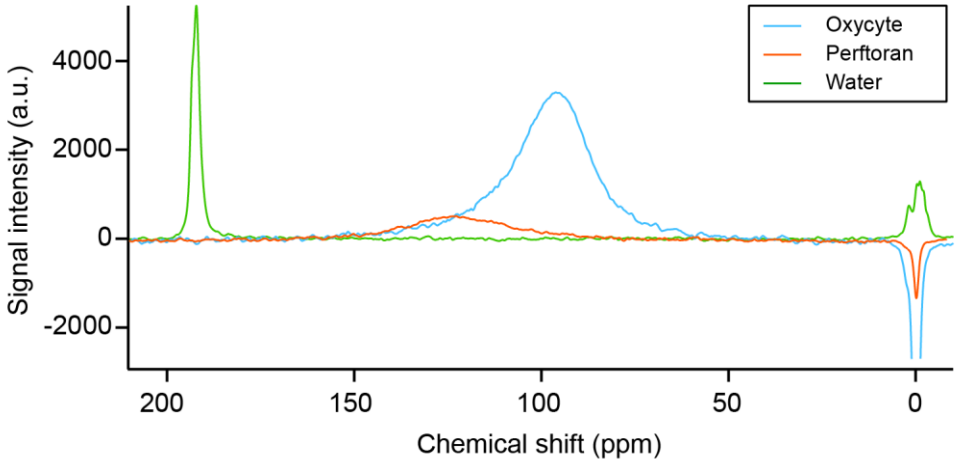

Figure 5.8 ^{129}Xe spectra in three carriers: Oxycyte (blue), Perftoran (orange) and water (green) after bubbling some hp ^{129}Xe through a 2 mL sample for 45 s.

Figure 5.8 displays the *in vitro* ^{129}Xe spectra for Oxycyte and Perftoran. The signal arising from a water sample is also displayed for reference. Hp ^{129}Xe signal from the Oxycyte (blue) appears to be notably bigger and narrower than the Perftoran 10% (orange). This is explained by the higher perfluorocarbon concentration in Oxycyte that contains 60 % v/v as compared to Perftoran that contains only 10 % v/v. The chemical shift or each synthetic blood and water, and their full width at half maximum (FWHM) are listed in Table 5.5. Both Oxycyte and Perftoran 10% peaks appear at 97 and 122 ppm respectively, notably apart from the tissue or water peak that would arise from a hp ^{129}Xe lung spectrum between 192 and 213 ppm. Moreover, ^{129}Xe T_1 was measured *in vitro* $(n = 4)$ in degassed Oxycyte, giving $T_1 = 97.1 \pm 13.5\ s$. This long T_1

and specific chemical shift are used in the next part of this chapter to selectively excite the ^{129}Xe tissue or the PFCE phase in excised rat lungs.

	Chemical shift	*FWHM*
Oxycyte	97 ppm	2.4 kHz
Perftoran 10 %	122 ppm	3.6 kHz
Water	192 ppm	250 Hz

Table 5.5 Hp ^{129}Xe dissolved *in vitro* in Oxycyte, Perftoran and water peaks chemical shift and full width at half maximum (FWHM).

The ^{129}Xe-O_2 relaxivity in Oxycyte was measured *in vitro*. The O_2 was added to the hp gas mixture before being bubbled *in vitro* to the Oxycyte. T_1 was measured using a train of 8 x 24˚ flip angles pulse sequence and calculated using the Eq. 2.16 described in Section 2.4.2. The relaxivity plot is presented in Figure 5.9. The effect of O_2 on the ^{129}Xe relaxation in Oxycyte (Eq. 5.1) will permit the mixing of hp gas with oxygen before inhalation for future preclinical *in vivo* studies.

$$R_1 = (0.003678 \pm 0.000517) \times \%_{O_2} \qquad \text{Eq. 5.1}$$

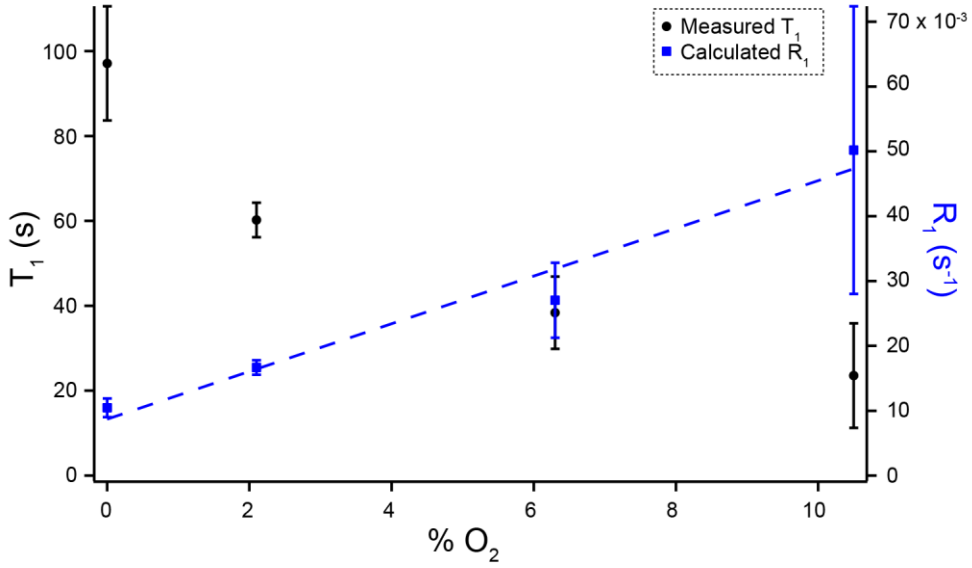

Figure 5.9 *In vitro* ^{129}Xe-O_2 relaxivity in Oxycyte. In black, the measured longitudinal relaxations, and in blue the calculated relaxivity as a function of the % O_2 in the hp gas mixture.

5.4.4. ^{129}Xe NMR of synthetic blood in excised rat lungs

5.4.4.1. Preliminary results in excised bleomycin-treated rat lungs

For the stage 2 study, some dissolved ^{129}Xe spectroscopy has been done on a bleomycin-treated lung and a control rat lung. The two rats underwent a *post mortem* blood replacement of the heart and pulmonary capillaries using Oxycyte. The protocol for the dissection and the blood replacement can be found in Section 2.8.

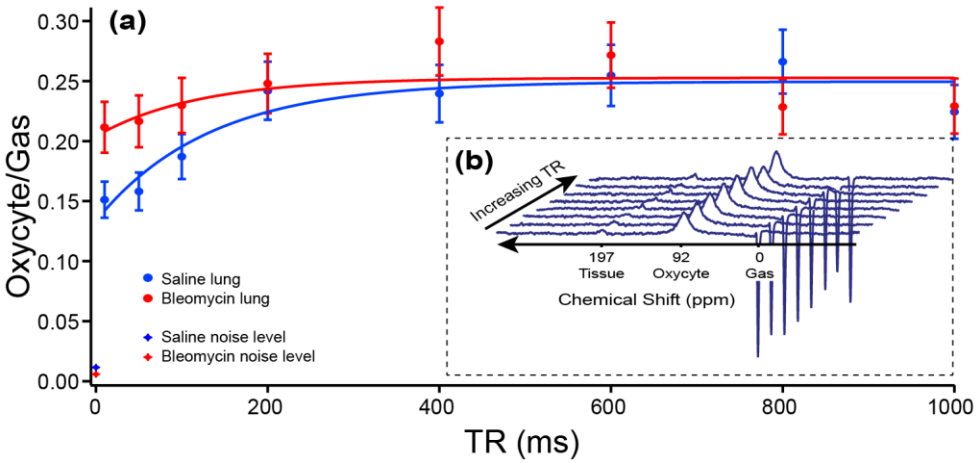

Figure 5.10 (a) Illustration of a set of chemical shift selective spectra acquired on a bleomycin-treated rat with increasing TR (64 averages). Each point represents an averaged acquisition with a given TR. (b) Oxycyte/Gas ratio in a saline-treated lung (blue) and a bleomycin-treated lung (red) and their respective noise levels. The lines represent an exponential fit of the data.

A spectrum was acquired right after inhalation of the hp gas. A chemical shift selective pulse centred on the PFCE frequency is applied, and averaged 64 times, with different repetition times. A 785 µs chemical shift selective sinc pulse was used, allowing for the excitation of the Oxycyte phase, with minor depolarization of the gas phase and the tissue phase. The acquisition of spectra with different repetition times TR ranging from 0.01 s to 1 s allows to evaluate the diffusion from the tissue to the vascular system. In the case of a gas diffusion that is slower than the repetition time, the signal will not increase, whereas a diffusion that is faster than the repetition time will induce a signal build-up.

The replenishment of the ^{129}Xe signal dissolved in Oxycyte is represented in Figure 5.10 b. This diffusion curve has been done by integrating the PFCE

peak for each spectrum with different repetition times. The diffusion in the bleomycin-treated lung from the tissue to the vasculature appears to be faster than in the saline-treated lung, in agreement with previous reports (11). This method enables for the measurement of hp ^{129}Xe diffusion from the gas to the tissue and the vascular phases but also passage of hp ^{129}Xe from the tissue to the vascular liquid.

5.4.4.2. Dynamic spectroscopy of the gas transfer in excised lungs with Perftoran 19.2 %

Chemical Shift Saturation Recovery (CSSR) is a straightforward spectroscopic technique to study the ^{129}Xe uptake by the lung parenchyma and blood in the course of a single acquisition. This technique is possible thanks to the large ^{129}Xe chemical shift between the different compartments that are the alveolar space, the lung parenchyma and the blood. By varying the delay between the RF saturation pulse and the acquisition of the spectrum, the amount of ^{129}Xe that has dissolved in the lung tissue will vary. In an *in vivo* setting, the ^{129}Xe signal arising from the parenchyma and the blood are however located very close to each other, at 198 and 218 ppm respectively, with overlapping peaks (33, 34), and is therefore challenging to selectively saturate one compartment.

Hyperpolarized ^{129}Xe uptake by the *ex vivo* lung parenchyma has been explored: the ^{129}Xe gas phase diffuses from the alveoli to the pulmonary tissue, and can then either come back to the alveolar space or advance further to the capillaries. The excised lungs underwent a *post mortem* blood replacement with Perftoran 19.2 %, allowing for a shift of the ^{129}Xe signal from the capillaries from 218 ppm to that of the PFCE, i.e. 90 ppm in the case of Perftoran 19.2 %. Such a chemical shift between the ^{129}Xe signal coming from the gas, the tissue or the blood compartments allows for the selective saturation and excitation of each of them. A 750 µs gauss shape chemical shift selective RF pulse was used to both saturate and excite each phase.

The following experiments show how selective saturation of each dissolved phase has been realised to observe ^{129}Xe build-up in the Perftoran phase and the tissue phase.

^{129}Xe dynamic spectroscopy in *ex vivo* rat lung Perftoran phase

The chemical shift selective RF pulse was centred on the Perftoran phase (90 ppm) in order to saturate the ^{129}Xe signal from the lung capillaries and evaluate the uptake of fresh hp ^{129}Xe in the Perftoran from the surrounding tissue, after varying diffusion delays. The pulse sequence consisted in a saturation RF pulse, followed by a diffusion delay $\Delta\tau$ and a spectrum acquisition, repeated with different diffusion delays (Figure 5.11 a). The RF saturation pulse is followed by a spoiler gradient dephasing the residual transverse magnetization. Most experiments shown in this chapter were composed of 10 to 12 increasing delays in a single breath-hold acquisition. The Perftoran phase (at 90 ppm) was integrated and normalised to the gas phase (0 ppm) integral. CSSR build-up curves of the ^{129}Xe Perftoran/Gas signal are displayed in Figure 5.12.

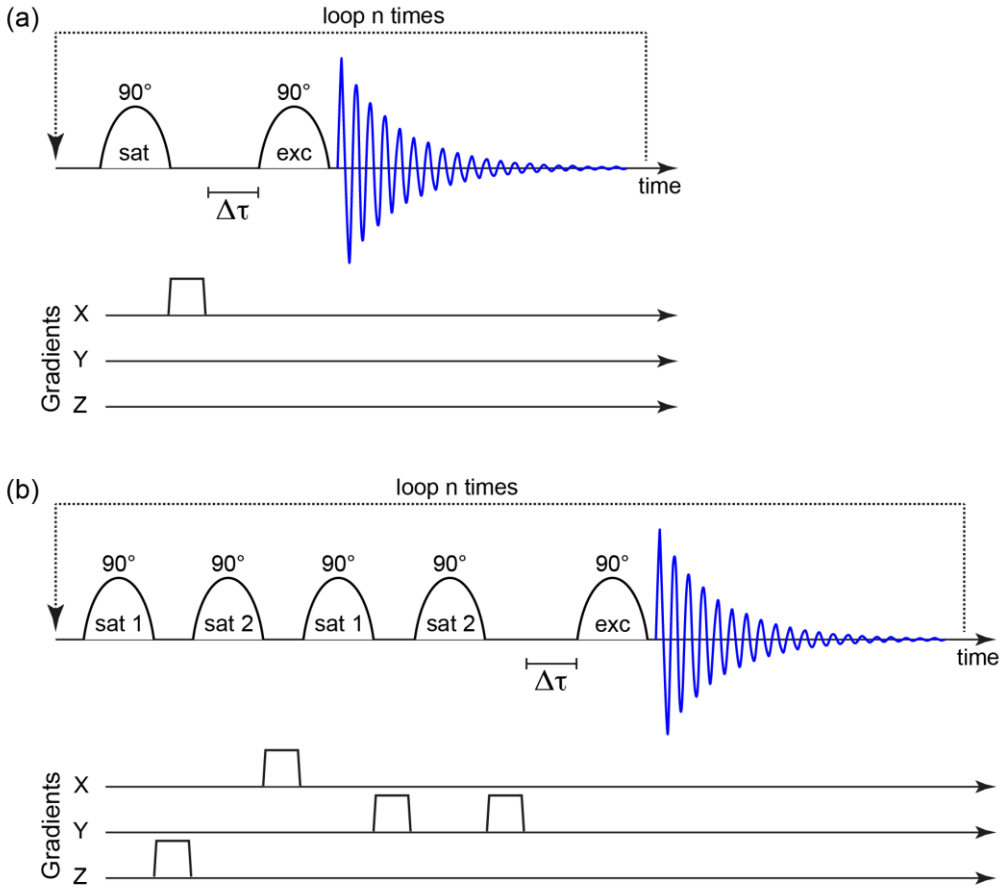

Figure 5.11 CSSR pulse sequences used in this section. (a) Single selective saturation, followed by a dephasing gradient, and selective excitation of a given dissolved ^{129}Xe phase. (b) 4 saturations spoilers followed by excitation. The 4 saturation pulses can be set to a single frequency ($sat1 = sat2 = tissue$) to saturate a single compartment or two frequencies ($sat1 = tissue$, $sat1 = Perftoran$) to saturate all dissolved ^{129}Xe.

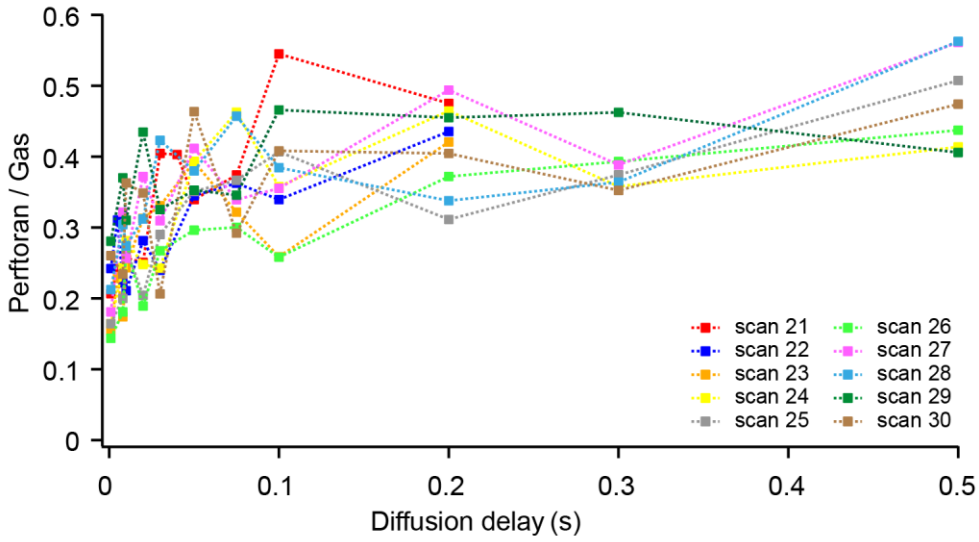

Figure 5.12 Replenishing of the ^{129}Xe magnetization in Perftoran (90 ppm) in an *ex vivo* healthy rat lung. Each signal recovery curve was acquired during a single breath-hold, after inhalation of the hyperpolarized ^{129}Xe gas mixture and lung using the CSSR pulse sequence illustrated in Figure 5.11 a.

The Perftoran signal build-up appears repeatable, and not dependent on the diffusion delays ($\Delta\tau$) that were used during a single acquisition. Data have been clustered when identical diffusion delays ($\Delta\tau$) were used during the acquisition as listed in Table 5.6 and were displayed in Figure 5.13.

The ^{129}Xe gas transport through the alveolar structure was following an exponential diffusion. The augmentation of the ^{129}Xe magnetization that has built-up in the dissolved compartments is described by Eq. 5.2 and displayed on Figure 5.13.

$$S(t) = S_A - S_B \times \exp\left(-\frac{t}{T_{diff}}\right) \qquad \text{Eq. 5.2}$$

where $(S_B - S_A)$ is the intercept at $t = 0$ and T_{diff} the exponential time constant. The fitting parameters for the data sets summarizing the two Perftoran/Gas signal build-up curves from Figure 5.13 are listed in Table 5.7.

Scans 21 - 23 *Green*	*Scans 24 - 30* *Red*
0.001	0.001
0.005	0.008
0.01	0.01
0.02	0.02
0.03	0.03
0.04	0.05
0.05	0.075
0.075	0.1
0.1	0.2
0.2	0.3
-	0.5

Table 5.6 List of the diffusion delays $\Delta\tau$ (in s) that were used for all magnetization recovery experiments displayed in Figure 5.12 and 5.13.

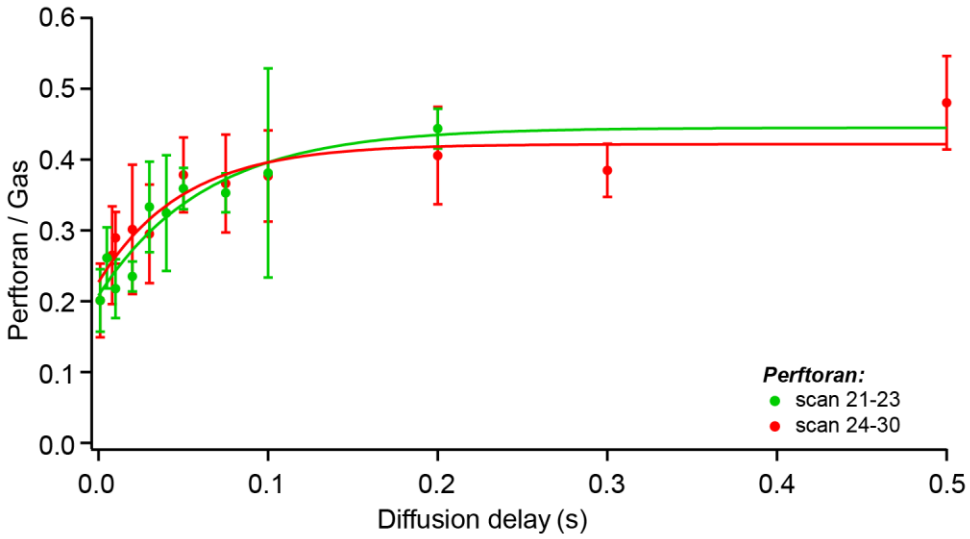

Figure 5.13 Replenishing of the ^{129}Xe magnetization dissolved in Perftoran (90 ppm) in an *ex vivo* healthy rat lung. Data sets from Figure 5.12 were regrouped when identical diffusion delays between the saturation and the excitation pulses were used (see Table 5.6 for delay lists). Averages and standard deviations are displayed; an exponential function as in Eq. 5.2 was fitted on each signal build-up.

	n	$S_B - S_A$	T_{diff} (s)
Green	3	0.208 ± 0.050	0.063 ± 0.024
Red	7	0.227 ± 0.055	0.049 ± 0.019
All scans	10	0.228 ± 0.053	0.058 ± 0.016

Table 5.7 Fitting parameters on the two datasets displayed in Figure 5.13. n represents the number of build-up curves with identical diffusion delays ($\Delta\tau$) that were averaged together. All scans were also put in a single data set and displayed in Figure 5.14.

The red and green data sets present similar fitting results with an exponential time constant T_{diff} of 63 and 49 ms respectively. This time constant illustrates the ^{129}Xe diffusion from the tissue to the Perftoran in the capillaries.

The 10 Perftoran signal recovery datasets were gathered to a single build-up curve and displayed in Figure 5.14. The fitting parameters are also listed in Table 5.7. The ^{129}Xe signal arising from the Perftoran phase increases to its maximum within 150 ms to reach a plateau. This plateau would increase with a light slope in the case of a live experiment with blood flow (10, 11).

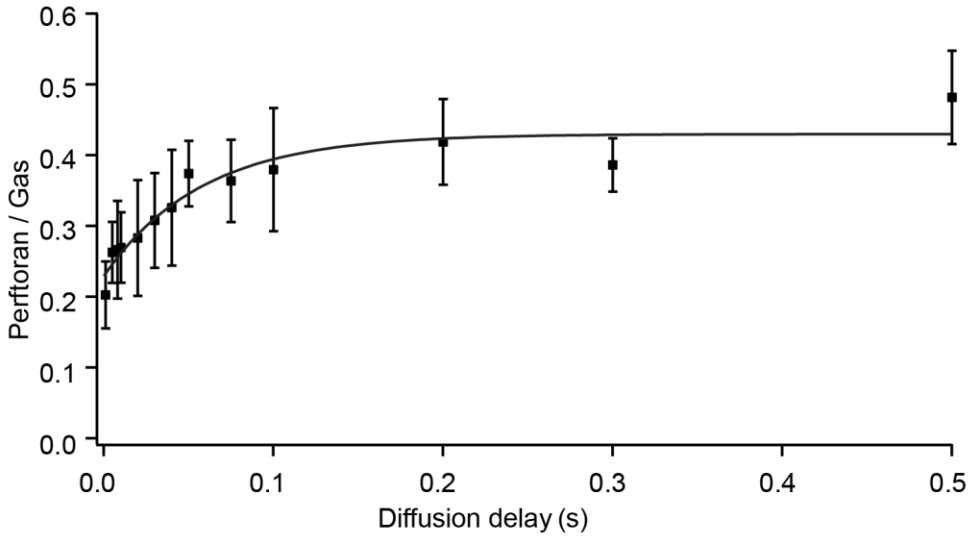

Figure 5.14 Replenishing of the ^{129}Xe magnetization dissolved in Perftoran (90 ppm). All data from Figure 5.12 (n = 10) were grouped. Averages and standard deviations are displayed; an exponential fit was applied to the signal build-up.

As a summary, the Perftoran signal is observed to increase up to a maximum reached within 150 ms. For more consistent results, averaging of the same diffusion delay could be done within the same CSSR acquisition and one breath hold. This way the signal scattering could be reduced.

^{129}Xe dynamic spectroscopy in *ex vivo* rat lung tissue phase

The ^{129}Xe signal dissolved in the tissue represents a much bigger proportion of the overall signal than that of the Perftoran, described in the previous section. The detection of the ^{129}Xe dissolved in the tissue is therefore easier. Moreover, the larger chemical shift between the gas phase and the tissue phase allows for minimal saturation and excitation of the bulk gas phase during the CSSR experiment (Figure 5.8). A better repeatability is expected when studying this ^{129}Xe phase.

All individual tissue signal recovery curves are displayed in Figure 5.15, where slightly different pulse programs were used (Figure 5.11). The first CSSR pulse sequence that was used consisted on a single saturation of the tissue phase and the observation of the tissue signal build-up (Figure 5.11 a) similarly to the previously shown Perftoran signal build-up acquisition. The second CSSR pulse sequence introduced the saturation of the Perftoran phase interlaced with the saturation of the tissue phase (Figure 5.11 b), with a total of 4 saturation pulses before each excitation and CSSR step. Data are displayed in Figure 5.15 a and b.

The fitting parameters for clustered data (experiments with identical diffusion delays $\Delta\tau$ as listed in Table 5.8), and their saturation scheme are listed in Table 5.9. Curves fitting the diffusion model are showed in Figure 5.16.

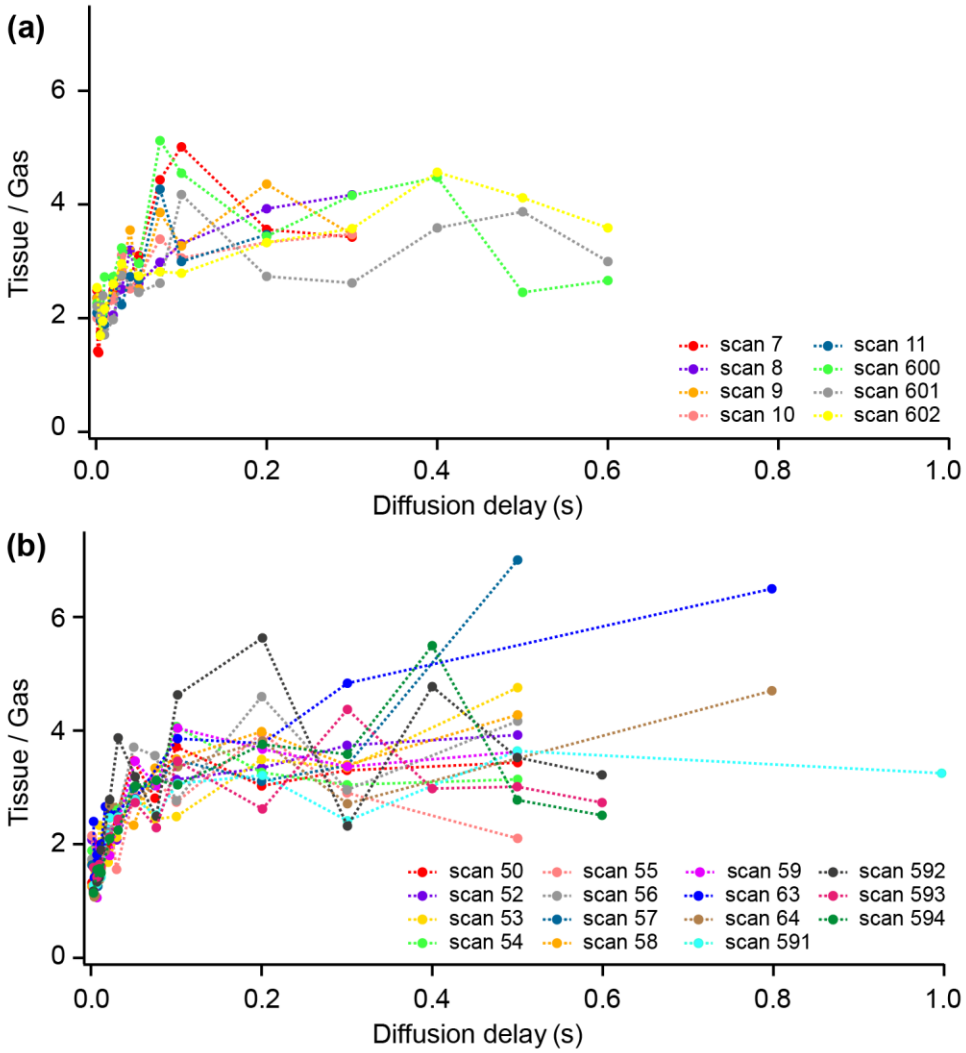

Figure 5.15 Replenishing of the ^{129}Xe magnetization dissolved in the tissue (195 ppm) in an *ex vivo* healthy rat lung. Individual signal recovery curves are represented. (a) Saturation of the tissue only as in Figure 5.11 a. (b) Saturation of the tissue and Perftoran following a 4 RF saturations scheme as in Figure 5.11 b.

Scans 8 - 10 Green	*Scans 600 - 602 Yellow*	*Scans 52 - 58 Blue*	*Scans 63 - 64 Grey*	*Scans 592 - 594 Red*	*Scan 591 Pink*
0.001	0.001	0.001	0.008	0.02	0.001
0.01	0.005	0.005	0.01	0.03	0.005
0.02	0.008	0.008	0.015	0.05	0.008
0.03	0.01	0.01	0.02	0.075	0.01
0.04	0.02	0.02	0.05	0.1	0.02
0.05	0.03	0.03	0.1	0.2	0.03
0.075	0.05	0.05	0.2	0.3	0.05
0.1	0.075	0.075	0.3	0.4	0.075
0.2	0.1	0.1	0.8	0.5	0.1
0.3	0.2	0.2	-	0.6	0.2
-	0.3	0.3	-	-	0.3
-	0.4	0.5	-	-	0.5
-	0.5	-	-	-	1
-	0.6	-	-	-	-

Table 5.8 List of the diffusion delays $\Delta\tau$ (in s) that were used for all scans displayed in Figure 5.15 and 5.16. Colours indicate the build-up curves in Figure 5.16 and Table 5.9.

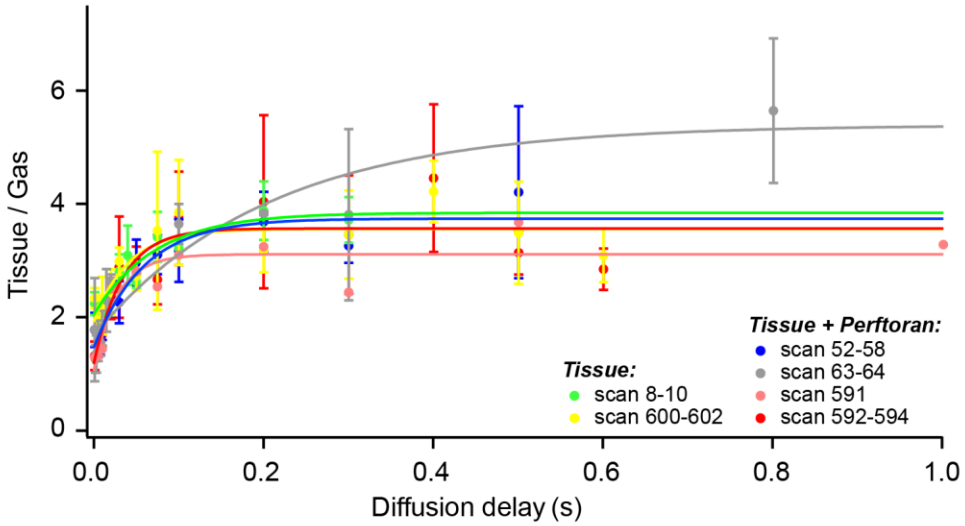

Figure 5.16 Replenishing of the ^{129}Xe magnetization dissolved in the lung parenchyma (195 ppm) in an *ex vivo* healthy rat lung. Data sets were regrouped when identical diffusion delays $\Delta\tau$ between the saturation and the FID acquisition were used. Averages and standard deviations are displayed; an exponential function was fitted on each signal build-up. Details on the saturation schemes for each colour group can be found in Table 5.9.

Not perceptible in the integrated signal build-up curves (Figure 5.16), when fitted with an exponential function, the ^{129}Xe dissolved in the tissue appears to build-up faster when only the tissue has been saturated as compared to a saturation of both tissue and Perftoran phases as listed in Table 5.9.

The exponential component of the signal build-up T_{diff} is equal to 57 ms on average when both tissue and Perftoran have been saturated, and the hp ^{129}Xe can only be provided from the gas phase alveolar reservoir. On the other side, T_{diff} is reduced to 47 ms when the tissue only has been saturated and the hp ^{129}Xe can therefore either come from the alveolar reservoir, or diffuse back from the Perftoran seating in the vascular system.

	n	*Saturation scheme*	$S_B - S_A$	T_{diff} *(s)*	*Average* T_{diff} ± *st. deviation (s)*
Green	3	Tissue	2.04 ± 0.12	0.057 ± 0.016	0.047 ± 0.016
Yellow	3	Tissue	1.91 ± 0.21	0.040 ± 0.019	
Blue	7	Tissue + Perftoran	1.46 ± 0.21	0.059 ± 0.017	0.057 ± 0.024
Grey	2	Tissue + Perftoran	1.68 ± 0.67	0.206 ± 0.072	
Red	3	Tissue + Perftoran	1.18 ± 0.28	0.034 ± 0.014	
Pink	1	Tissue + Perftoran	1.06	0.027	

Table 5.9 CSSR scan saturation schemes and fitting parameters for the diffusion model for six magnetization build-ups displayed in Figure 5.16. The average T_{diff} for the tissue signal build-up after saturation of the tissue only or tissue + Perftoran is indicated.

The choice of diffusion delays used during the CSSR acquisition appears to be an important parameter inducing some variability in the obtained data. The grey data set represented in Figure 5.16 does not display a similar growth as the other build-up curves. This might be due to the high number of very low $\Delta\tau$ delays and unique longer $\Delta\tau$ (see Table 5.8).

The ^{129}Xe diffusion from the alveolar gas space to the parenchyma follows a 1D and 2-phase system diffusion through a single layer of porous medium (35) and should follow:

$$S(\tau) \propto \sqrt{2D\tau} \qquad \text{Eq. 5.3}$$

where D is the diffusion coefficient of ^{129}Xe in the dissolved phase and τ the diffusion delay. The build-up data collected after saturation of the tissue phase or both tissue and blood compartments were plotted against $\sqrt{\tau}$ (Figure 5.17).

The dissolved signal increases linearly with $\sqrt{\tau}$ for short times before the tissue saturates (35). The septal uptake curves represent how fast the ^{129}Xe builds up in the tissue. ^{129}Xe diffuses back from the alveolar airspace when the tissue and Perftoran phases were saturated (Figure 5.17, green points) whereas it will diffuse from the airspace and the capillaries in the case of the saturation of the sole tissue phase (Figure 5.17, orange points). The normalised signal shows a non-zero y-intercept due to an immediately saturated thin layer of tissue at the interface with the gas phase and the capillaries. The amount of tissue very quickly saturated is 1.5 times higher in the case of the saturation of the tissue

only, as some ^{129}Xe will rapidly enter the tissue on the alveolar side and the capillaries side.

The difference in the build-up slopes can also be explained by the different saturation schemes as well. As explained in the previous paragraph, they do not start with the same amount of signal. Furthermore, both build-ups reach a plateau of full saturation of the tissue with ^{129}Xe at around $\sqrt{\tau} = 0.3\ s^{1/2}$. Therefore, the slope in Figure 5.17 is decreased from $7.4 \pm 0.7\ s^{-1/2}$ when the tissue and Perftoran phases were saturated to $5.8 \pm 0.9\ s^{-1/2}$ when the tissue only was saturated, explaining the previously observed slightly different build-up times T_{diff} for each saturation schemes (Table 5.9).

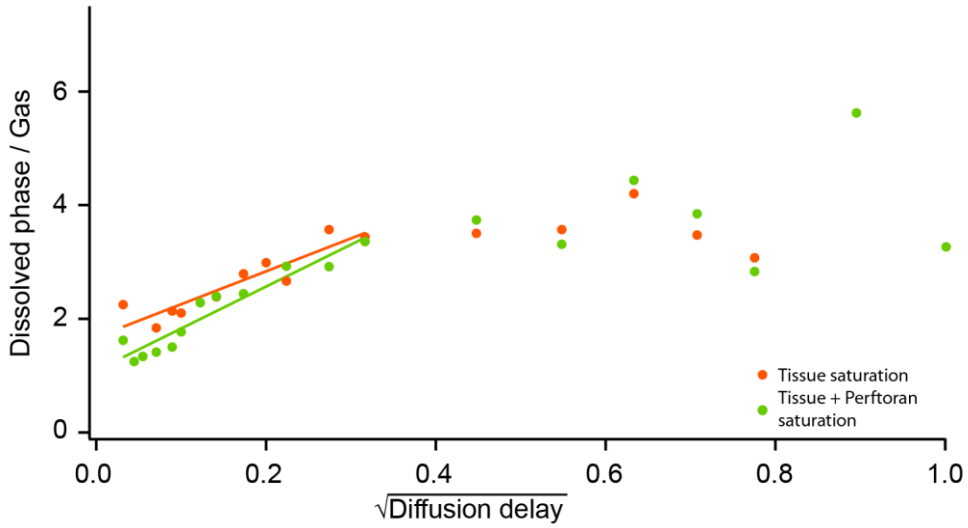

Figure 5.17 Experimentally measured and normalised signal from the tissue phase as a function of $\sqrt{\Delta\tau}$. Orange data were acquired after saturation of the tissue phase (195 ppm) whereas green data were acquired after saturation of both the tissue phase and the Perftoran phase (90 ppm).

5.5. Conclusions

In this study, we have used hyperpolarized ^{129}Xe to evaluate the gas diffusion through excised rat lungs. We have demonstrated that CSSR dynamic spectroscopy with perfluorocarbon emulsion as a blood replacement in excised lungs allows for the selective saturation and detection of the ^{129}Xe dissolved in the tissue or the blood compartments. The technique is sensitive enough to detect the Perftoran signal located in the capillaries, independently to the tissue signal, with a clear chemical shift difference and no peak overlap with neither the tissue nor the gas phase. The selective saturation has allowed the measurement of the signal build-up in each phase, with no saturation of the other ^{129}Xe phases. Different exponential time constants for the signal build-up were observed in the tissue phase when the tissue only or both the tissue and the Perftoran phases have been saturated. This difference was emphasised by the representation of the signal build-up against $\sqrt{\tau}$, showing a faster build-up at short times when only the tissue was saturated (Figure 5.17).

The measurement of such parameter should be further studied in animal models where the gas exchange is impaired. This technique would replace the technically difficult lung function tests in small animals, but however necessitate sacrificing the animal and replacing the blood by PFCE. The use of theoretical models such as the Månsson model (11) on these build-up curves, or even the Patz model (10) and the MOXE model (36) will allow for the exploration of animal models such as the bleomycin rat model described by a parenchymal thickening, in synergy with DLCO (diffusing capacity of the lung for carbon monoxide), a clinical test measuring the gas transfer from the airspace to the RBC. These mathematical models use CSSR build-up data and fitting parameters to provide thickness measurements of the parenchyma, or the alveolar diameter. Histological studies would confirm the fibrotic thickening (37). Moreover, a regional mapping of the gas uptake in the PFCE will be possible using the XTC technique developed by Ruppert et al. (7). The multimodality of the hyperpolarization techniques would allow the evaluation of both parenchymal thickening and alveolar degradation using hp ^{129}Xe magnetization kinetics and hp ^{83}Kr T_1 relaxation mapping respectively. The bleomycin-induced viscoelastic changes and alveolar degradation will be

assessed using plethysmography (38). Finally, recent advances on ^{19}F sensitivity (39) allowed for the quantification of the minimum detectable fluorine concentration in the sample under the given laboratory hardware settings, and would allow the ^{19}F MRI of the PFCE in the lungs.

Even if the three ^{129}Xe phases are separated by a large chemical shift and do not require a very narrow and selective pulse (e.g. reference (12) used a custom-designed RF pulse), particular considerations should be taken to avoid the possible hardware difficulties that we encountered during the course of this study. The coils should have an homogeneous excitation in order to allow a precise calibration of the chemical shift selective low power RF pulse. The coil should also have a sufficient shielding to avoid any RF noise. Indeed, the CSSR spectra acquired for this work were presenting a low frequency noise that appeared at a very close frequency to that of the ^{129}Xe dissolved in tissue and at the early diffusion delays, therefore substantially altering the calculated diffusion constants T_{diff}.

The partial blood replacement with PFCE for *in vivo* exploration would complicate the model as the red blood cells ^{129}Xe peak would appear close to the tissue peak and there would be two peaks representing one compartment, therefore reducing the amount of signal in both. This study is however possible, and both peaks should show similar build-ups. Moreover, the use of breathable hyperpolarized gas mixed with 21% O_2 would provide a sufficiently long $T_1 = 12.9\ s$ in the PFCE phase (Figure 5.9).

The perfluorocarbon emulsion (PFCE) concentration appeared to be an important factor. The original Perftoran 10 % was not providing sufficient dissolved ^{129}Xe signal within the excised lungs (data not shown) and required concentrating it up to 19.2 %. The concentration process involves slight heating and vacuum of the solution, which might be deleterious for the emulsion compound. Some investigations on the Perftoran structural change upon concentration should be done.

5.6. References

1. Driehuys B, Cofer GP, Pollaro J, Mackel JB, Hedlund LW, Johnson GA. Imaging alveolar-capillary gas transfer using hyperpolarized Xe-129 MRI. Proceedings of the National Academy of Sciences of the United States of America. 2006;103(48):18278-83.

2. Kaushik SS, Freeman MS, Yoon SW, Liljeroth MG, Stiles JV, Roos JE, et al. Measuring diffusion limitation with a perfusion-limited gas-Hyperpolarized Xe-129 gas-transfer spectroscopy in patients with idiopathic pulmonary fibrosis. Journal of Applied Physiology. 2014;117(6):577-85.

3. Cleveland ZI, Virgincar RS, Qi Y, Robertson SH, Degan S, Driehuys B. 3D MRI of impaired hyperpolarized Xe-129 uptake in a rat model of pulmonary fibrosis. Nmr in Biomedicine. 2014;27(12):1502-14.

4. Swanson SD, Rosen MS, Coulter KP, Welsh RC, Chupp TE. Distribution and dynamics of laser-polarized Xe-129 magnetization in vivo. Magnetic Resonance in Medicine. 1999;42(6):1137-45.

5. Albert MS, Schepkin VD, Budinger TF. Measurement of Xe-129 T1 in Blood to Explore the Feasibility of Hyperpolarized Xe-129 Mri. Journal of Computer Assisted Tomography. 1995;19(6):975-8.

6. Ratcliffe CI. Xenon NMR. Annual Reports on NMR Spectroscopy. 1998;36:123-221.

7. Ruppert K, Brookeman JR, Hagspiel KD, Mugler JP. Probing lung physiology with xenon polarization transfer contrast (XTC). Magnetic Resonance in Medicine. 2000;44(3):349-57.

8. Driehuys B, Möller HE, Cleveland ZI, Pollaro J, Hedlund LW. Pulmonary Perfusion and Xenon Gas Exchange in Rats: MR Imaging with Intravenous Injection of Hyperpolarized 129Xe. Radiology. 2009;252(2):386-93.

9. Abdeen N, Cross A, Cron G, White S, Rand T, Miller D, et al. Measurement of xenon diffusing capacity in the rat lung by hyperpolarized 129Xe MRI and dynamic spectroscopy in a single breath-hold. Magnetic Resonance in Medicine. 2006;56(2):255-64.

10. Patz S, Muradyan I, Hrovat MI, Dabaghyan M, Washko GR, Hatabu H, et al. Diffusion of hyperpolarized (129)Xe in the lung: a simplified model of

(129)Xe septal uptake and experimental results. New Journal of Physics. 2011;13:015009.

11. Mansson S, Wolber J, Driehuys B, Wollmer P, Golman K. Characterization of diffusing capacity and perfusion of the rat lung in a lipopolysaccaride disease model using hyperpolarized Xe-129. Magnetic Resonance in Medicine. 2003;50(6):1170-9.

12. Stewart NJ, Leung G, Norquay G, Marshall H, Parra-Robles J, Murphy PS, et al. Experimental validation of the hyperpolarized Xe-129 chemical shift saturation recovery technique in healthy volunteers and subjects with interstitial lung disease. Magnetic Resonance in Medicine. 2015;74(1):196-207.

13. Cleveland ZI, Cofer GP, Metz G, Beaver D, Nouls J, Kaushik SS, et al. Hyperpolarized Xe-129 MR Imaging of Alveolar Gas Uptake in Humans. Plos One. 2010;5(8).

14. Bifone A, Song YQ, Seydoux R, Taylor RE, Goodson BM, Pietrass T, et al. NMR of laser-polarized xenon in human blood. Proceedings of the National Academy of Sciences of the United States of America. 1996;93(23):12932-6.

15. Amor N, Hamilton K, Kuppers M, Steinseifer U, Appelt S, Blumich B, et al. NMR and MRI of Blood-Dissolved Hyperpolarized Xe-129 in Different Hollow-Fiber Membranes. Chemphyschem. 2011;12(16):2941-7.

16. Cleveland ZI, Moller HE, Hedlund LW, Nouls JC, Freeman MS, Qi Y, et al. In Vivo MR Imaging of Pulmonary Perfusion and Gas Exchange in Rats via Continuous Extracorporeal Infusion of Hyperpolarized Xe-129. Plos One. 2012;7(2).

17. Venkatesh AK, Zhao L, Balamore D, Jolesz FA, Albert MS. Evaluation of carrier agents for hyperpolarized xenon MRI. Nmr in Biomedicine. 2000;13(4):245-52.

18. Agusti AGN, Roca J, Gea J, Wagner PD, Xaubet A, Rodriguezroisin R. Mechanisms of gas-exchange impairment in idiopathic pulmonary fibrosis. American Review of Respiratory Disease. 1991;143(2):219-25.

19. Egger C, Cannet C, Gerard C, Jarman E, Jarai G, Feige A, et al. Administration of Bleomycin via the Oropharyngeal Aspiration Route Leads to

Sustained Lung Fibrosis in Mice and Rats as Quantified by UTE-MRI and Histology. Plos One. 2013;8(5):13.

20. Wolber J, Rowland IJ, Leach MO, Bifone A. Intravascular delivery of hyperpolarized (129)xenon for in vivo MRI. Applied Magnetic Resonance. 1998;15(3-4):343-52.

21. Wolber J, Rowland IJ, Leach MO, Bifone A. Perfluorocarbon emulsions as intravenous delivery media for hyperpolarized xenon. Magnetic Resonance in Medicine. 1999;41(3):442-9.

22. Amor N, Zanker PP, Blumler P, Meise FM, Schreiber LM, Scholz A, et al. Magnetic resonance imaging of dissolved hyperpolarized Xe-129 using a membrane-based continuous flow system. Journal of Magnetic Resonance. 2009;201(1):93-9.

23. Baumer D, Brunner E, Blumler P, Zanker PP, Spiess HW. NMR spectroscopy of laser-polarized Xe-129 under continuous flow: A method to study aqueous solutions of biomolecules. Angewandte Chemie-International Edition. 2006;45(43):7282-4.

24. Albert MS, Balamore D, Kacher DF, Venkatesh AK, Jolesz FA. Hyperpolarized Xe-129 T-1 in oxygenated and deoxygenated blood. Nmr in Biomedicine. 2000;13(7):407-14.

25. Lilburn DML, Hughes-Riley T, Six JS, Stupic KF, Shaw DE, Pavlovskaya GE, et al. Validating Excised Rodent Lungs for Functional Hyperpolarized Xenon-129 MRI. Plos One. 2013;8(8).

26. Six JS, Hughes-Riley T, Lilburn DML, Dorkes AC, Stupic KF, Shaw DE, et al. Pulmonary MRI contrast using Surface Quadrupolar Relaxation (SQUARE) of hyperpolarized Kr-83. Magnetic Resonance Imaging. 2014;32(1):48-53.

27. Hughes-Riley T, Six JS, Lilburn DML, Stupic KF, Dorkes AC, Shaw DE, et al. Cryogenics free production of hyperpolarized 129Xe and 83Kr for biomedical MRI applications. Journal of Magnetic Resonance. 2013;237:23-33.

28. Moeller A, Ask K, Warburton D, Gauldie J, Kolb M. The bleomycin animal model: A useful tool to investigate treatment options for idiopathic pulmonary fibrosis? International Journal of Biochemistry & Cell Biology. 2008;40(3):362-82.

29. Keipert PE, Faithfull NS, Bradley JAD, Hazard DY, Hogan J, Levisetti MS, et al. Oxygen delivery augmentation by low-dose perfluorochemical emulsion during profound normovolemic hemodilution. In: Vaupel P, Zander R, Bruley DF, editors. Oxygen Transport to Tissue Xv. Advances in Experimental Medicine and Biology. 345. New York: Plenum Press Div Plenum Publishing Corp; 1994. p. 197-204.

30. Woitzik J, Weinzierl N, Schilling L. Early administration of a second-generation perfluorochemical decreases ischemic brain damage in a model of permanent middle cerebral artery occlusion in the rat. Neurological Research. 2005;27(5):509-15.

31. Borzone G, Moreno R, Urrea R, Meneses M, Oyarzun M, Lisboa C. Bleomycin-Induced Chronic Lung Damage Does Not Resemble Human Idiopathic Pulmonary Fibrosis. American Journal of Respiratory and Critical Care Medicine. 2001;163(7):1648-53.

32. Stupic KF, Elkins ND, Pavlovskaya GE, Repine JE, Meersmann T. Effects of pulmonary inhalation on hyperpolarized krypton-83 magnetic resonance T-1 relaxation. Physics in Medicine and Biology. 2011;56(13):3731-48.

33. Mugler JP, Driehuys B, Brookeman JR, Cates GD, Berr SS, Bryant RG, et al. MR imaging and spectroscopy using hyperpolarized Xe-129 gas: Preliminary human results. Magnetic Resonance in Medicine. 1997;37(6):809-15.

34. Wolber J, Cherubini A, Dzik-Jurasz ASK, Leach MO, Bifone A. Spin-lattice relaxation of laser-polarized xenon in human blood. Proceedings of the National Academy of Sciences of the United States of America. 1999;96(7):3664-9.

35. Patz S, Muradian I, Hrovat MI, Ruset IC, Topulos G, Covrig SD, Frederick E, Hatabu H, Hersman FW, Butler JP. Human pulmonary imaging and spectroscopy with hyperpolarized Xe-129 at 0.2T. Academic Radiology 2008;15(6):713-727.

36. Chang YV. MOXE: A model of gas exchange for hyperpolarized 129Xe magnetic resonance of the lung. Magnetic Resonance in Medicine. 2013;69(3):884-90.

37. Hesterberg TW, Gerriets JE, Reiser KM, Jackson AC, Cross CE, Last JA. Bleomycin-induced pulmonary fibrosis: Correlation of biochemical, physiological, and histological changes. Toxicology and Applied Pharmacology. 1981;60(2):360-7.
38. Dolhnikoff M, Mauad T, Ludwig MS. Extracellular Matrix and Oscillatory Mechanics of Rat Lung Parenchyma in Bleomycin-induced Fibrosis. American Journal of Respiratory and Critical Care Medicine. 1999;160(5):1750-7.
39. Taylor AJ, Granwehr J, Lesbats C, Krupa JL, Six JS, Pavlovskaya GE, et al. Probe-Specific Procedure to Estimate Sensitivity and Detection Limits for 19F Magnetic Resonance Imaging. PLoS One. 2016;11(10):e0163704.

CHAPTER 6

CONCLUSIONS AND FUTURE OUTLOOK

The work presented in this thesis investigates hyperpolarized ^{83}Kr and ^{129}Xe as biomarkers for pulmonary diseases. Three potential markers have been evaluated in *ex vivo* rat lungs and in solution.

(i) The ^{83}Kr surface quadrupolar relaxation (SQUARE) has been validated in excised healthy rat lungs prior to the work realised for this thesis (1). ***Chapter 3*** and (2) detail an application of this technique to an animal model of emphysema, where the surface-to-volume ratio within the lungs is decreased due to an alveolar wall destruction. The ^{83}Kr SQUARE T_1 maps allow for a qualitative discrepancy between healthy and emphysematous lungs. The analysis of the overall T_1 distribution within the lungs demonstrated a significant difference between the control and treated animals. A correlation analysis also indicated a relationship between the regional ^{83}Kr relaxation behaviour and the histologically measured alveolar dimensions in each lobe. Some further work can be done on the *ex vivo* animal model of emphysema. The obtained results can be compared to ^{129}Xe ADC MRI that has been correlated to the alveolar radius (3). Furthermore, the mean alveolar area (MAA) has been proved to be an efficient measurement for the S/V in the lungs, but most hyperpolarized studies were using the gold standard histological intercept measurement. In future works, this could be addressed with a new cohort of rats. Further comparisons with the S/V obtained through SQUARE with that from hp ^{129}Xe ADC measurements and hp ^{129}Xe dissolved phase measurements would shine further light on this new biomarker.

Such surface-to-volume ratio dependent ^{83}Kr contrast will be implemented to a human scale MRI system at the Sir Peter Mansfield Imaging Centre. Once the threshold for healthy human alveolar T_1 will be determined, the SQUARE maps will provide an easy and early diagnosis of emphysema. The translation of this technology from excised rat lungs to human lungs involves a 3-fold increase in the alveolar diameter. The T_1 relaxation is therefore expected to increase by three times (4). The shift from 9.4 T to lower B_0 magnetic field, 7

T, might however shorten the T_1 relaxation (5). Better imaging protocols should be implemented to improve the image signal-to-noise ratio (SNR) with a bigger coil. It should be noted that there is a lot of room for optimization of the experimental protocol. For example, the production of hp ^{83}Kr can be further improved leading to higher signal intensity (6). Furthermore, EPI acquisition schemes utilizing the long T_2 relaxation time of ^{83}Kr and compressed sensing can be explored and counteract sensitivity limitations. EPI would have the advantage of using 90° pulses instead of small flip angle excitation, thereby potentially improving signals 5-fold over what is currently been used. Lastly, better coil design for the low radiofrequency of ^{83}Kr may further improve sensitivity.

(ii) The investigations on a new ^{129}Xe biosensor has been presented in ***Chapter 4*** and (7). It is based on the tethering of a cryptophane A to a paramagnetic GdDOTA group inducing the fast depolarization of the encapsulated ^{129}Xe, that subsequently exchanges with the surrounding dissolved ^{129}Xe atoms. Different molecular derivatives of the model biosensor were tested *in vitro*. ^{129}Xe relaxation was induced by the close vicinity of the noble gas atom and the paramagnetic GdDOTA, and is displaced by fast chemical exchange from the cage to the medium. This sensor showed clearly different relaxation behaviour when the cage was tethered to a GdDOTA and when it was not. Unlike most ^{129}Xe biosensors, it is not based on the detection of a small chemical shift but the measurement of the dissolved phase (~200 ppm) and will not require a high spectral resolution thanks to a low background noise level.

A functionalised biosensor will be evaluated. This time, the linker between the cryptophane A cage and the paramagnetic GdDOTA will be the target of MMP-9, an abundant enzyme in diseased lungs. The presence of the enzyme would induce the cleavage of the biosensor and therefore no relaxation will be generated. In the absence of the MMP-9 enzyme, the biosensor remains intact and a fast relaxation of the hyperpolarized ^{129}Xe would be induced as shown in ***Chapter 4***. This will induce a positive contrast, with a higher signal appearing from the places where the enzyme is present. This would however necessitate an homogeneous repartition of the biosensor in the organ. This issue will be overcome by assessing the biosensor repartition in the organism, using ^{1}H MRI

as it has been shown that the proton relaxation is unaffected by the cleavage of the molecule.

(iii) In ***Chapter 5***, the use of synthetic blood has permitted for a clear distinction of the blood compartment on an *ex vivo* rat lung ^{129}Xe NMR spectrum. The complete blood replacement in the excised organ tackles the problem of the dissolved ^{129}Xe overlapping peaks *in vivo*. Instead of displaying three peaks for the red blood cells, the plasma and adipose cells, and the lung parenchyma, the dissolved ^{129}Xe spectrum only shows two peaks for the lung tissue (195 ppm) and the synthetic blood (90 ppm). The two compartments can be selectively excited thanks to their separated respective chemical shifts. This compartmentalization in excised lungs will allow for novel evaluation of the gas transfer in animal models.

The use of better coil could improve the selective saturation and excitation, and homogeneity across the sample region. The synthetic blood needed to be concentrated to be able to detect the ^{129}Xe dissolved in the lung capillaries. The ^{129}Xe chemical shift and T_1 should be evaluated in the synthetic blood after concentrating it, in order to verify the good quality of the product after the procedure. More improvements can be done on the dynamic spectroscopy protocols, with optimized delays, saturations, randomisation, and averaging. This will allow for more applications in excised lungs of animal models. The difference in ^{129}Xe diffusion through the parenchyma should be observed in an animal model of pulmonary fibrosis and analysed using diffusion models (8-10). Some imaging techniques such as XTC (11) can be derived from the knowledge of the gas diffusion behaviour in the healthy and pathologic lungs. Finally, despite the complex ^{19}F spectrum *in vitro* and *in vivo*, recent advances in ^{19}F NMR and MRI sensitivity will allow for a mapping of the capillaries in the organ.

The work presented in this document intends to find biomarkers for specific characteristics of pulmonary diseases. Multimodal imaging will facilitate pulmonary diagnosis by addressing the variety and complexity of lung pathologies. The combination of ^{129}Xe and ^{83}Kr with the markers described in

this work seeks to enable the evaluation of both the alveolar structural integrity and the parenchymal thickness.

References

1. Six JS, Hughes-Riley T, Lilburn DML, Dorkes AC, Stupic KF, Shaw DE, et al. Pulmonary MRI contrast using Surface Quadrupolar Relaxation (SQUARE) of hyperpolarized Kr-83. Magnetic Resonance Imaging. 2014;32(1):48-53.

2. Lilburn DML, Lesbats C, Six JS, Dubuis E, Yew-Booth L, Shaw DE, et al. Hyperpolarized Kr-83 magnetic resonance imaging of alveolar degradation in a rat model of emphysema. Journal of the Royal Society Interface. 2015;12(107).

3. Boudreau M, Xu X, Santyr GE. Measurement of 129Xe gas apparent diffusion coefficient anisotropy in an elastase-instilled rat model of emphysema. Magn Reson Med. 2013;69(1):211-20.

4. Cleveland ZI, Meersmann T. Studying porous materials with krypton-83 NMR spectroscopy. Magnetic Resonance in Chemistry. 2007;45:S12-S23.

5. Cleveland ZI, Pavlovskaya GE, Stupic KF, LeNoir CF, Meersmann T. Exploring hyperpolarized 83Kr by remotely detected NMR relaxometry. Journal of Chemical Physics. 2006;124:044312.

6. Rogers NJ, Hill-Casey F, Stupic KF, Six JS, Lesbats C, Rigby SP, Fraissard J, Pavlovskaya GE, Meersmann T. Molecular hydrogen and catalytic combustion in the production of hyperpolarized Kr-83 and Xe-129 MRI contrast agents. Proceedings of the National Academy of Sciences of the United States of America 2016;113(12):3164-3168.7. Zamberlan F, Lesbats C, Rogers NJ, Krupa JL, Pavlovskaya GE, Thomas NR, et al. Molecular Sensing with Hyperpolarized Xe-129 Using Switchable Chemical Exchange Relaxation Transfer. ChemPhysChem. 2015;16(11):2294-8.

8. Patz S, Muradyan I, Hrovat MI, Dabaghyan M, Washko GR, Hatabu H, et al. Diffusion of hyperpolarized (129)Xe in the lung: a simplified model of (129)Xe septal uptake and experimental results. New Journal of Physics. 2011;13:015009.

9. Chang YV. MOXE: A model of gas exchange for hyperpolarized 129Xe magnetic resonance of the lung. Magn Reson Med. 2013;69(3):884-90.
10. Mansson S, Wolber J, Driehuys B, Wollmer P, Golman K. Characterization of diffusing capacity and perfusion of the rat lung in a lipopolysaccaride disease model using hyperpolarized Xe-129. Magn Reson Med. 2003;50(6):1170-9.
11. Ruppert K, Brookeman JR, Hagspiel KD, Mugler JP. Probing lung physiology with xenon polarization transfer contrast (XTC). Magn Reson Med. 2000;44(3):349-57.

APPENDICES

Appendix 1: Birdcage coil construction for ^{129}Xe excitation and detection in the University of Nottingham preclinical MRI facilities

This section details a custom-built ^{129}Xe coil for the *in vivo* preclinical MRI Bruker scanner, located in the psychology department of the university of Nottingham.

Radiofrequency (RF) coils are used for the detection of the NMR signal. MRI imposes additional field homogeneity requirements on the RF coil. To date, the most commonly used in MRI and the most volume homogeneous RF resonators have the cylindrical geometry and are commonly termed "birdcage coils". Unlike a solenoid coil, the B_1 magnetic field in birdcage coils is generated perpendicular to the main axis of the cylinder of the coil. This allows for the alignment of the opening of the coil with the magnet bore thus giving a great opportunity to study live animals in relatively small bores (gradients bore diameter: 12 cm). In addition, the open bore design allows for a better delivery of life support and breathing for the animals during the experiments *in vivo*.

The birdcage coil for ^{129}Xe resonance frequency (83.8 MHz) was designed using the shareware program "BirdcageBuilder", distributed by the College of Medicine of Pennsylvania State University, USA (1).

The low-pass concept of the present birdcage coil was borrowed from a commercial Bruker coil used for measurements in small animals *in vivo* in scanner with the same bore size.

The critical geometric parameters were the diameter of the coil, the number and length of the rungs and the diameter of the RF shield surrounding the coil. The RF shield surrounding the coil is a very important component in the coil design as it alters the resonance frequency of the coil by inductive coupling and also ensures that no detuning of the tuning and matching capacitors occurs outside the magnet. Therefore, the ratio of the coil diameter to the RF shield diameter was approximately 0.66 to minimise the inductive coupling between the shield and the coil.

The following additional geometric parameters were used in the calculations of the rung capacitance to ensure that the coil resonates at 83.023 MHz: coil diameter = 74 mm; length of rungs = 148 mm and shield diameter = 112 mm.
In principle, at least 50 % of the coil surface has to be covered by the conductor. The following calculations were used to evaluate the width of an individual rung. The circumference of the coil is $\pi \times 74\, mm = 233\, mm$, therefore at least 117 mm have to be covered by the conductor. This results in approximately 7.3 mm for an individual rung and 16 rungs in total.

A1.1. Rung capacitor value determination

To determine the value of the rung capacitors of the low pass birdcage coil, the parameters displayed in Table A.1 were used in the simulation using the "BirdcageBuilder" software. The simulation returned a rung capacitor value of 13.9 pF.

Resonance frequency	*83.8 MHz*
Type of ER	Rectangular
Nb of rungs	16
Coil radius (cm)	3.7
Leg Length (cm)	14.8
Leg Width (cm)	0.8
RF shield radius (cm)	5.6
ER segment length (cm)	1.45
ER segment width (cm)	0.8

Table A.1 Geometrical parameters for the construction of the ^{129}Xe birdcage coil resonating at 83.8 MHz at 7 T.

A1.2. Conductor thickness in the RF shield

In simplest terms, the main purpose of the RF shield is to avoid the detuning of the tuning and matching capacitors when the coil is placed inside the magnet bore for measurements. Therefore, the thickness of the shield conductor should exceed the required skin depth δ for an efficient isolation from unwanted irradiation. The skin depth can be determined using the well-known relationship (2):

$$\delta = \sqrt{\frac{2\rho}{2\pi\upsilon\mu}} \qquad \text{Eq. A.1}$$

where ν is the frequency in Hz, ρ is the resistivity of the conductor in $\Omega.\mathrm{m}$, and μ is the magnetic permeability of the conductor in $H.m^{-1}$.

Using the ^{129}Xe resonance frequency at 7 T $\upsilon = 83.8\,MHz$, the resistivity of copper $\rho = 1.678\times10^{-8}\Omega.m$ and the magnetic permeability of copper $\mu = 1.256\times10^{-6}H.m^{-1}$, we get a skin depth of $\delta = 7.13\times10^{-6}m$.

This means that the thickness of the copper conductor chosen for the shield manufacturing has to exceed 7 μm in order to provide efficient isolation from unwanted irradiation.

A1.3. ^{129}Xe birdcage coil outline and manufacturing

The outline of the coil is given in Figure A.1. The birdcage coil is composed of 16 equally spaced rungs connected by two end-rings as shown in the left panel of Figure A.1. To ensure the desired low-pass band, the rung capacitors were placed in the centre of each rung.

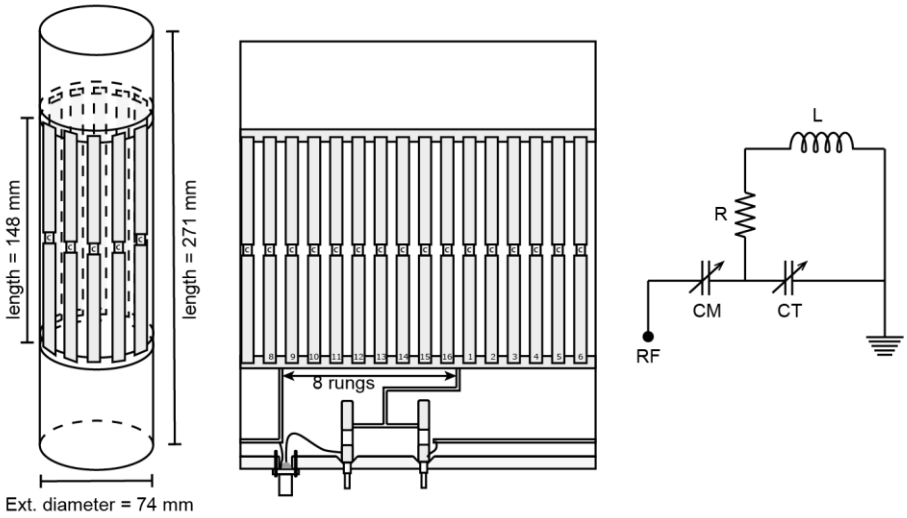

Figure A.1 Left panel - The outline of the coil with all relevant sizes. Central panel – mounting points of tuning and matching capacitors are shown. The capacitive matching circuit was used in this particular design to ensure that the coil resonates at the ^{129}Xe frequency at 7 T. Right panel – schematic of the capacitive matching circuit.

Copper tape (Saint Gobain, France) was used to manufacture rungs, end rings and other conducting components. 15 pF non-magnetic chip ceramic high power capacitors (ATC, New York, USA) have been used as rung capacitors.

A 2 mm thick acrylic cylinder with OD = 74 mm and length = 271 mm was used as a coil holder. The capacitive matching network shown in the right panel of Figure 2.2 was used to match the impedance to 50 Ohm and to tune the coil to the resonance frequency of 83.8 MHz. The circuit was attached to the coil as shown in the middle panel of Figure A.1. Glass trimmer capacitors (Voltronics Corporation, Maryland, USA) were used as variable tuning and matching capacitors.

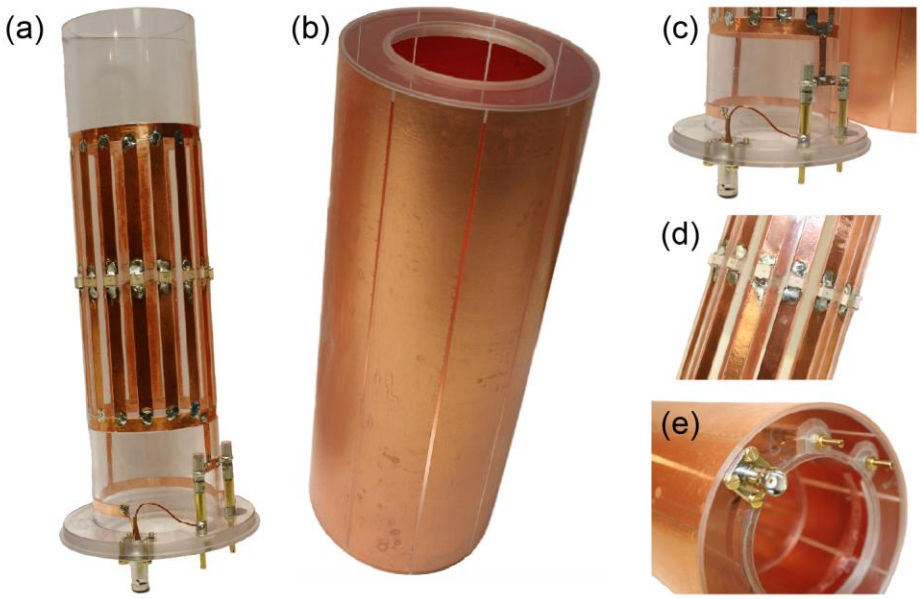

Figure A.2 Photographs of the components of a ^{129}Xe birdcage coil for a preclinical 7 T Bruker MRI scanner: (a) the birdcage coil, (b) the RF shield, (c) mounting points of the capacitive matching network, (d) the coil body with mounted 15pF rung capacitors, and (e) BNC plug and matching rods as positioned in the MRI scanner.

The RF shield composed of 9 copper foil strips of 40 mm in width and 270 mm in length was mounted onto 2 mm acrylic holder of OD = 112 mm and of length = 271 mm. The strips have been place evenly around the acrylic cylinder leaving gaps of equal size between the strips. The gaps were produced to quench eddy currents during the gradient pulsing of MRI experiments.

The coil and the shield were held together by two acrylic end-rings of OD = 108 mm. All components are displayed in Figure A.2.

A1.4. Testing, troubleshooting

The coil is loaded with a ^{129}Xe thermal sample and is matched to the 50 Ohm impedance. The RF homogeneity of the coil will also be determined to ensure the MR image quality. The coil stability and linear response will also be checked during RF pulsing. An example of thermal sample signal is given in Figure A.3.

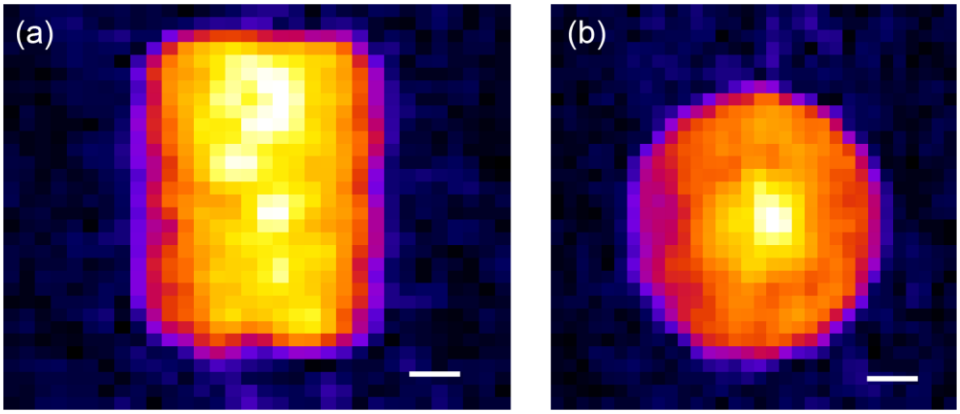

Figure A.3 Longitudinal (a) and axial (b) view of the ^{129}Xe thermal sample using the birdcage coil. Scale bar: 10 mm.

Appendix 2: Hp ^{129}Xe MRI of bleomycin-treated and control lungs using a Variable Flip Angle (VFA) FLASH pulse sequence

This section presents all of the images acquired for comparison of fibrotic lungs with control lungs (see Section 5.4.1.).

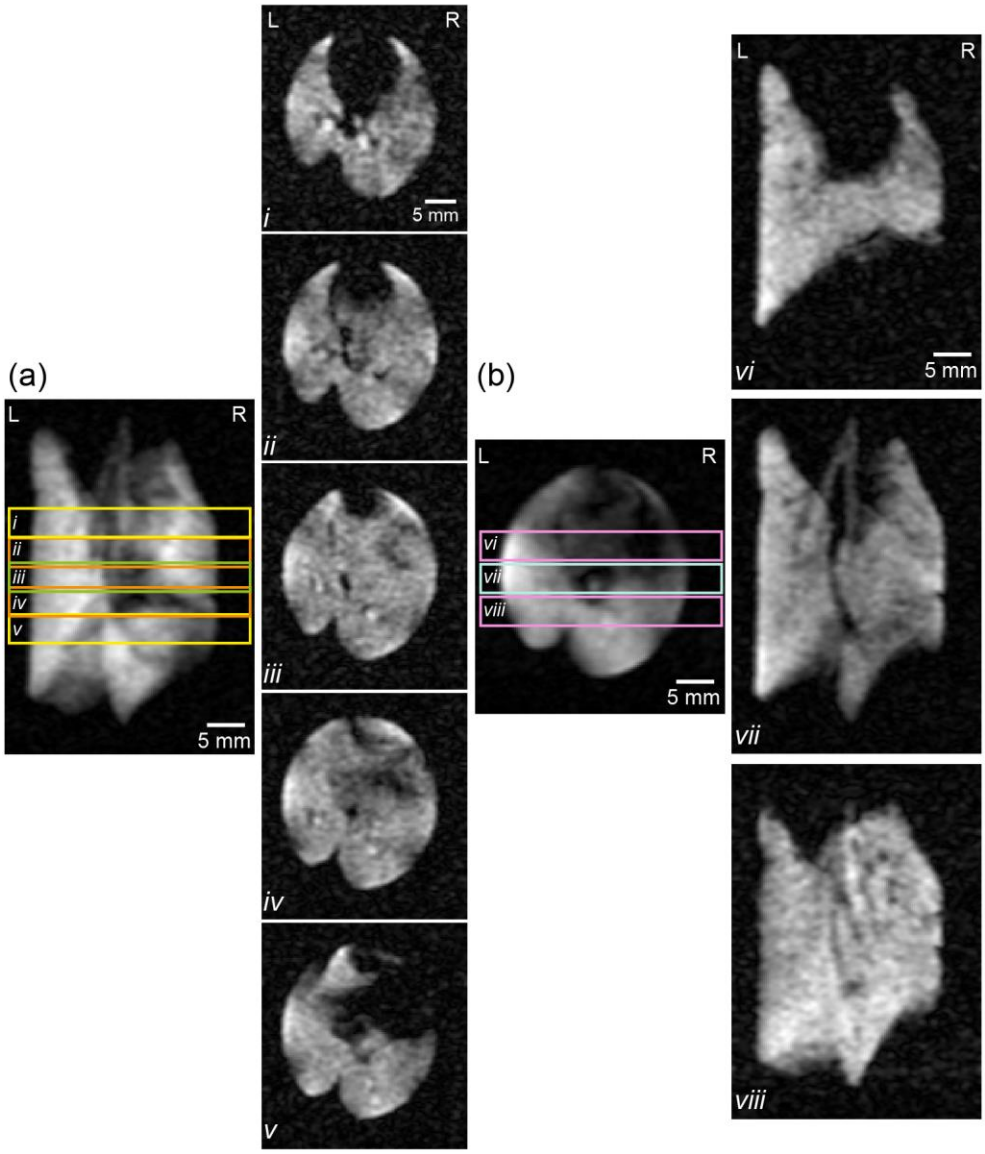

Figure A.4 Transverse (a) and coronal (b) slice selective VFA FLASH images of the excised Control lung 2_3 accompanied by a non-slice selective image showing the location of the slices.

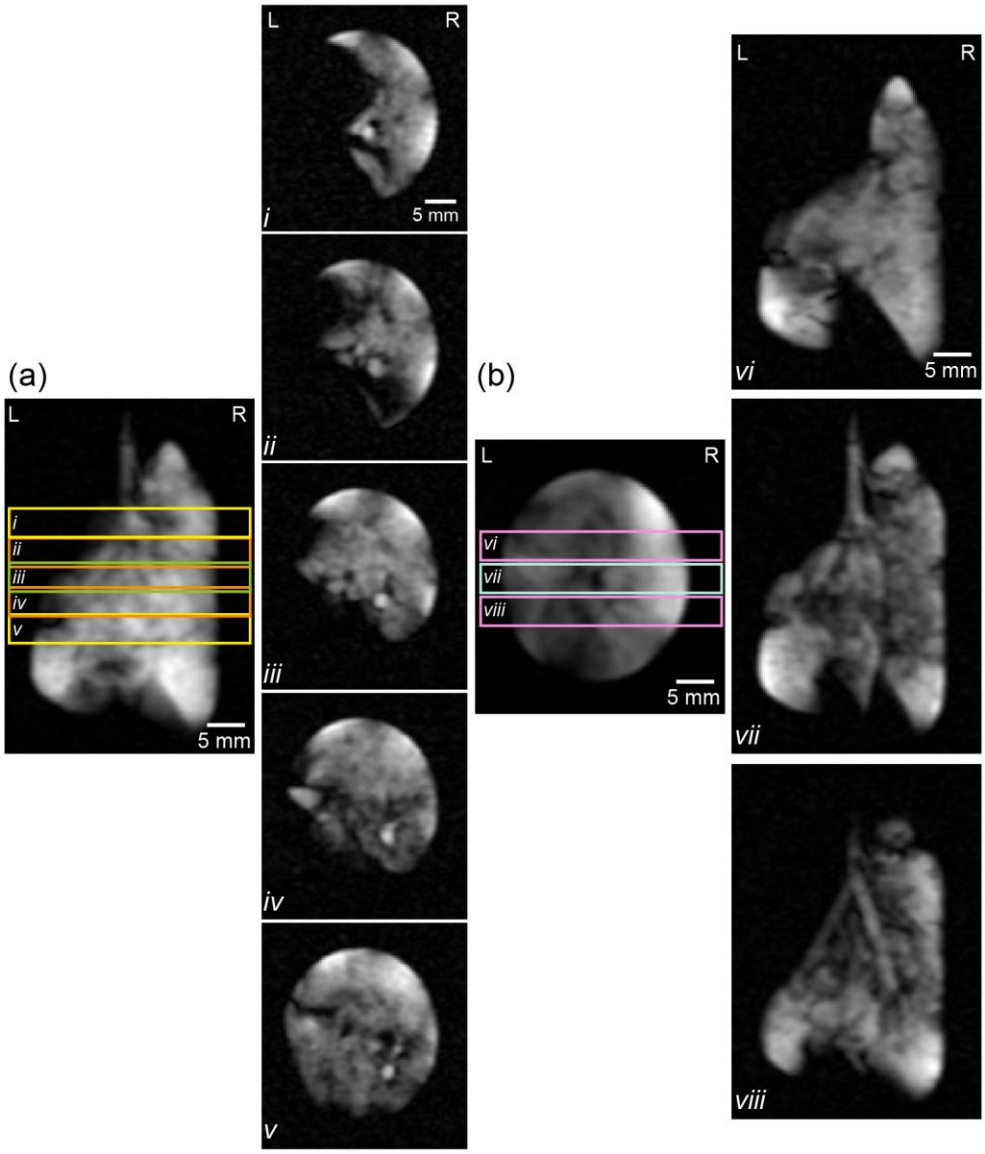

Figure A.5 Transverse (a) and coronal (b) slice selective VFA FLASH images of the excised Bleo lung 1_3 accompanied by a non-slice selective image showing the location of the slices. The left upper lobe is collapsed.

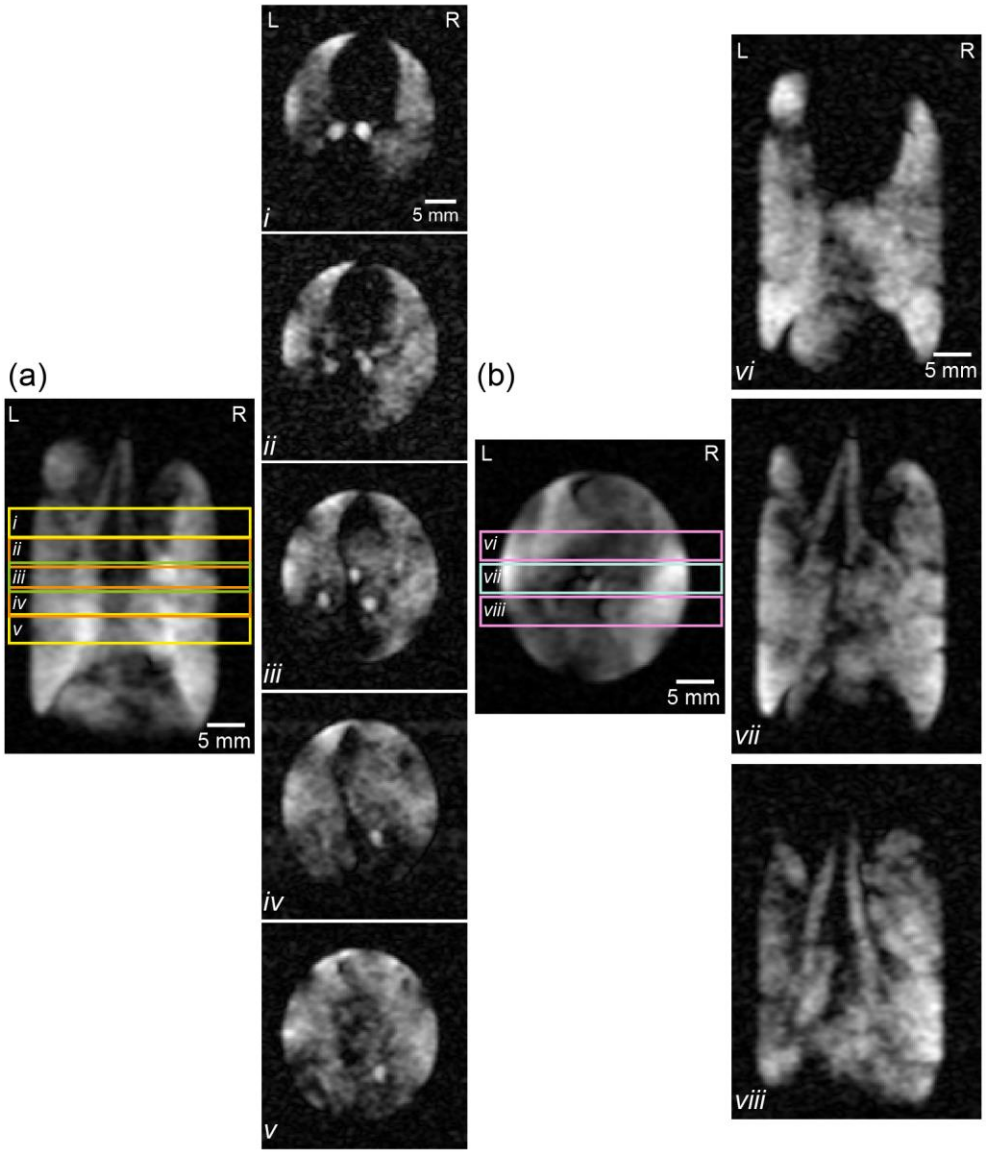

Figure A.6 Transverse (a) and coronal (b) slice selective VFA FLASH images of the excised Bleo lung 3_3 accompanied by a non-slice selective image showing the location of the slices.

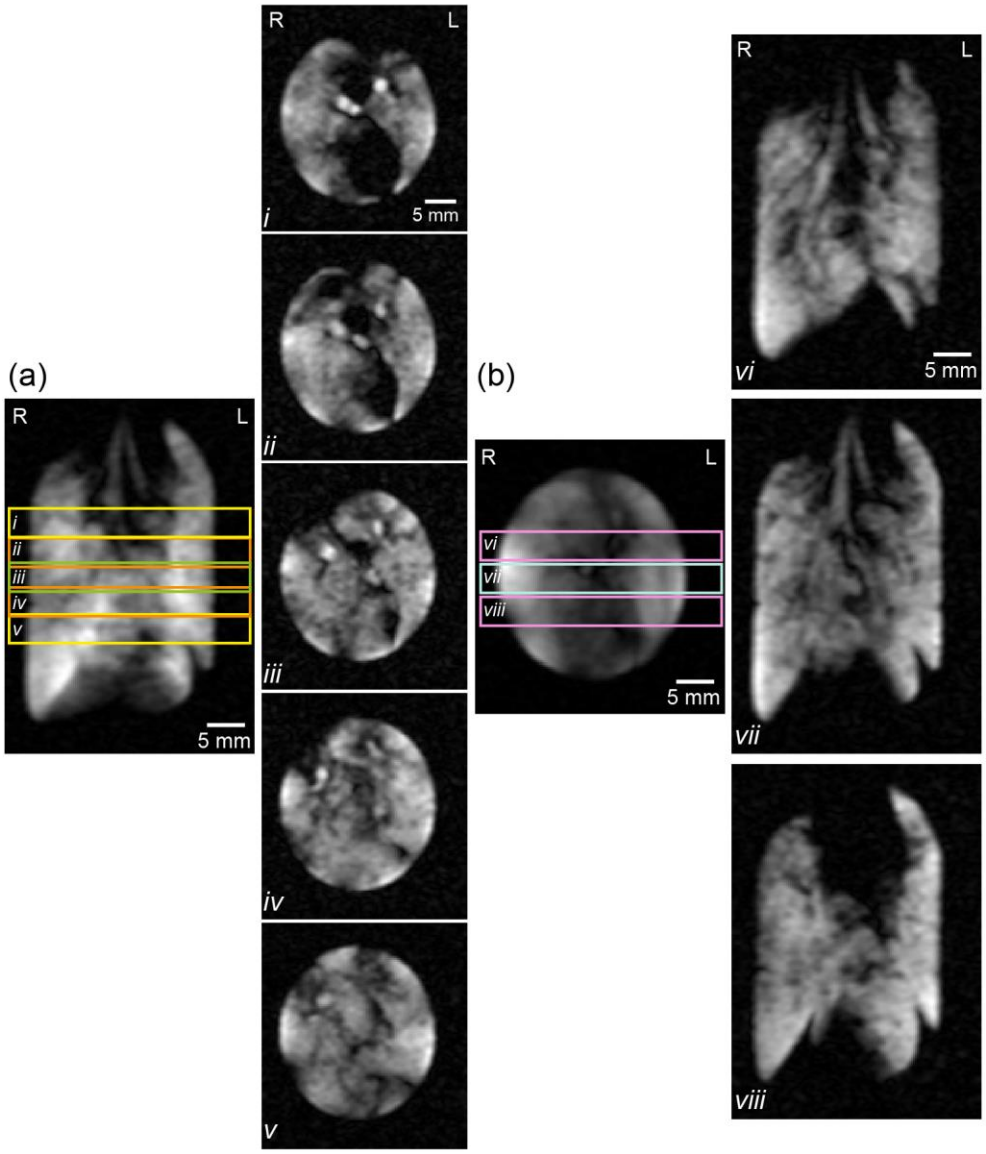

Figure A.7 Transverse (a) and coronal (b) slice selective VFA FLASH images of the excised Bleo lung 3_4 accompanied by a non-slice selective image showing the location of the slices.

References

1. Chin CL, Collins CM, Li SH, Dardzinski BJ, Smith MB. BirdcageBuilder: Design of specified-geometry birdcage coils with desired current pattern and resonant frequency. Concepts Magn Resonance. 2002;15(2):156-63.

2. Horowitz P, Hill W. The Art of Electronics: Cambridge University Press; 1980.